Atlas and Anatomy of PET/MRI

Vanessa Murad, E. Edmund Kim, Jin-Chul Paeng, Hyung-Jun Im, and Gi-Jeong Cheon

Hybrid positron emission tomography/magnetic resonance image (PET/MRI) has undergone rapid evolution during the last years, moving from a predominantly research field to clinical practice. With the advances in faster silicon photomultiplier detectors, MRI-based attenuation correction, and image reconstruction, significant improvements in equipment and image quality have been achieved. Currently, there are fully integrated PET/MRI systems that allow simultaneous and more rapid acquisition, improving not only the technical quality but also the experience for patients who need a low radiation dose [1–3]. With this technology comes the possibility of performing multiparametric MRI studies, where detailed anatomical evaluation and functional evaluation are possible, not only considering the qualitative and quantitative data of PET but also integrating multiple parameters such as perfusion (contrast-enhanced sequences), cellularity (diffusion-weighted sequence), metabolites (spectroscopic analysis), and texture analysis. Additionally, recent developments are very promising in giving the possibility of incorporating advanced data and biomarkers to integrate with bioinformatics and allow a better understanding of the disease, as well as an efficient evaluation, prediction of response to treatment, and follow-up [4–7].

With the growing availability of PET/MRI, its main and differential applications have also been clarified. Nonspecific ^{18}F-fludeoxyglucose (FDG) PET/MRI continues to be the most widely used, and thus new radiotracers are expanding the field to be explored. Among the most frequent applications of ^{18}F-FDG PET/MRI, where its superiority over PET/CT has been demonstrated, are the evaluation of head and neck, colorectal, gynecological, bone and soft tissue tumors, as well as the evaluation and characterization of primary or secondary liver lesions [8–12]. It has also shown good results in non-tumor pathology such as epilepsy, inflammatory bowel disease, and cardiac sarcoidosis [4, 13].

The creation of new radiotracers that can be imaged both with PET/MRI and PET/CT, depending on the case and availability, has allowed great advances in the evaluation of other oncological and non-oncological pathologies. In the case of neuroendocrine tumors and prostate cancer, targeting somatostatin receptors with ^{68}Ga-DOTATOC, targeting PSMA with ^{68}Ga-PSMA-11 among others available tracers, and the inclusion of ^{177}Lu agents have revolutionized the diagnosis and treatment of these pathologies respectively [14, 15]. In the field of neuroimaging, the wide availability of radiotracers has made it possible to improve the evaluation of multiple targets different from glucose metabolism (FDG), such as DNA synthesis (^{18}F-fluorothymidine), protein synthesis (^{11}C-methionine, ^{18}F-fluoroethyl-L-tyrosine [FET], ^{18}F-fluoro-L-3,4-dihydroxyphenylalanine [DOPA]), and hypoxia (^{18}F-fluoromisonidazole) [16, 17]. In the field of degenerative diseases, where much remains to be explored and research is very promising, examples of emerging invaluable applications are amyloid PET and Tau PET for Alzheimer's disease, as well as ^{18}FP-CIT PET for Parkinson's disease [18, 19].

In this chapter, we present multiple demonstrative examples of the different uses of PET/MR, with the most relevant anatomical references for each case.

V. Murad (✉)
Department of Nuclear Medicine, Seoul National University College of Medicine, Seoul, Republic of Korea

Department of Diagnostic Imaging, Fundacion Santa Fe de Bogotá University Hospital, Bogota, Colombia

E. E. Kim
Department of Radiological Sciences, University of California, Irvine, School of Medicine, Orange, CA, USA

Department of Nuclear Medicine and Department of Molecular Medicine, Graduate School of Convergence Science and Technology, Seoul National University College of Medicine, Seoul, Republic of Korea

J.-C. Paeng · G.-J. Cheon
Department of Nuclear Medicine, Seoul National University College of Medicine, Seoul, Republic of Korea

H.-J. Im
Departments of Applied Bioengineering, Molecular Medicine, and Biopharmaceutical Sciences, Graduate School of Convergence Science and Technology, Seoul National University, Seoul, Republic of Korea

E. E. Kim et al. (eds.), *Atlas and Anatomy of PET/MRI, PET/CT and SPECT/CT*, https://doi.org/10.1007/978-3-030-92349-5_1

1 Head and Neck

1.1 Case 1

A 75-year-old male patient, with worsening dizziness and weakness in both legs. Brain malignancy was suspected on brain CT, so ^{18}F- FDG PET/MR was performed. Images revealed marked increased activity in a well-defined enhancing mass involving the corpus callosum, crossing the midline and with subependymal extension. Primary central nervous system (CNS) lymphoma was suspected, and stereotaxic biopsy confirmed a diffuse large B-cell lymphoma (Fig. 1) [20].

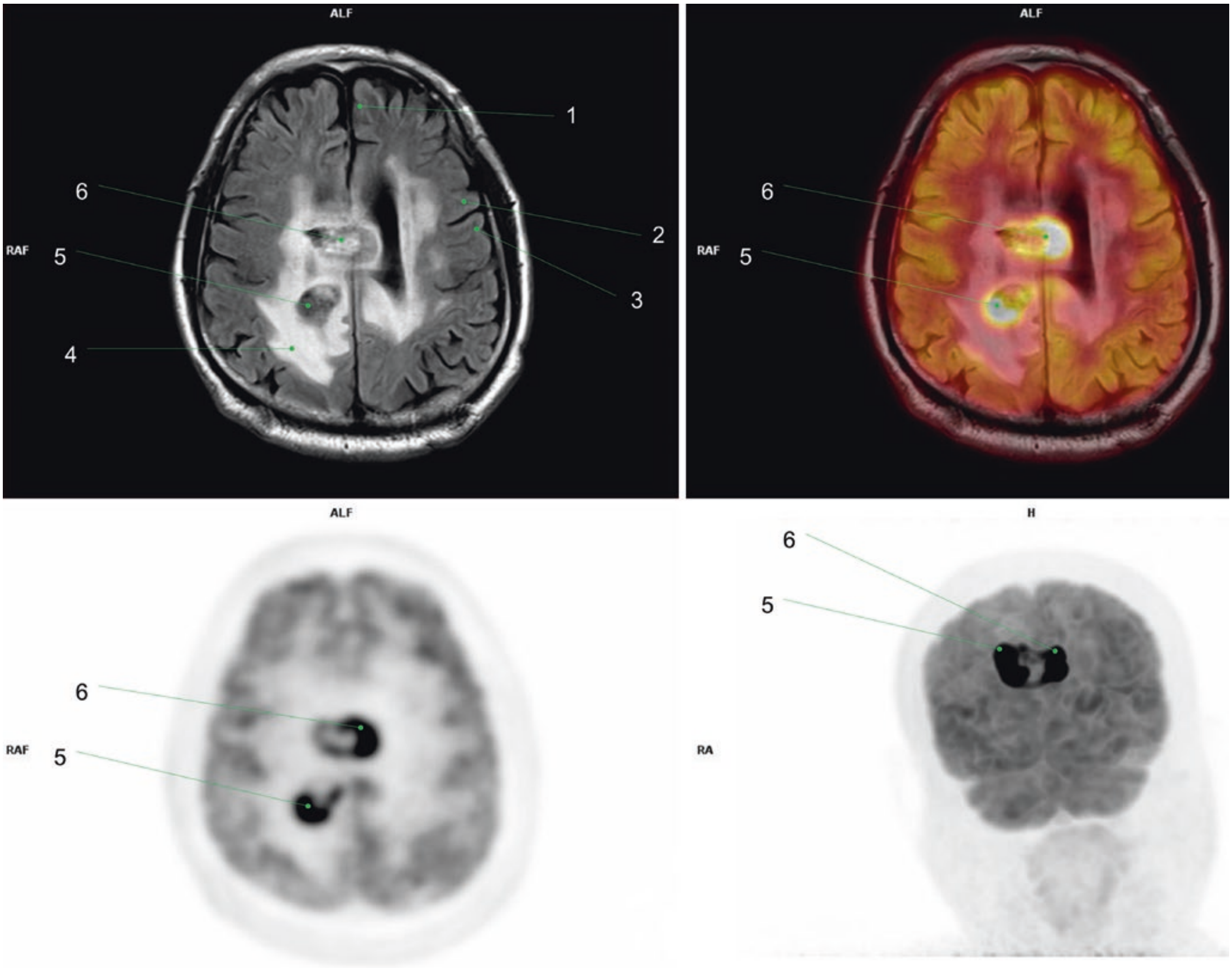

Fig. 1 1. Left superior frontal gyrus
2. Left precentral gyrus
3. Left postcentral gyrus
4. Peritumoral edema, right parietal lobe
5. Primary central nervous system lymphoma involving right parietal white matter
6. Primary central nervous system lymphoma involving corpus callosum

1.2 Case 2

A 72-year-old man with diagnosis of lymphoplasmacytic lymphoma (LPL)/Waldenström macroglobulinemia (WM) from marginal zone lymphoma, with central nervous system involvement. After surgery and chemotherapy, complete response was achieved, but the patient attended an early checkup with headache, so ^{18}F-FDG PET/MR was performed. Images showed focal increased activity in a lobulated mass at the periventricular white matter, adjacent to the posterior horn of the left lateral ventricle with perilesional edema, which showed predominantly low signal on T2WI and heterogeneous contrast enhancement, which are frequent findings of lymphoma involvement. With these findings, a relapse was confirmed, and treatment was initiated again (Fig. 2) [21].

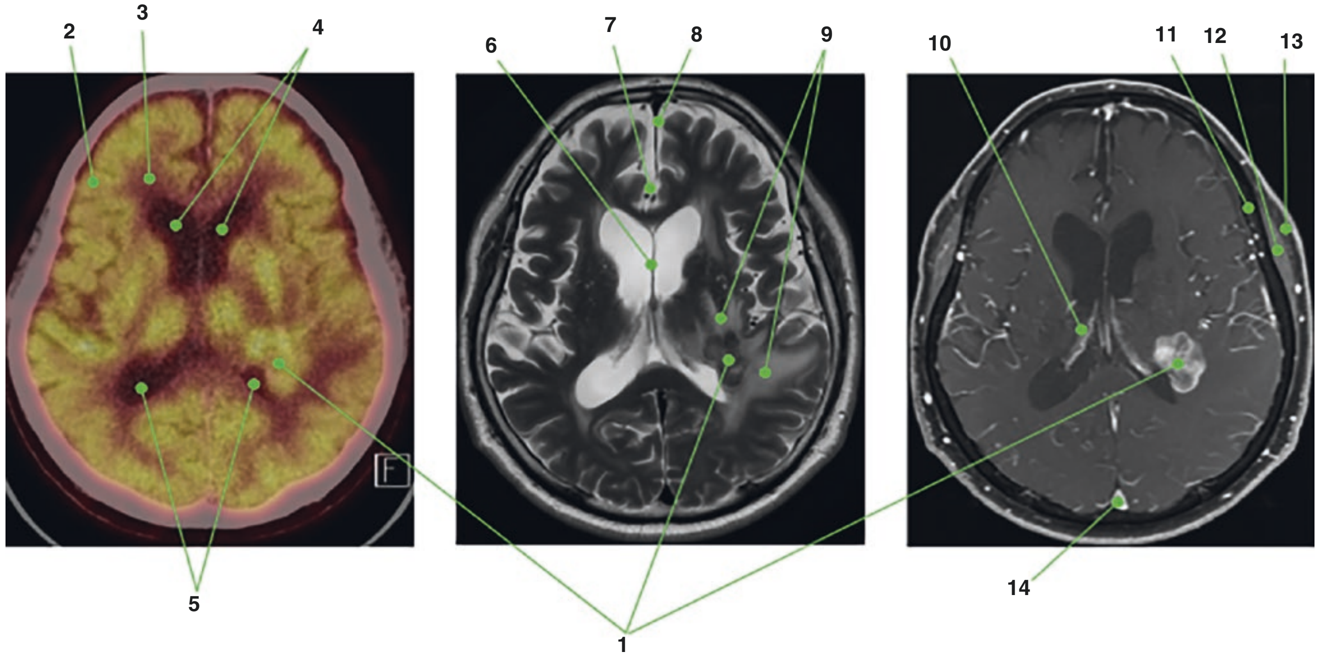

Fig. 2 1. Metabolically active lymphoma adjacent to the posterior horn of the left lateral ventricle
2. Normal FDG uptake in gray matter at the frontal cortex
3. Normal FDG uptake in the white matter at the frontal lobe
4. Anterior horns of the lateral ventricles
5. Posterior horns of the lateral ventricles
6. Septum pellucidum
7. Anterior cerebral arteries
8. Falx cerebri, frontal region
9. Perilesional edema
10. Choroid plexus at right lateral ventricle
11. Skull, left parietal area
12. Left temporal muscle
13. Scalp, left parietal area
14. Superior sagittal sinus

1.3 Case 3

A 5-year-old patient with gradual loss of vision in the right eye. Clinical examination and contrast-enhanced MRI were performed and confirmed the diagnosis of retinoblastoma. ^{18}F-FDG PET/MR was performed during initial workup and staging. Minimal uptake was found in the primary tumor and the presence of metabolically active metastases was ruled out (Fig. 3) [22].

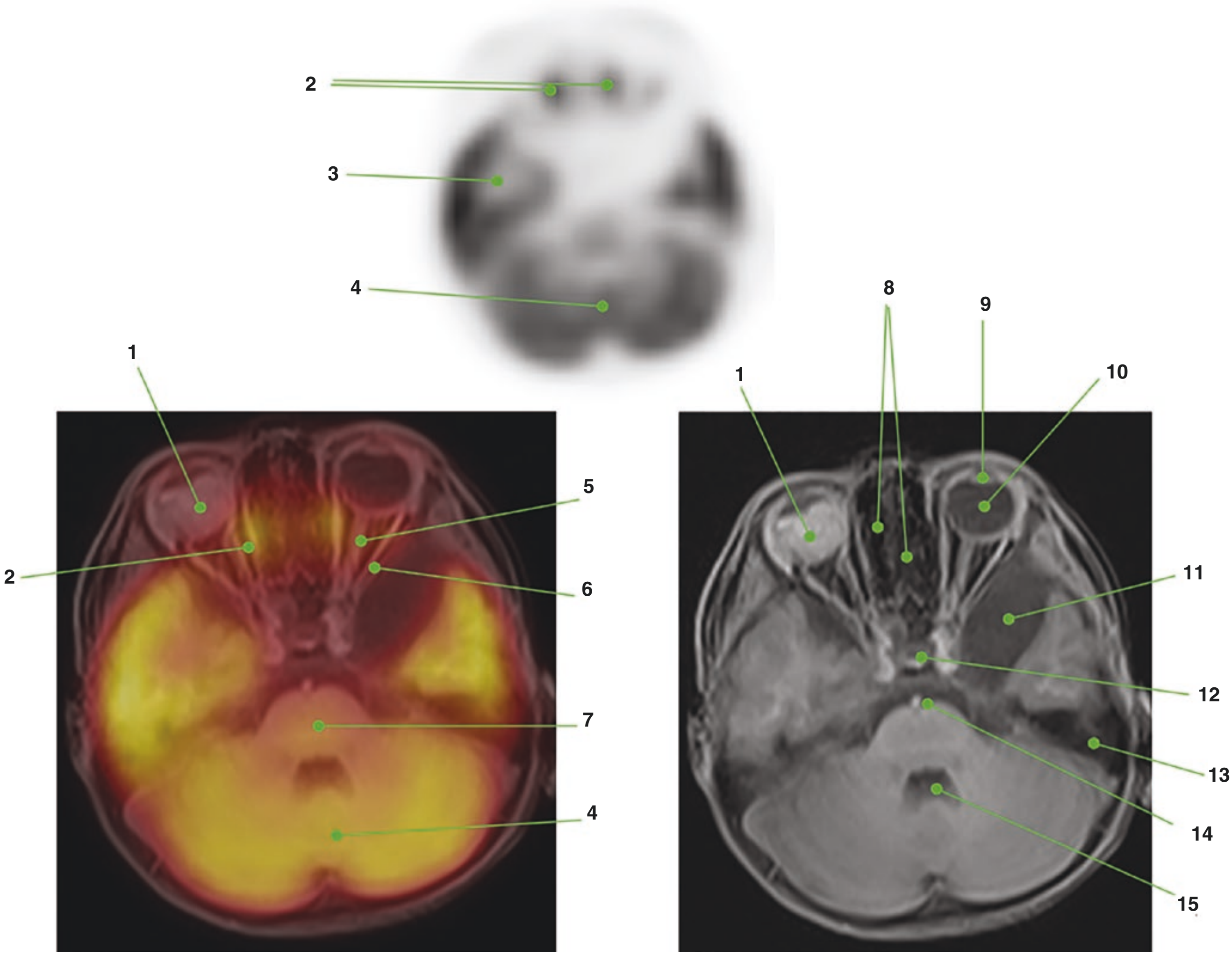

Fig. 3 1. Right eye retinoblastoma with minimal diffuse FDG uptake
2. Right medial rectus muscles
3. Right temporal lobe
4. Cerebellar vermis
5. Left optic nerve
6. Left lateral rectus muscle
7. Pons
8. Ethmoid air cells
9. Left eye, anterior chamber
10. Left eye, vitreous chamber
11. Left temporal arachnoid cyst
12. Pituitary gland
13. Left temporal bone
14. Basilar artery
15. Fourth ventricle

1.4 Case 4

A 49-year-old woman with a headache and decreased mobility of the right eye. ^{18}F-FDG PET/MR was performed, and images showed a metabolically active mass with heterogeneous enhancement in the olfactory recess involving the cribriform plate and ethmoid air cells. The lesion produced lateral displacement of the right medial rectus muscle, compression of the optic chiasm, and obstruction of the sphenoid sinuses. Subsequent biopsy confirmed the diagnosis of an olfactory neuroblastoma, also known as esthesioneuroblastoma (Fig. 4) [23].

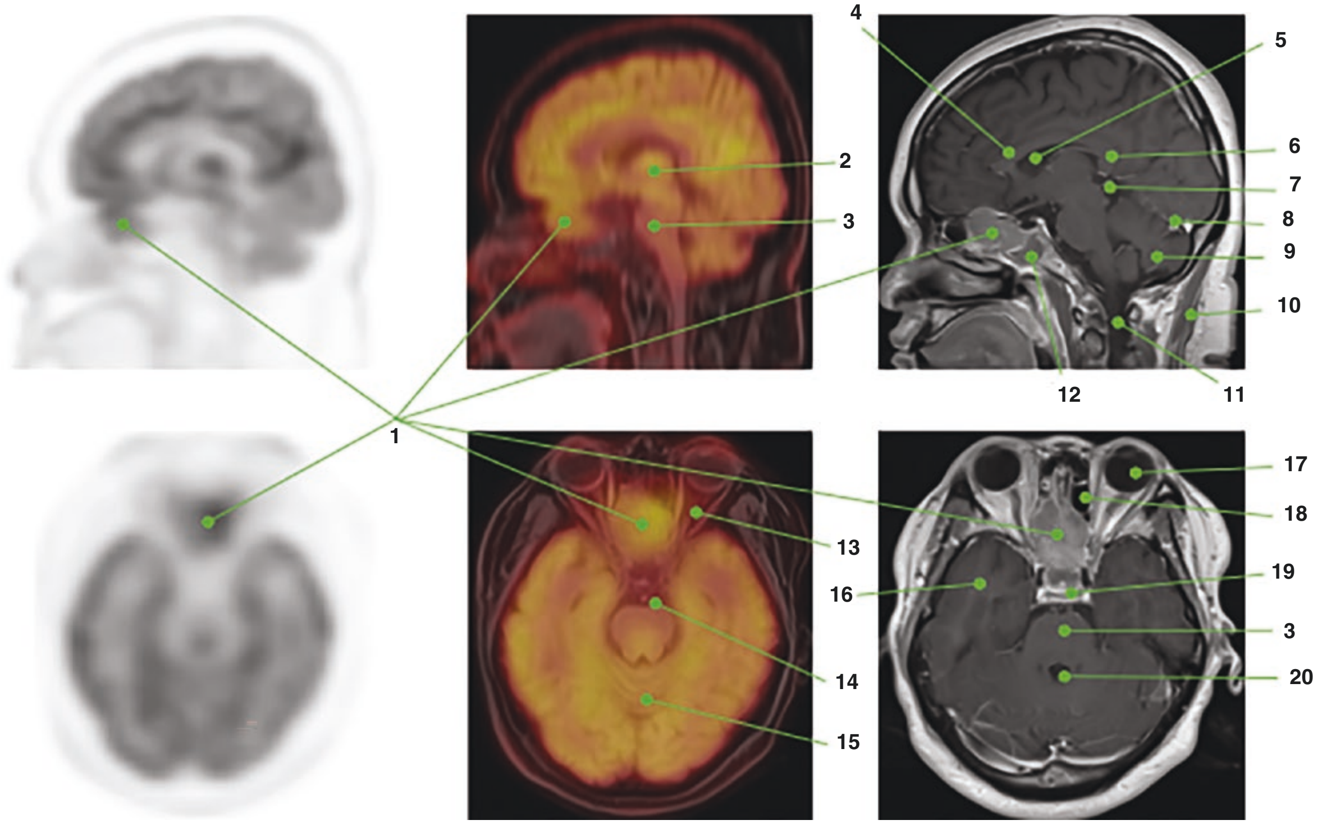

Fig. 4 1. Metabolically active tumor in the upper olfactory recess
2. Thalamus
3. Pons
4. Genu of corpus callosum
5. Lateral ventricle anterior horn
6. Splenium of corpus callosum
7. Pineal gland
8. Straight sinus
9. Cerebellum
10. Nuchal ligament
11. Spinal cord
12. Sphenoidal sinus with secretion due to obstruction
13. Left optic nerve
14. Basilar artery
15. Cerebellar vermis
16. Right temporal lobe
17. Left eye, vitreous chamber
18. Left ethmoid air cells
19. Optic chiasm
20. Fourth ventricle

1.5 Case 5

A 48-year-old male patient with progressive proptosis, impaired visual acuity, and headaches. ^{18}F-FDG PET/MR was performed, finding diffuse metabolically active infiltration of the soft tissues in both orbits and eyelids, with encasement and displacement of the optic nerves and muscles, without infiltration. Biopsy revealed the diagnosis of an extra nodal marginal zone B-cell lymphoma (EMZBC) (Fig. 5) [22].

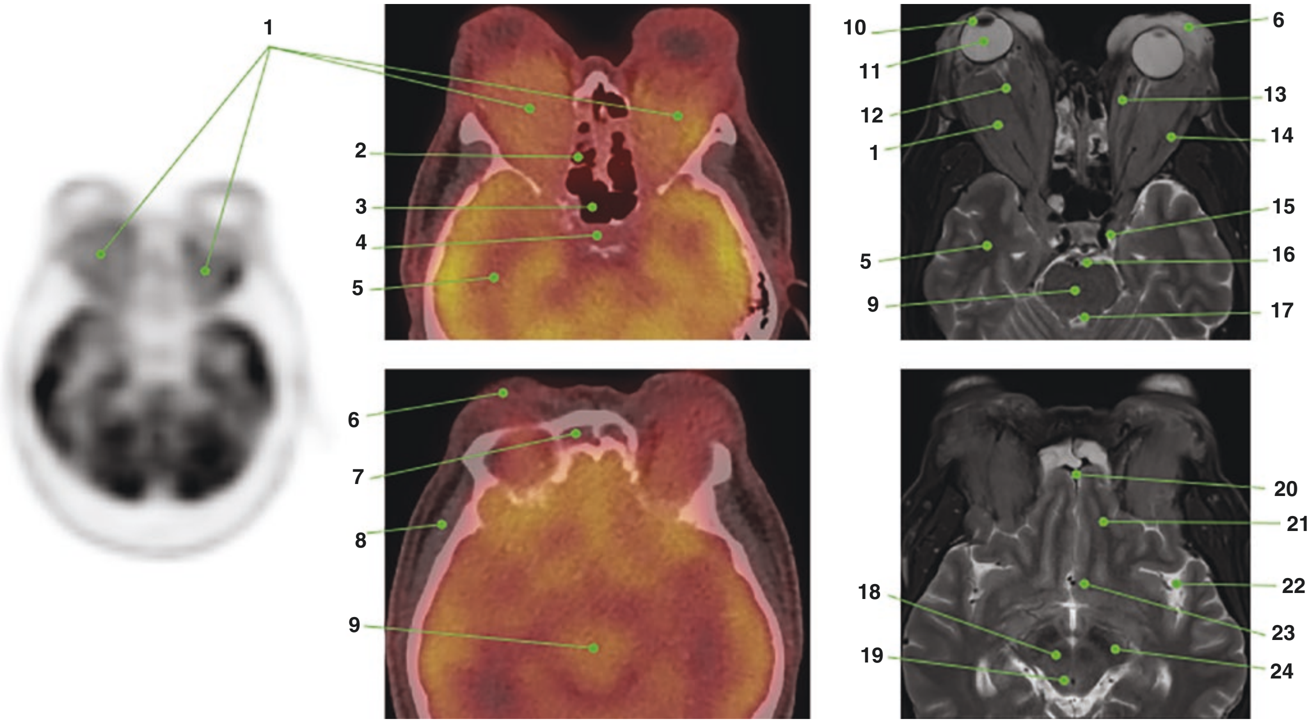

Fig. 5 1. Metabolically active bilateral orbital lymphoma infiltration
2. Right anterior ethmoid air cells
3. Right posterior ethmoid air cells
4. Sella turcica (pituitary gland)
5. Right temporal lobe
6. Right superior eyelid with lymphoma infiltration
7. Frontal sinuses
8. Right temporal muscle
9. Pons
10. Right eye lens
11. Right eye vitreous chamber
12. Right optic nerve
13. Left medial rectus muscle
14. Left lateral rectus muscle
15. Left internal carotid artery
16. Basilar artery
17. Fourth ventricle
18. Midbrain, red nucleus
19. Aqueduct of Sylvius
20. Crista galli
21. Left olfactory cortex
22. Left Sylvian fissure
23. Anterior cerebral arteries
24. Midbrain, sustancia nigra

1.6 Case 6

A 55-year-old male patient with sore throat and a soft tissue mass in the right nasopharyngeal wall on physical examination. Biopsy revealed nasopharyngeal squamous cell carcinoma, so ^{18}F-FDG PET/MR was performed for staging. Images showed increased metabolic activity in the right nasopharyngeal area at a soft tissue mass, consistent with the primary tumor. Hypermetabolic, enlarged, metastatic lymph node (LN) was also found in the right neck, level II (Figs. 6 and 7) [24].

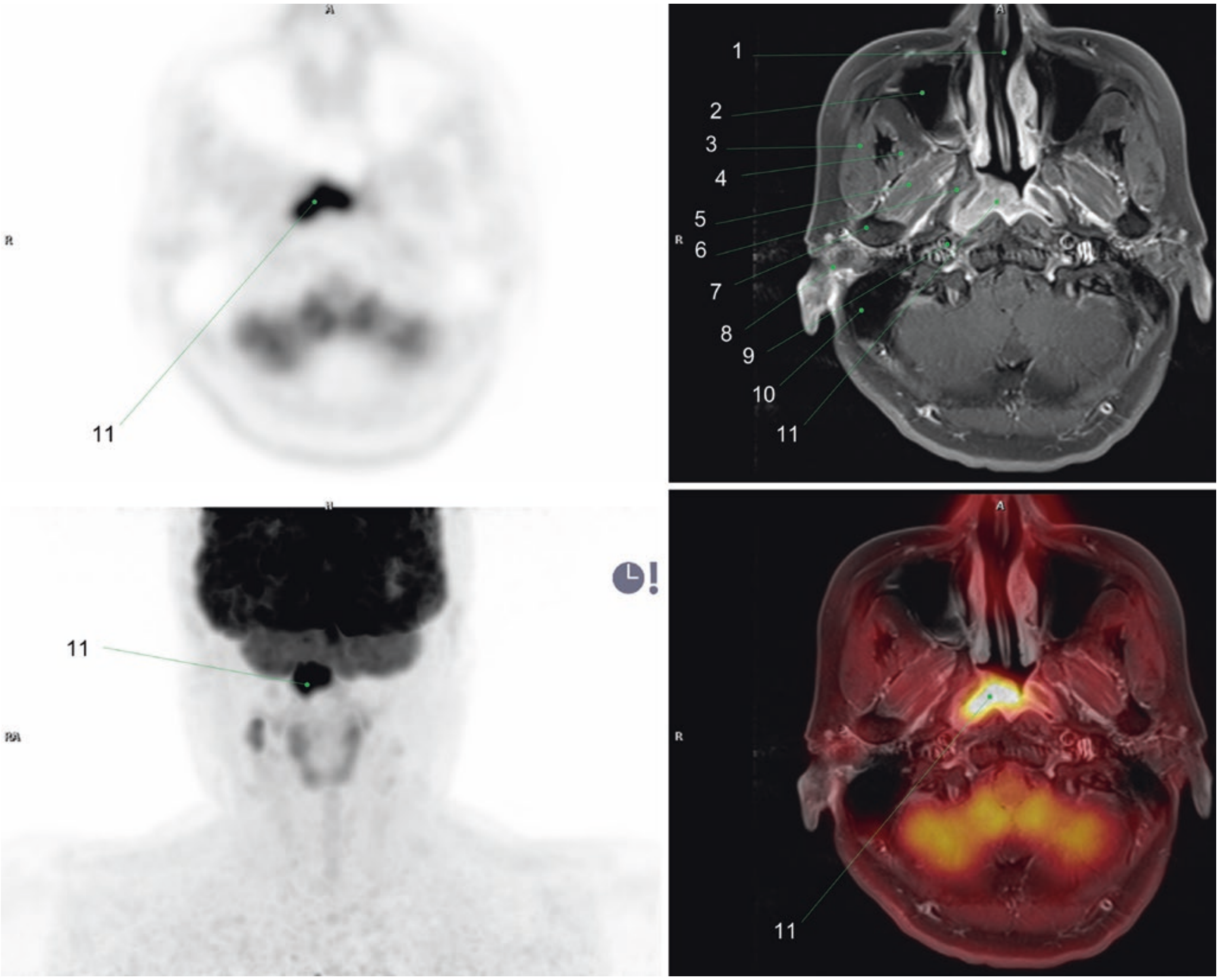

Fig. 6 1. Nasal septum
2. Right maxillary sinus
3. Right masseter muscle
4. Right temporalis muscle
5. Right lateral pterygoid muscle
6. Right medial pterygoid muscle
7. Right mandibular ramus
8. Right external auditory canal
9. Right internal carotid artery
10. Right mastoid air cells
11. Metabolically active tumor at the right fossa of Rosenmüller

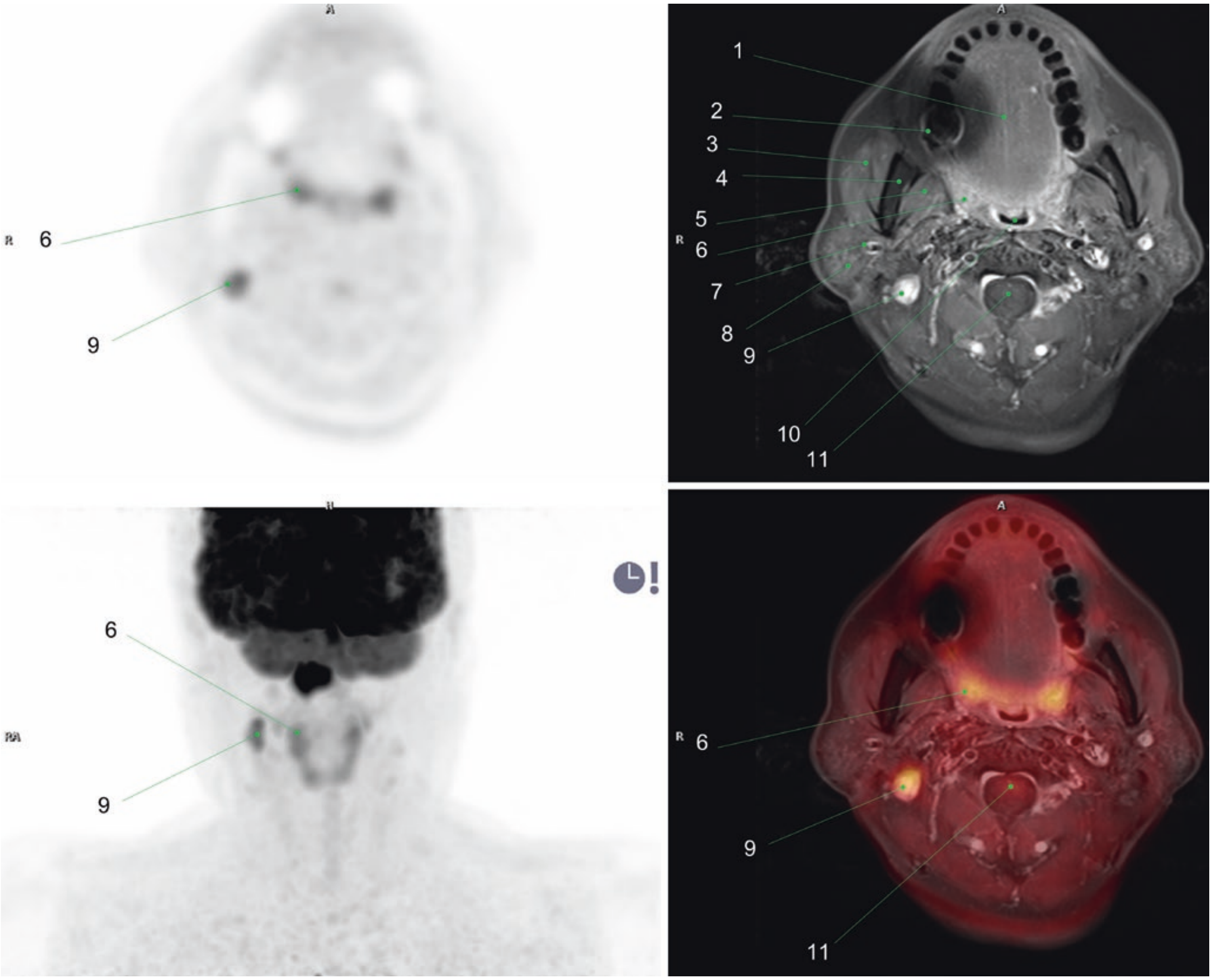

Fig. 7 1. Tongue
2. Right molar teeth with artifact due to dental implant
3. Right masseter muscle
4. Right mandibular ramus
5. Right medial pterygoid muscle
6. Right palatine tonsil
7. Right external maxillary vein
8. Right parotid gland
9. Metabolically active LN metastasis, right neck level II
10. Oropharynx
11. Spinal cord

1.7 Case 7

A 55-year-old female patient with a growing ulcerated mass in the right sublingual area. Biopsy was performed confirming an adenoid cystic carcinoma with cribriform pattern, so ^{18}F-FDG PET/MR was performed for staging. Images showed a focal hypermetabolic lesion in the right sublingual space, displacing the tongue's intrinsic muscles, without infiltrating them. Ipsilateral, level II, hypermetabolic lymph node metastasis was also found (Fig. 8) [10].

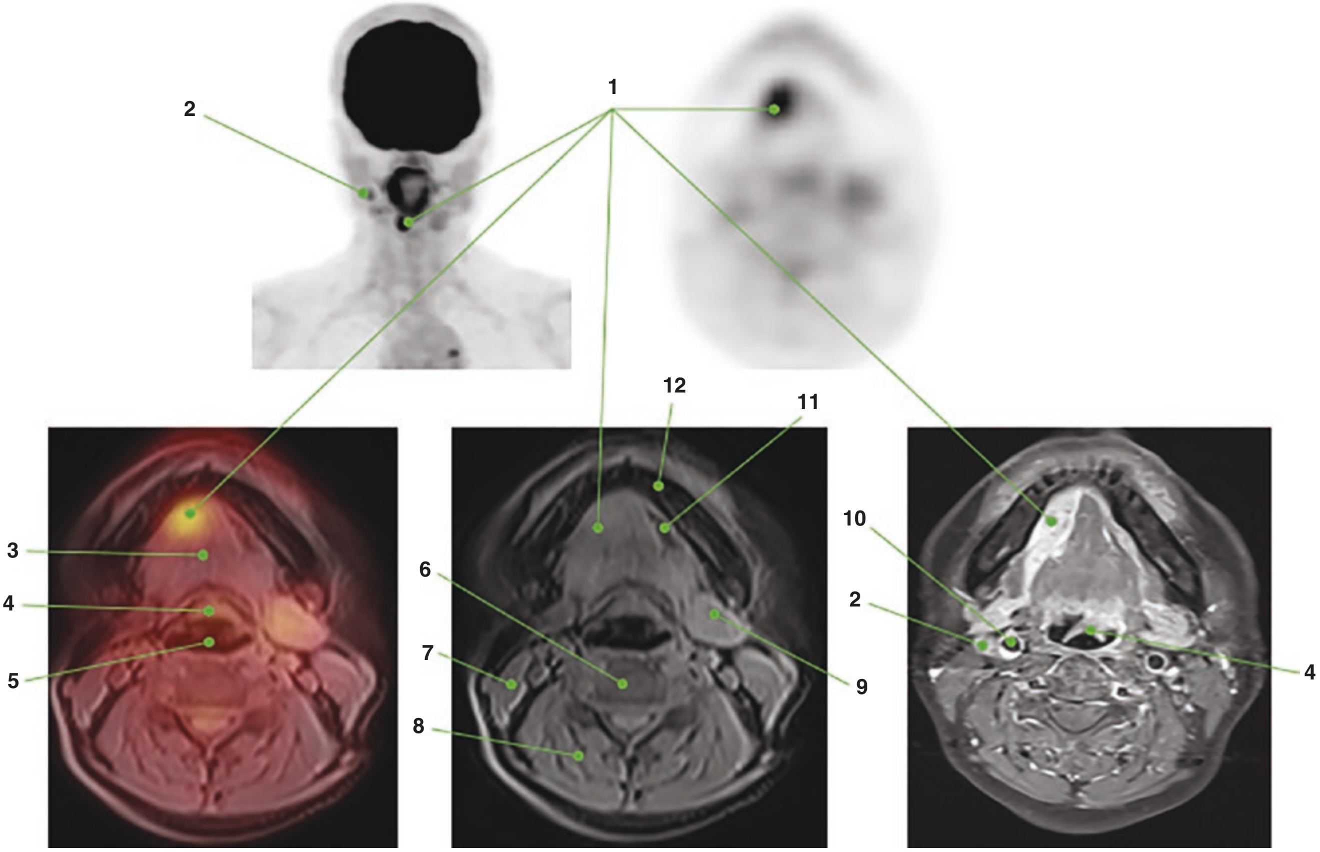

Fig. 8 1. Metabolically active tumor in the right sublingual space
2. Metastatic LN, right neck level II
3. Genioglossus muscle
4. Epiglottis
5. Larynx
6. Cervical vertebral body
7. Right sternocleidomastoid muscle
8. Posterior cervical muscles (inner to outer): semispinalis, splenius cervicis, and splenius capitis
9. Left submandibular gland
10. Right common carotid artery
11. Left sublingual space
12. Mandible, body

1.8 Case 8

A 55-year-old male patient with a history of persistent dysphagia and cough. Direct endoscopic examination was performed finding a laryngeal mass, consistent with an epiglottic squamous cell carcinoma. ^{18}F-FDG PET/MR was performed for staging, finding a prominent hypermetabolic mass in the superior aspect of the epiglottis, projecting towards the upper airway and decreasing its caliber. No hypermetabolic lymph nodes or distant metastases were observed (Fig. 9) [10].

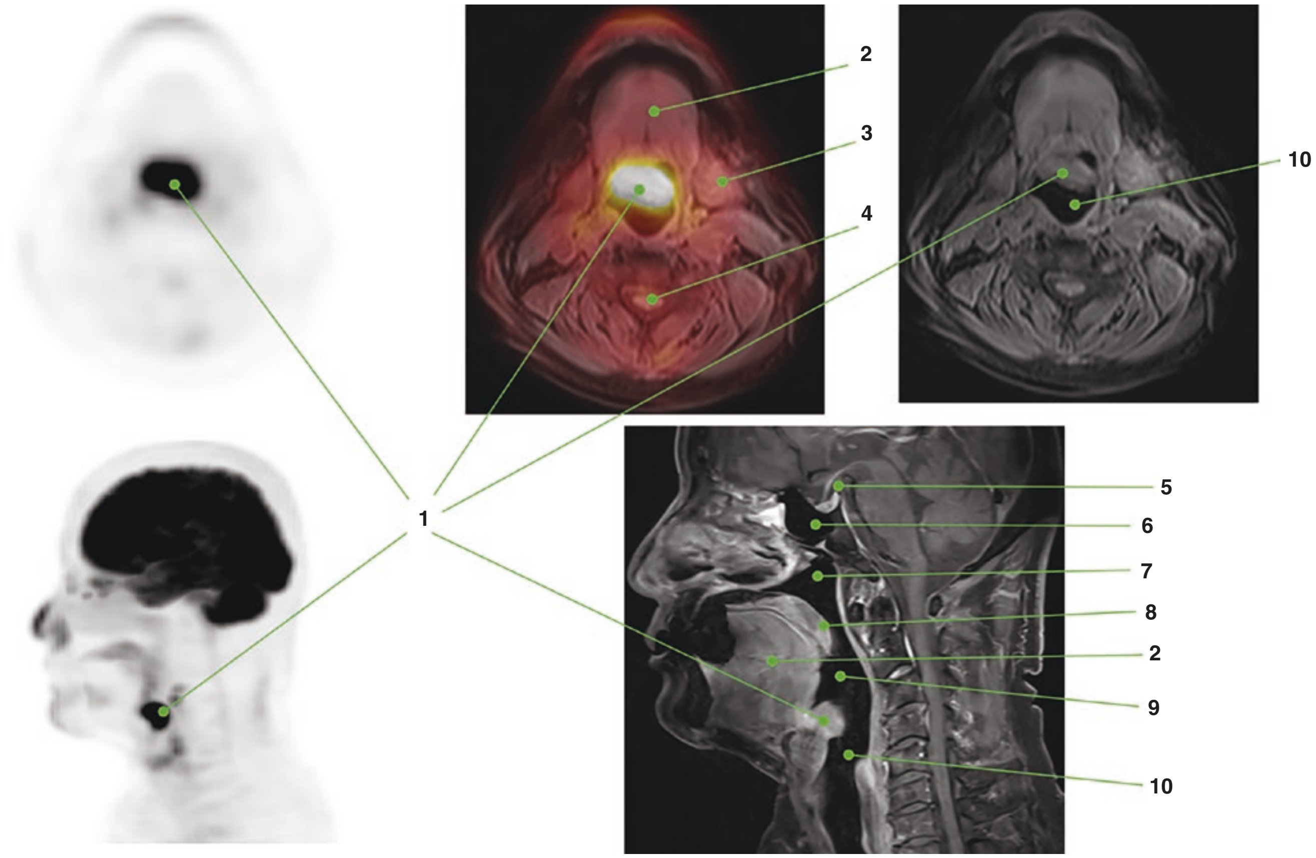

Fig. 9 1. Metabolically active epiglottic tumor
2. Intrinsic tongue muscles (genioglossus)
3. Left submandibular gland
4. Spinal cord
5. Pituitary gland and stalk
6. Sphenoid sinus
7. Nasopharynx
8. Uvula
9. Oropharynx
10. Larynx

1.9 Case 9

A 21-year-old man with a non-painful, progressively growing right parotid mass. Ultrasound-guided biopsy revealed a secretory carcinoma, so ^{18}F-FDG PET/MR was performed for staging. Images showed a hypermetabolic irregular mass involving both the superficial and deep lobes of the right parotid gland, without associated metastatic lymph nodes (Fig. 10) [25].

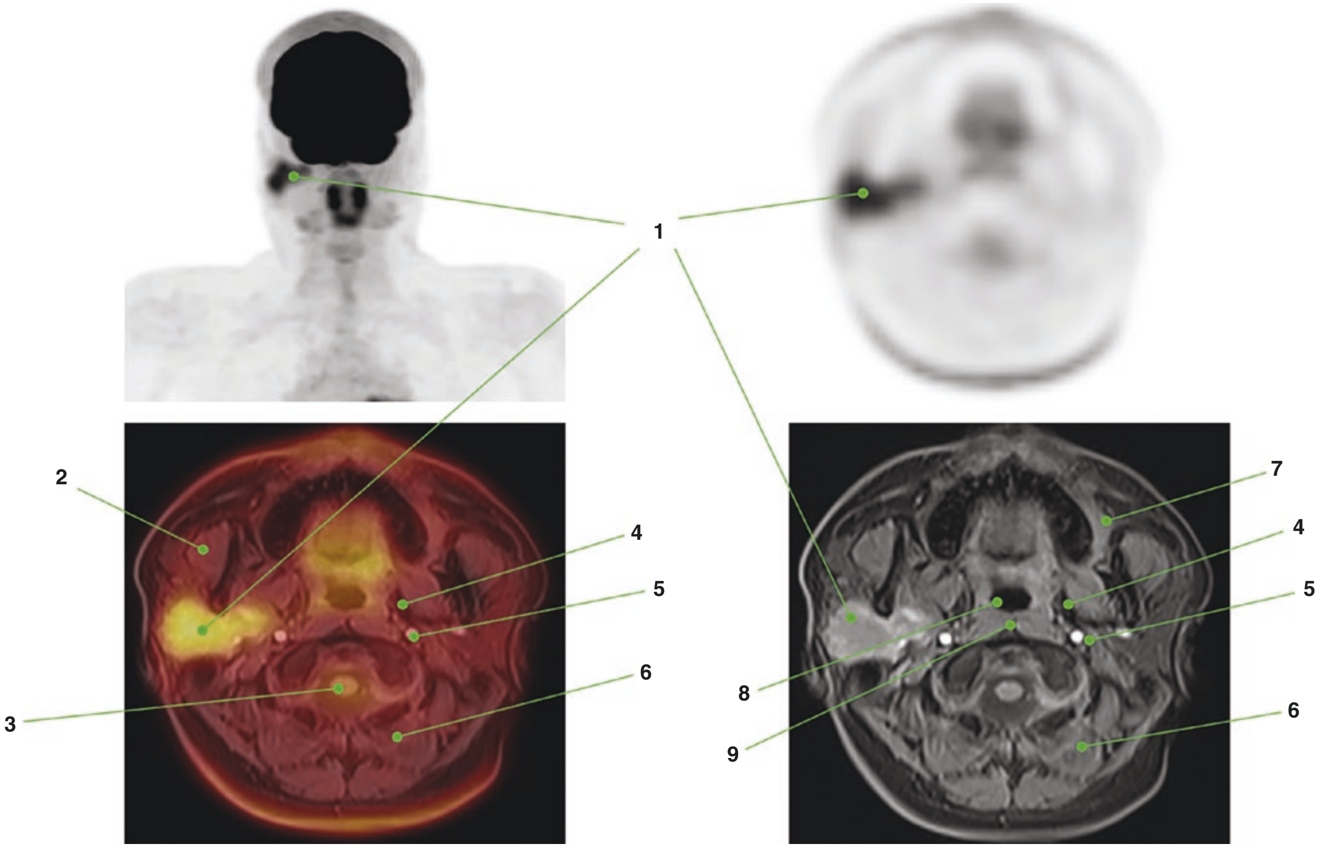

Fig. 10 1. Metabolically active right parotid tumor, involving both superficial and deep lobes
2. Right masticator space
3. Spinal cord
4. Left parapharyngeal space
5. Left carotid space
6. Left paraspinal space
7. Left buccal space
8. Oropharynx
9. Longus capitis muscles

1.10 Case 10

A 57-year-old man with a painful, rapidly growing left cervical mass. Ultrasound was performed finding an enlarged, necrotic lymph node, which biopsy revealed a metastatic carcinoma. ^{18}F-FDG PET/MR was performed suspecting primary head and neck malignancy, and images showed a hypermetabolic mass in the hypopharynx, predominantly left side, with multiple metastatic lymph nodes in the left neck. The diagnosis of primary squamous cell carcinoma in this location was confirmed (Fig. 11) [10].

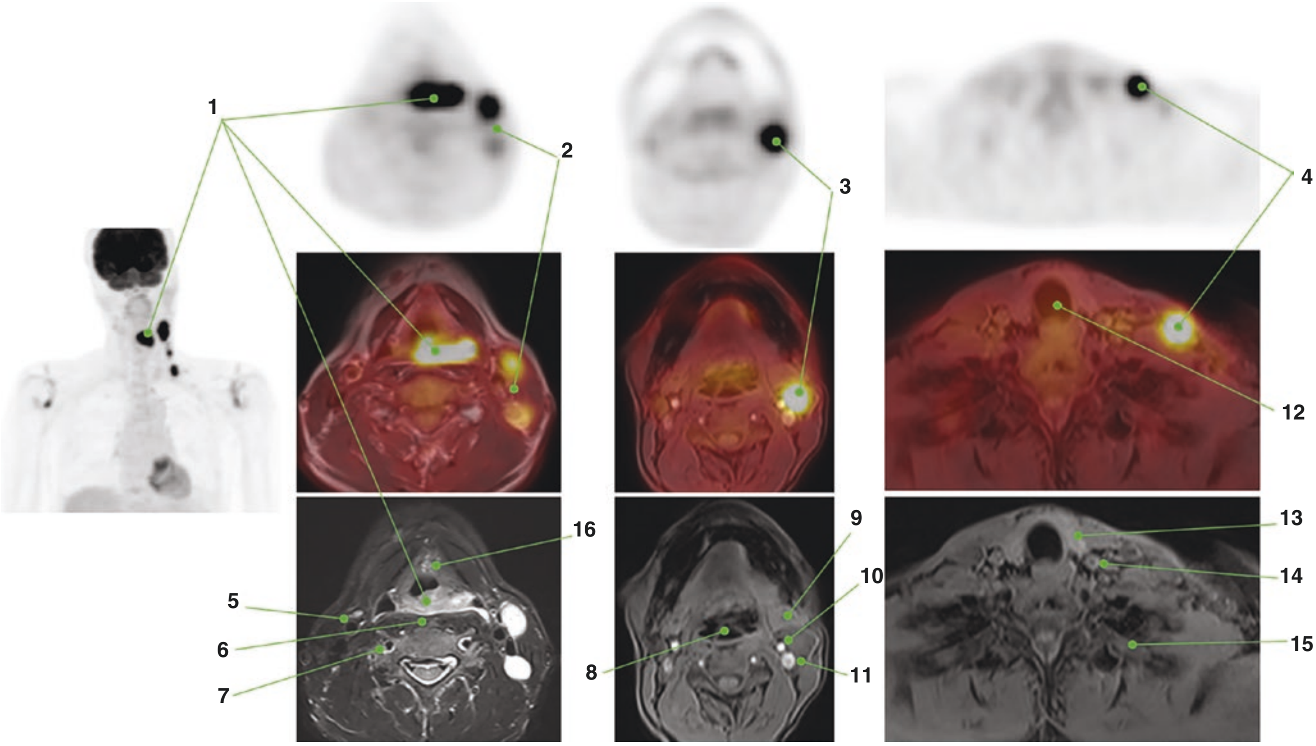

Fig. 11 1. Metabolically active hypopharyngeal tumor
2. Hypermetabolic metastatic neck lymph nodes: left, level III
3. Hypermetabolic metastatic neck lymph node: left, level II
4. Hypermetabolic metastatic neck lymph nodes: left, level IV
5. Right carotid artery
6. Retropharyngeal space
7. Right vertebral artery
8. Epiglottis
9. Left submandibular gland
10. Left carotid artery
11. Left jugular vein
12. Trachea
13. Left thyroid lobe
14. Left common carotid artery
15. Left second rib
16. Vocal cords

1.11 Case 11

A 22-year-old man with headache, occasional fever, and weakness in both arms. Laboratory tests did not show definite abnormalities, so ^{18}F-FDG PET/MR and MRI were performed to rule out unknown origin infection vs occult malignancy. Images showed diffusely increased activity along the spinal cord with corresponding ill-defined high signal intensity lesions in T2WI. With these findings and other neurological tests, the diagnosis of acute disseminated encephalomyelitis (ADEM) was confirmed (Fig. 12) [26].

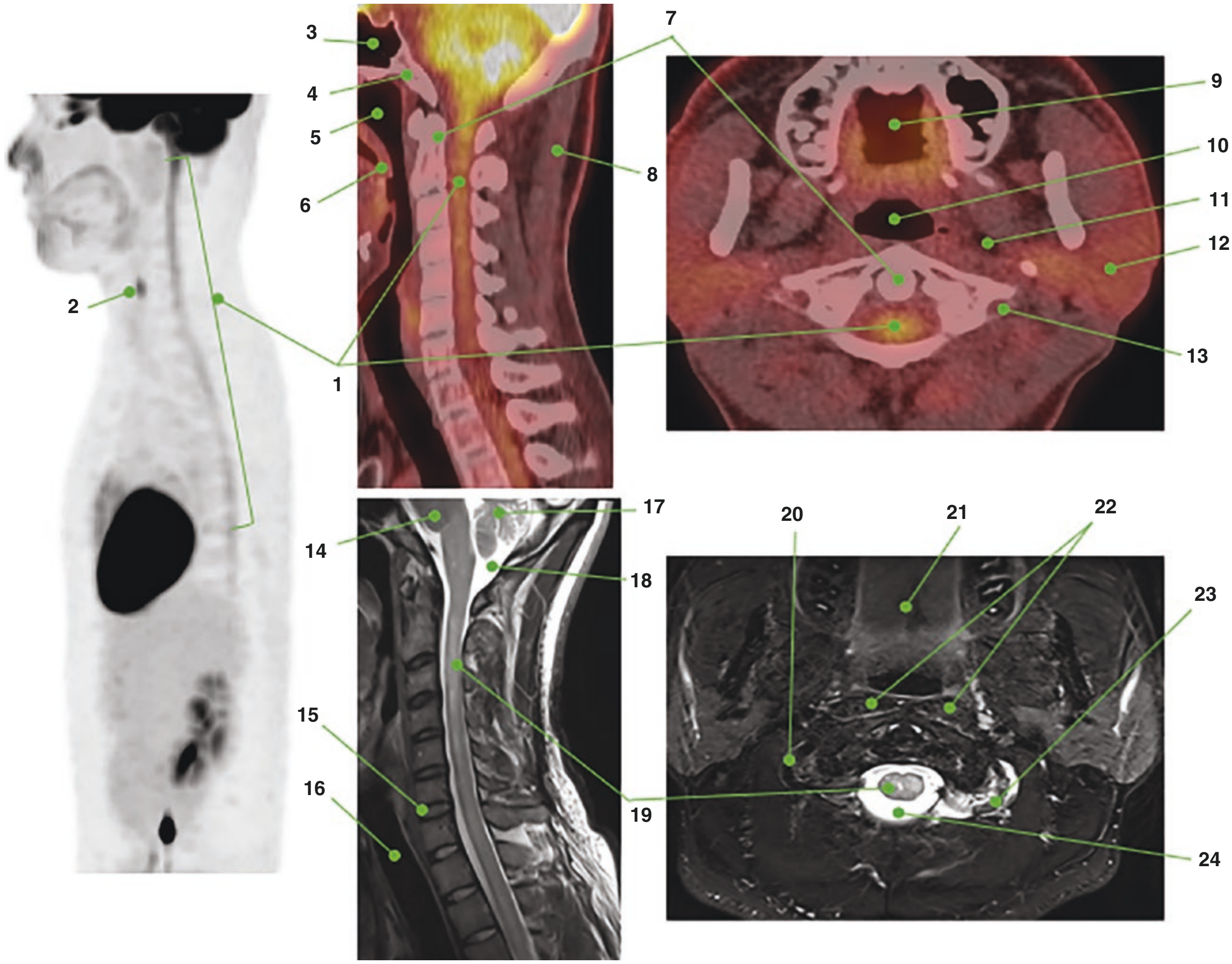

Fig. 12 1. Diffusely increased activity along the spinal cord
2. Focal increased activity at the vocal cords, physiologic
3. Sphenoid sinus
4. Clivus
5. Nasopharynx
6. Uvula
7. C2, odontoid process
8. Nuchal ligament
9. Oral cavity
10. Oropharynx
11. Left parapharyngeal space
12. Left parotid gland
13. Left vertebral foramen in C1
14. Brainstem
15. C6–C7 Intervertebral disc
16. Trachea
17. Cerebellum
18. Cisterna magna
19. Ill-defined high signal intensity lesions (T2WI)
20. Right vertebral artery
21. Hard palate
22. Longus capitis muscles
23. Left vertebral artery
24. Cerebrospinal fluid

1.12 Case 12

A 67-year-old male patient with a history of left maxillary sinus squamous cell carcinoma, treated 9 years ago with radiotherapy and surgery (resection with flap reconstruction). He attended his annual checkup completely asymptomatic and among other studies ^{18}F-FDG PET/MR was performed. Images showed focal increased activity in the lateral wall of the left nostril on the medial aspect of the surgical flap, which also presented heterogeneous contrast enhancement, which was not evident in the previous study. This finding was confirmed as a local recurrence (Fig. 13) [10].

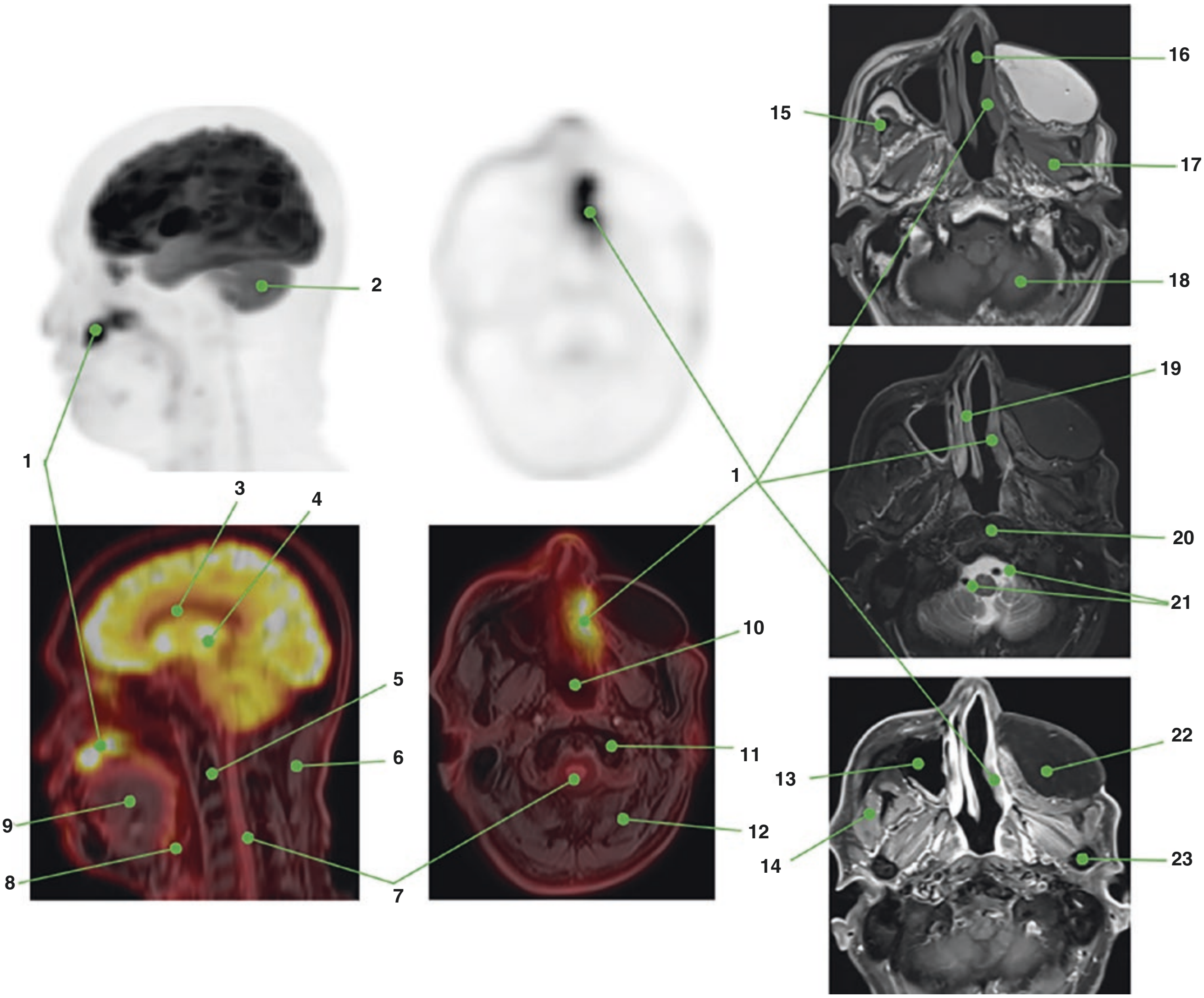

Fig. 13 1. Metabolically active recurred tumor in the surgical flap
2. Cerebellum
3. Lateral ventricles
4. Thalami
5. C2, odontoid process
6. Nuchal ligament
7. Medulla
8. Epiglottis
9. Tongue
10. Nasopharynx
11. Left occipital condyle
12. Left cervical paraspinal muscles (multifidus, longissimus capitis, splenius capitis)
13. Right maxillary sinus
14. Right masseter muscle
15. Right mandibular ramus
16. Left nostril
17. Left pterygoid muscles
18. Left cerebellar hemisphere
19. Nasal septum
20. Prevertebral muscles (longus capitis and rectus capitis muscles)
21. Proximal vertebral arteries
22. Surgical graft
23. Left mandibular condyle

2 Chest

2.1 Case 1

A 62-year-old male patient with a solitary pulmonary nodule and history of heavy smoking. ^{18}F-FDG PET/MR was performed during staging. Images showed moderately increased activity in a small solid nodule at the left lower lobe, which was later resected and confirmed as an adenocarcinoma. No metabolically active metastases were detected (Figs. 14, 15, 16, 17, 18, and 19) [27, 28].

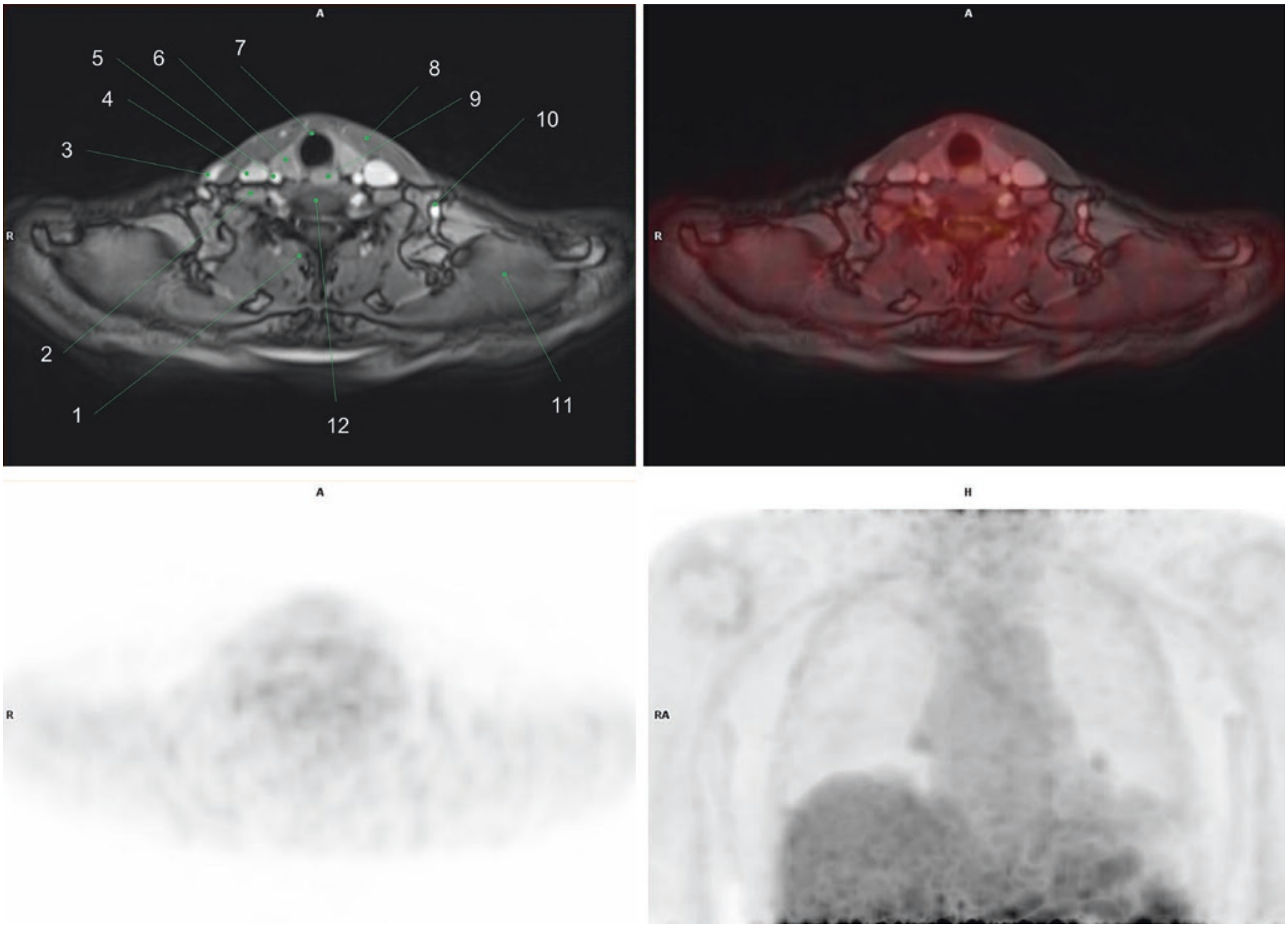

Fig. 14 1. Right erector spinae muscle
2. Right anterior scalene muscle
3. Right external jugular vein
4. Right internal jugular vein
5. Right common carotid artery
6. Thyroid gland, right lobe
7. Trachea
8. Left sternocleidomastoid muscle
9. Esophagus
10. Normal lymph node, left neck, level IV
11. Left trapezius muscle
12. Cervical vertebral body

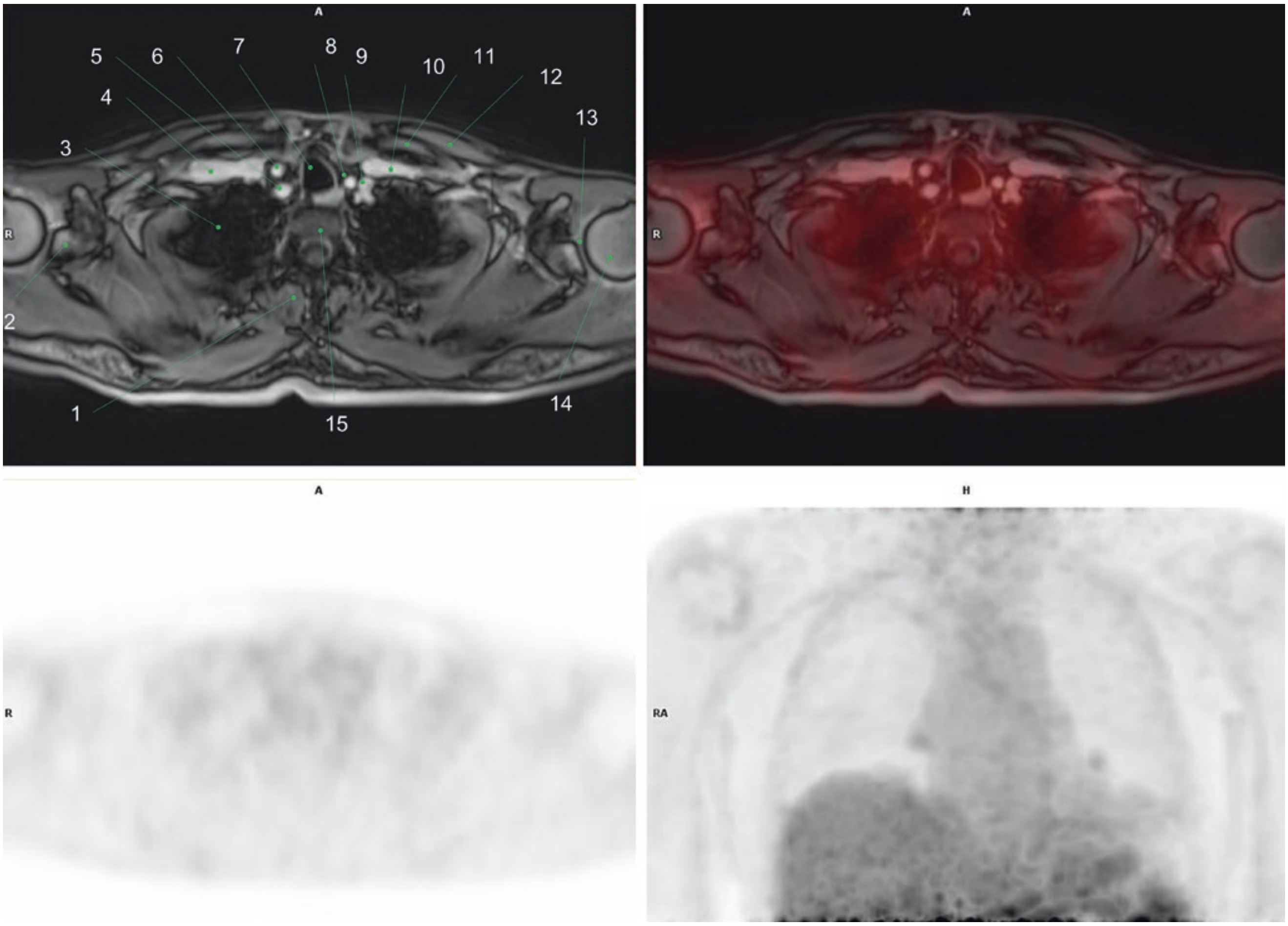

Fig. 15 1. Right erector spinae muscle
2. Right glenoid
3. Right lung apex, right upper lobe (RUL)
4. Right subclavian vein
5. Right subclavian artery
6. Right common carotid artery
7. Trachea
8. Left common carotid artery
9. Left subclavian artery
10. Left subclavian vein
11. Left pectoralis minor muscle
12. Left pectoralis major muscle
13. Left glenohumeral joint
14. Left humeral head
15. Thoracic vertebral body

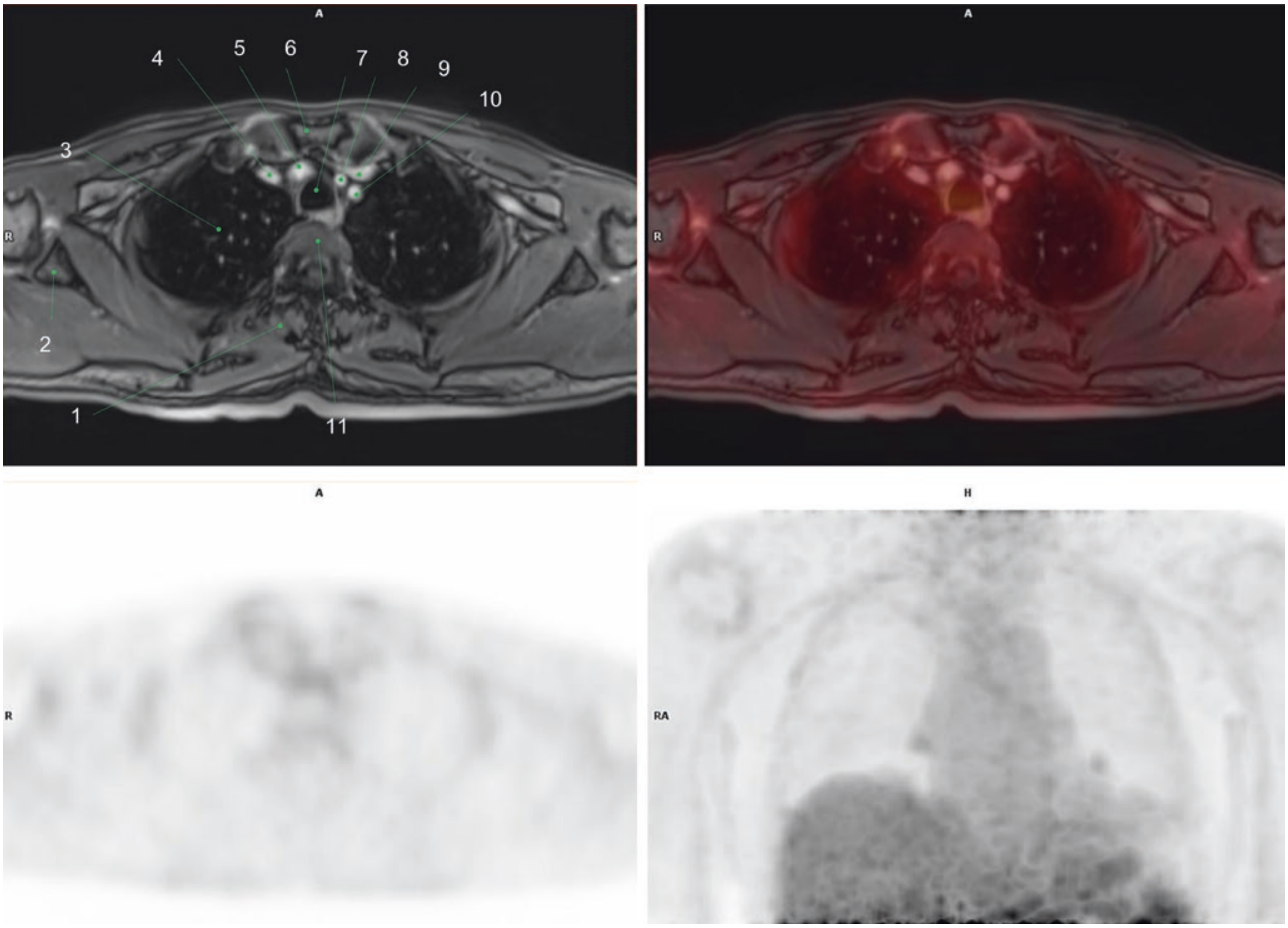

Fig. 16 1. Right erector spinae muscle
2. Right glenoid, scapula
3. Lung RUL
4. Right brachiocephalic vein
5. Right brachiocephalic artery
6. Sternal manubrium
7. Trachea
8. Left common carotid artery
9. Left brachiocephalic vein
10. Left subclavian artery
11. Thoracic vertebral body

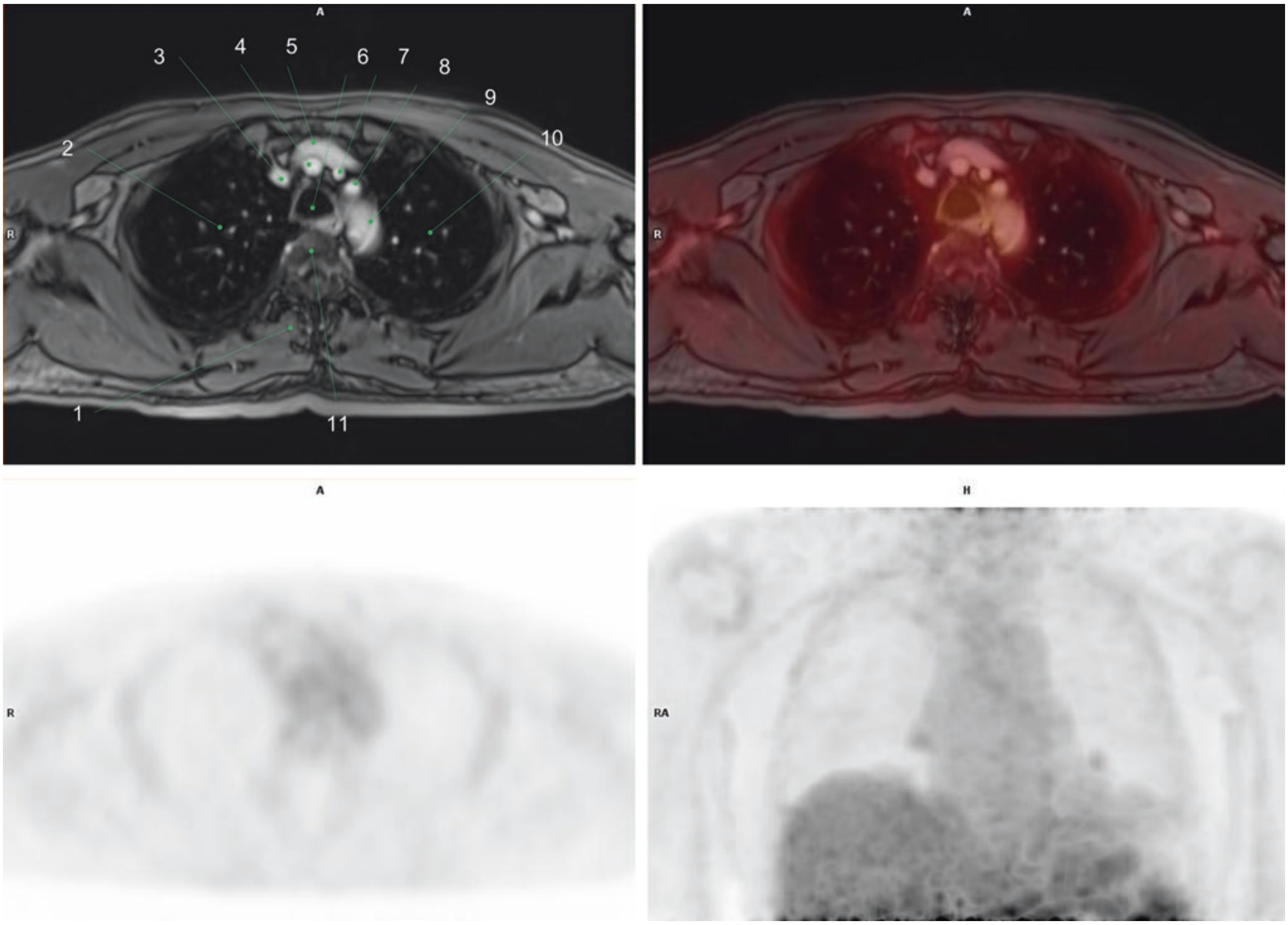

Fig. 17 1. Right erector spinae muscle
2. Lung RUL
3. Right brachiocephalic vein
4. Right brachiocephalic artery
5. Left brachiocephalic vein
6. Trachea
7. Left common carotid artery
8. Left subclavian artery
9. Aortic arch
10. Lung left upper lobe (LUL)
11. Thoracic vertebral body

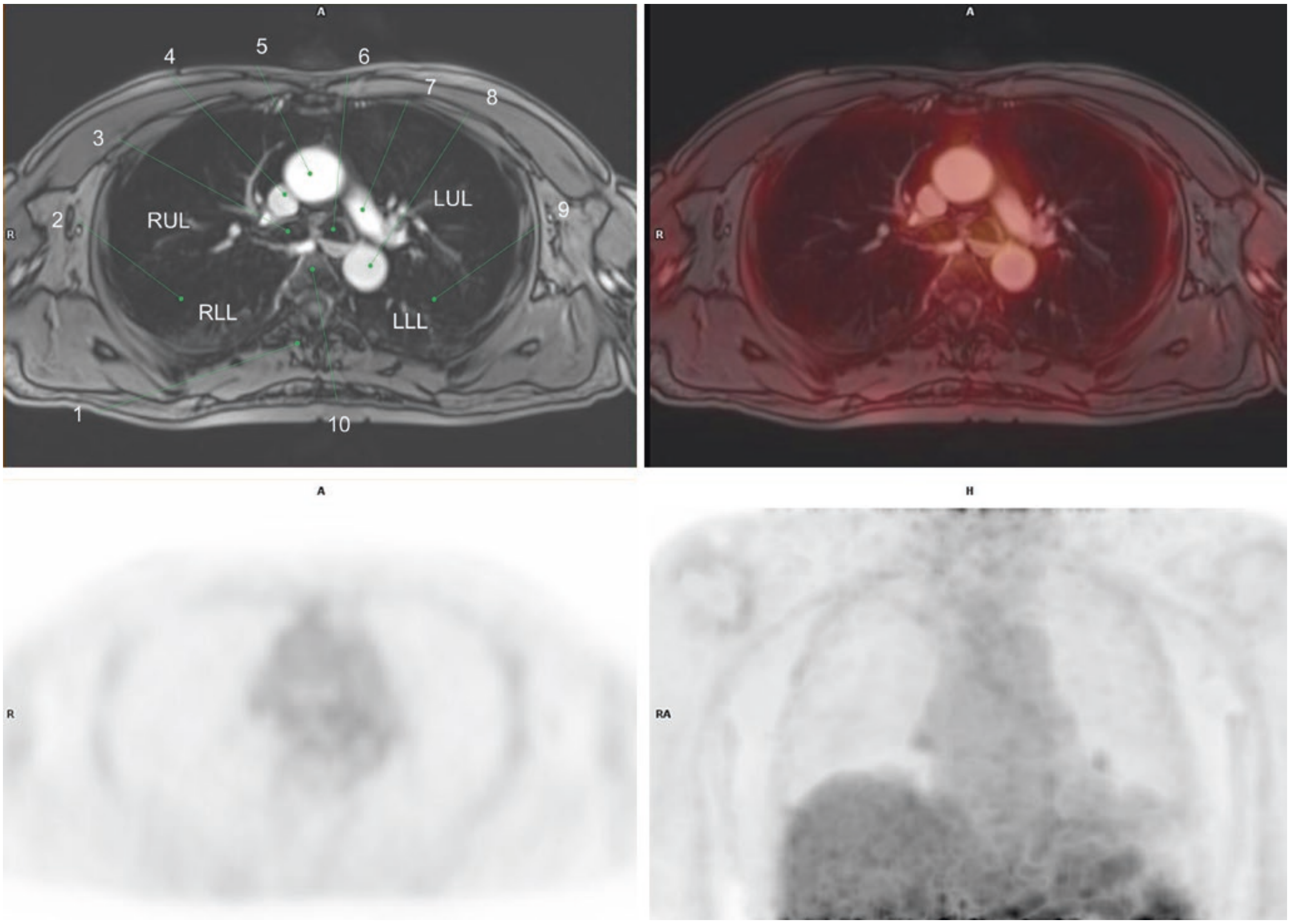

Fig. 18 1. Right erector spinae muscle
2. Right major fissure
3. Right main bronchus
4. Superior vena cava (SVC)
5. Ascending aorta
6. Left main bronchus
7. Left pulmonary artery
8. Descending aorta
9. Left lung fissure
10. Thoracic vertebral body

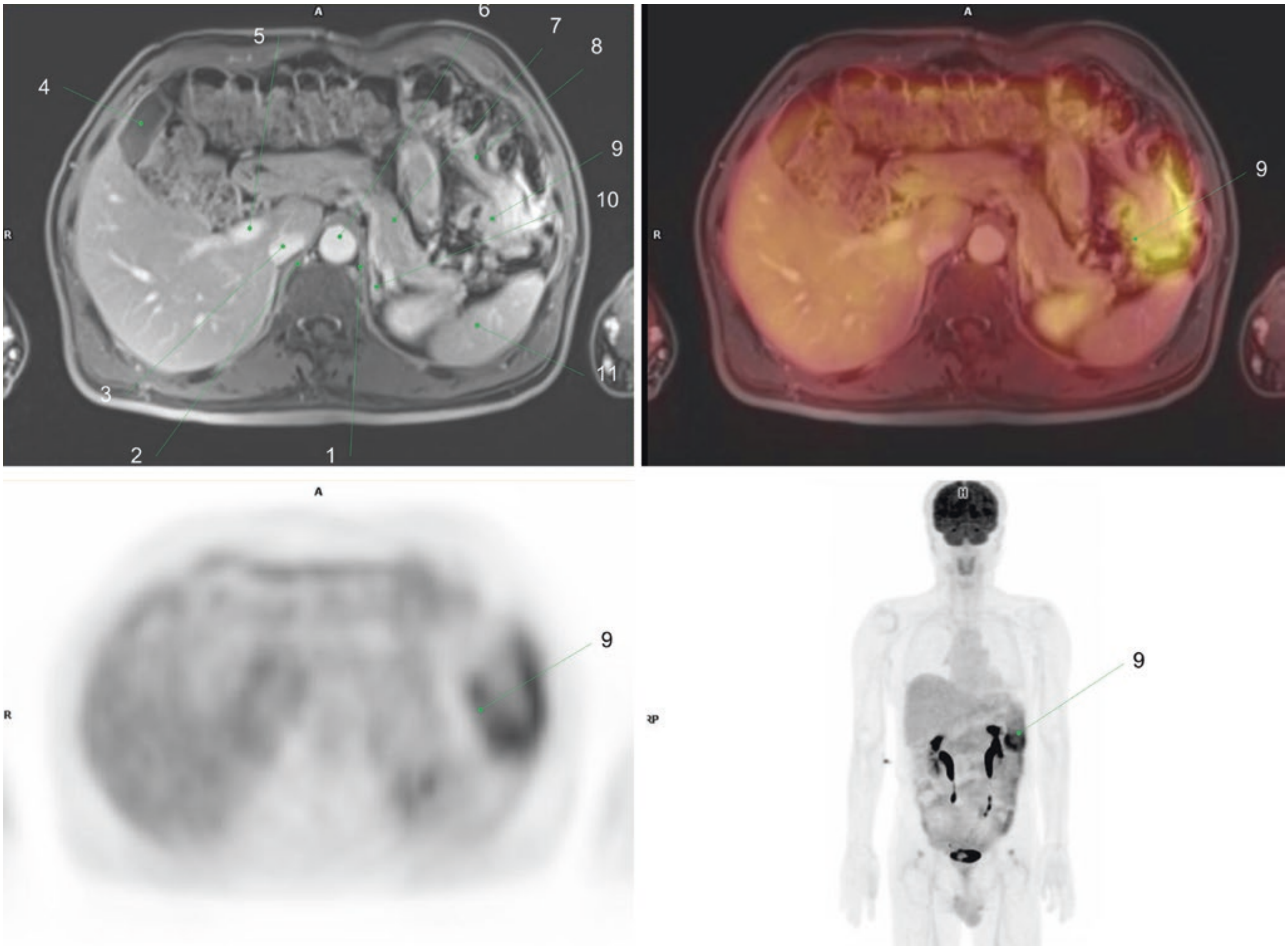

Fig. 19 1. Left diaphragmatic crura
2. Right diaphragmatic crura
3. Inferior vena cava
4. Gallbladder
5. Main portal vein
6. Abdominal aorta
7. Pancreas, body
8. Transverse colon
9. Descending colon
10. Left adrenal gland
11. Spleen

2.2 Case 2

Chest X-ray was performed on a 43-year-old woman due to a history of tuberculosis. A mediastinal mass was found, so evaluation with ^{18}F-FDG PET/MR was indicated. Images showed mild focal increased activity at an oval, well-defined mass in the anterior and superior mediastinum as the only finding. Posterior biopsy confirmed a low-grade thymoma, type A (Fig. 20) [29].

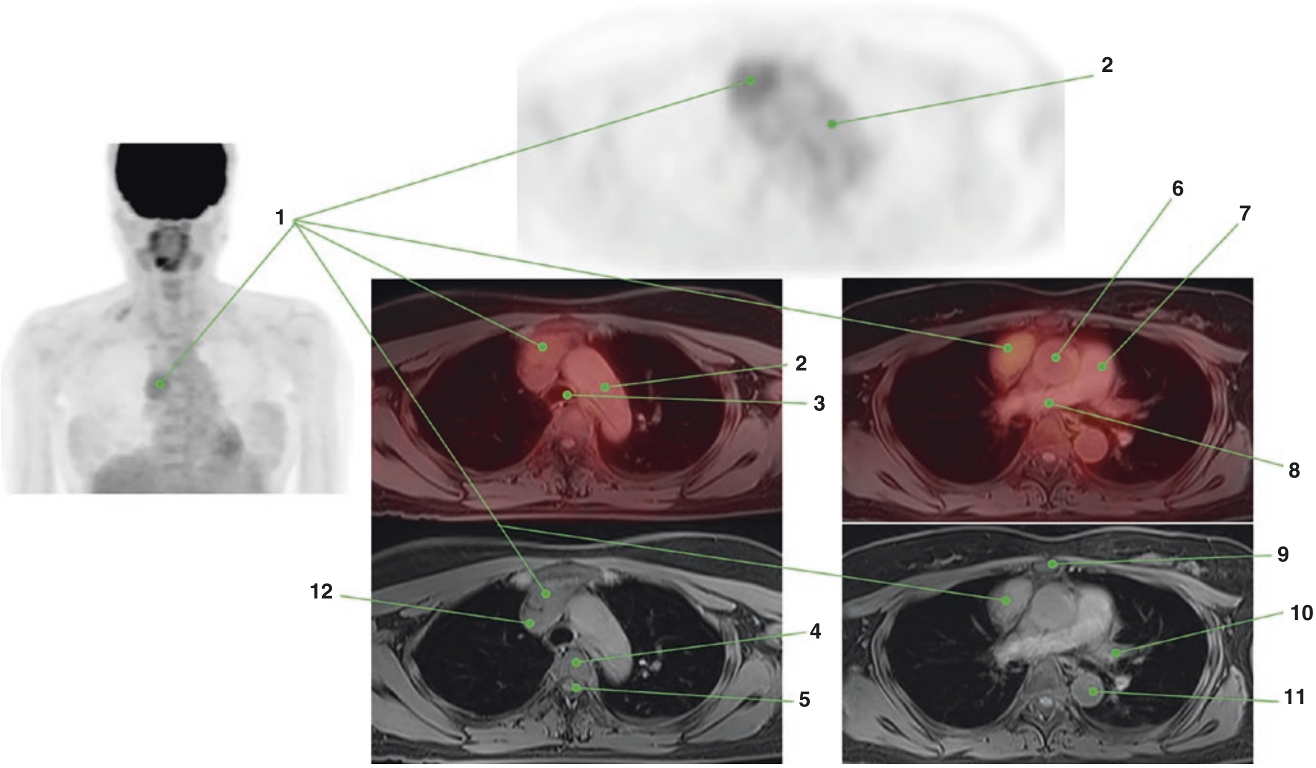

Fig. 20 1. Anterior mediastinal mass with mild, diffuse FDG uptake: low-grade thymoma
2. Aortic arch
3. Trachea
4. Thoracic vertebral body
5. Spinal cord
6. Ascending aorta
7. Main pulmonary artery
8. Right pulmonary artery
9. Sternum
10. Left pulmonary artery
11. Descending aorta
12. Superior vena cava

2.3 Case 3

A 39-year-old woman with family history of breast cancer (two sisters), who attended with a palpable mass in the right breast. Initial studies confirmed an invasive ductal carcinoma, so ^{18}F-FDG PET/MR was performed for staging. Images showed a metabolically active mass in the right breast with metastatic axillary lymph nodes in levels I and II. Intense FDG uptake was found in the left ventricular wall, probably related to poor fasting (Figs. 21 and 22).

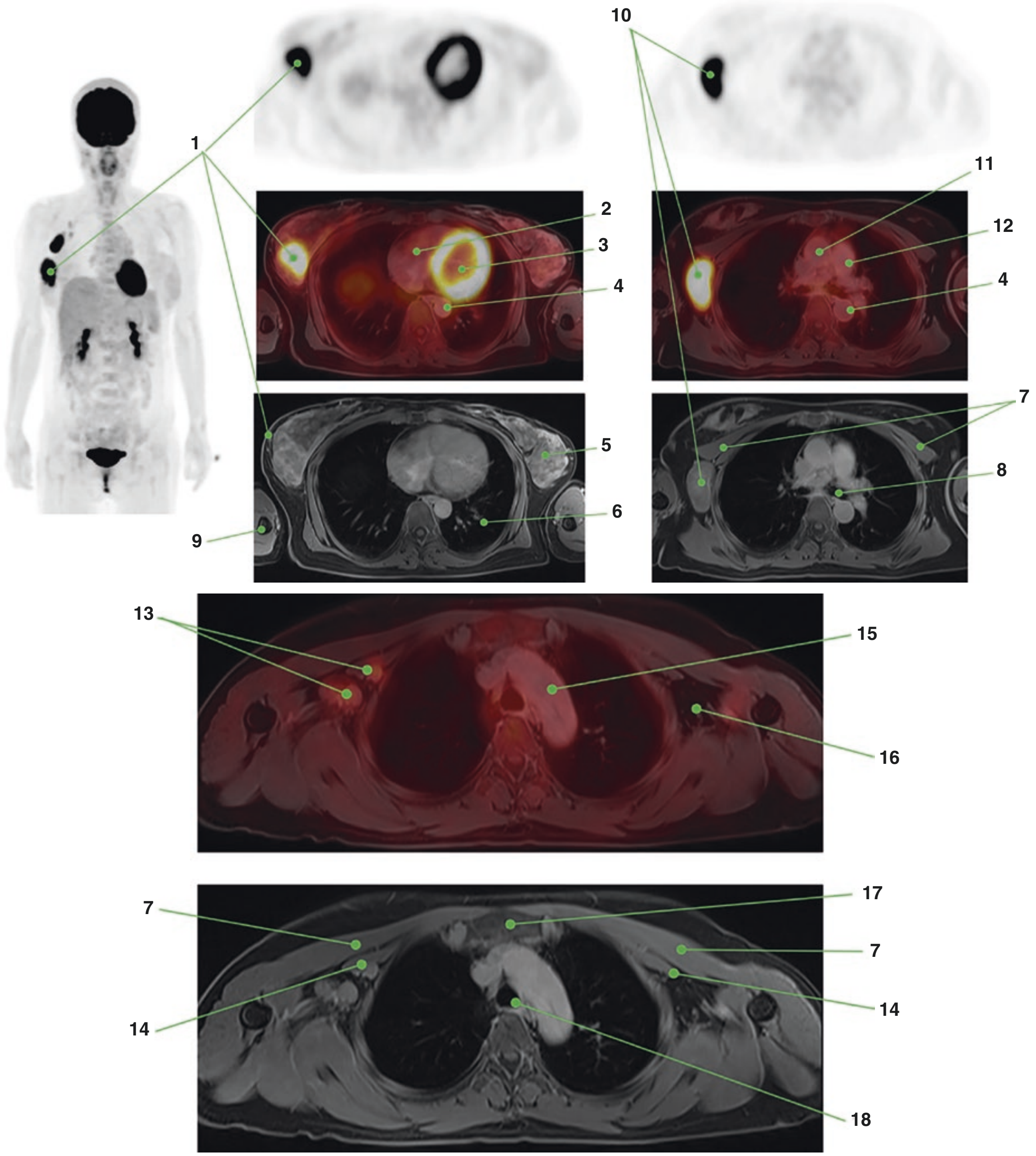

Figs. 21 and 22 1. Metabolically active tumor in the right breast
2. Right ventricle
3. Left ventricle (diffuse myocardial uptake)
4. Descending aorta
5. Left breast normal fibroglandular tissue
6. Lung, left lower lobe
7. Pectoralis major muscles
8. Left main bronchus
9. Right humeral shaft
10. Hypermetabolic LN metastasis, right axillary level I
11. Ascending aorta
12. Main pulmonary artery
13. Mild hypermetabolic LN metastasis, right axillary level II
14. Right pectoralis minor muscle
15. Aortic arch
16. Left axillary fossa
17. Sternum
18. Trachea

3 Abdomen and Pelvis

3.1 Case 1

A 60-year-old male patient with weight loss of 10 kg over 7 months. Endoscopy and biopsy confirmed the diagnosis of a gastric adenocarcinoma, so ^{18}F-FDG PET/MR was done for initial staging. Images showed a hypermetabolic lesion along the lesser curvature of the stomach, corresponding to the primary tumor. Another focal lesion with increased activity was found in the liver S5, which was confirmed as a liver metastasis [30]. As an incidental finding, a cystic lesion was observed in the left perineal soft tissues, which corresponded to a dermoid cyst (Figs. 23, 24, and 25).

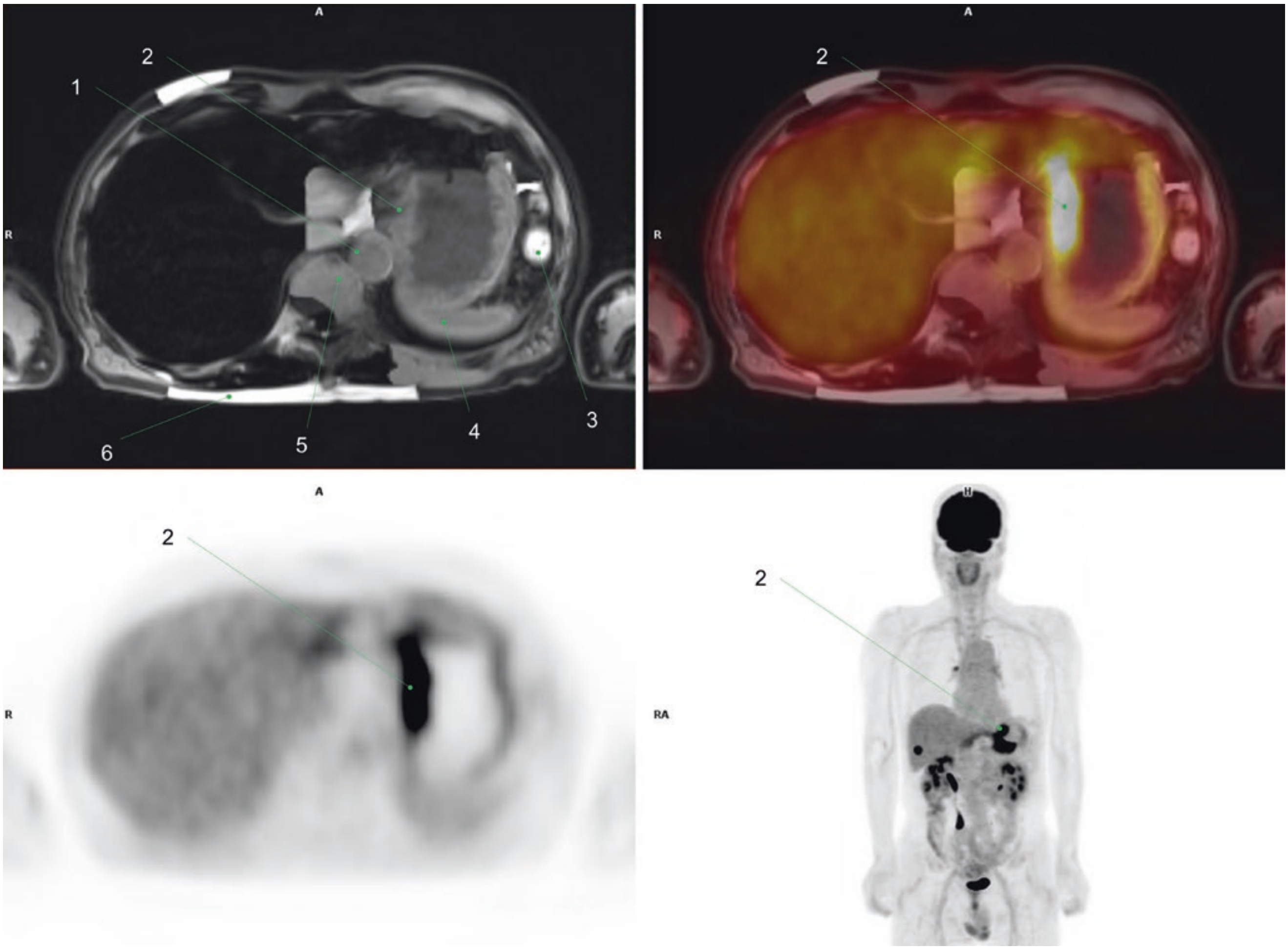

Fig. 23 1. Abdominal aorta
2. Metabolically active stomach cancer in lesser curvature
3. Splenic flexure of the colon
4. Spleen
5. Thoracic vertebral body
6. Magnetic resonance artifact

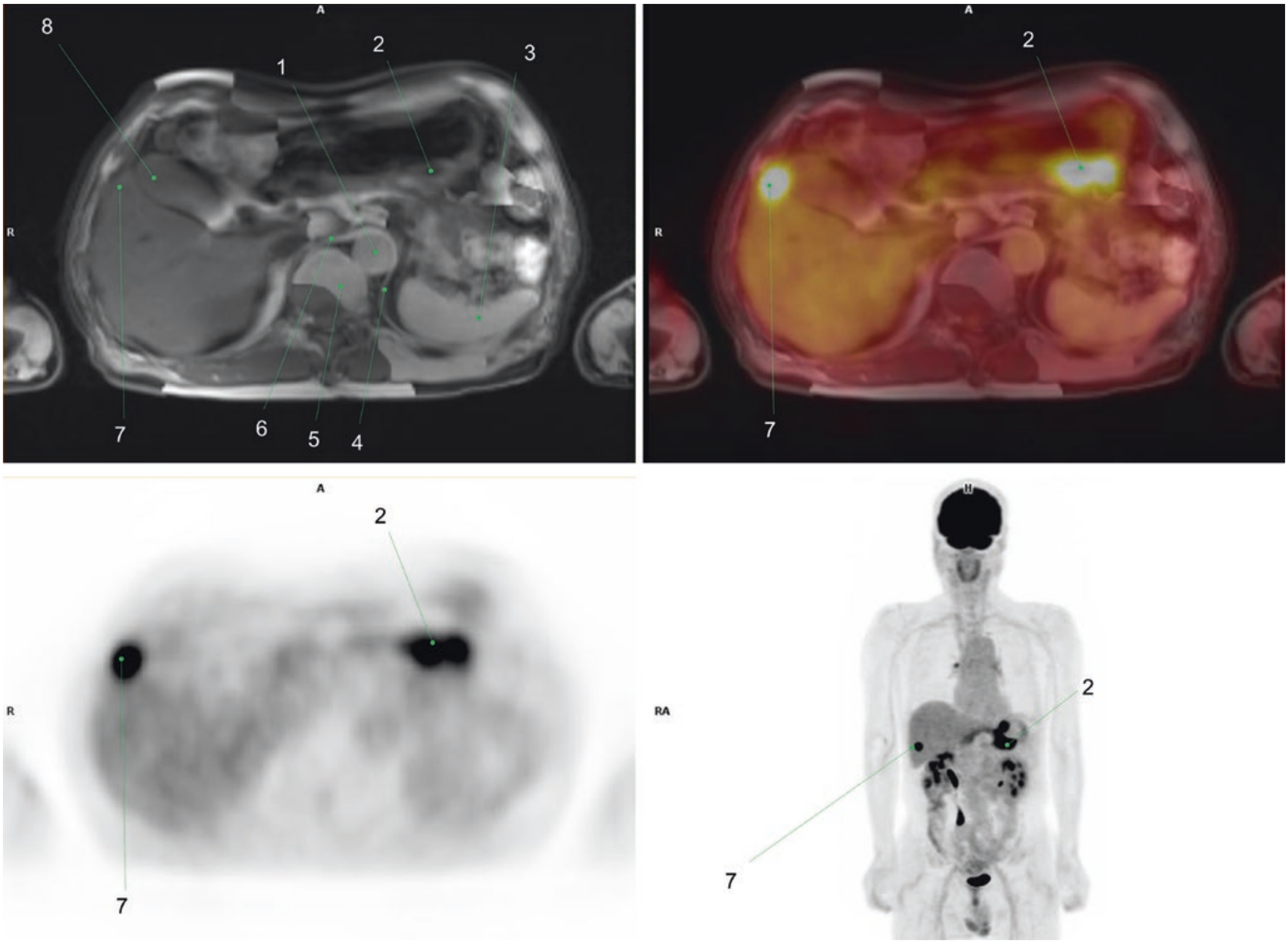

Fig. 24 1. Abdominal aorta
2. Metabolically active stomach cancer in lesser curvature
3. Spleen
4. Left diaphragmatic crura
5. Thoracic vertebral body
6. Right diaphragmatic crura
7. Metabolically active liver metastasis, S5
8. Gallbladder

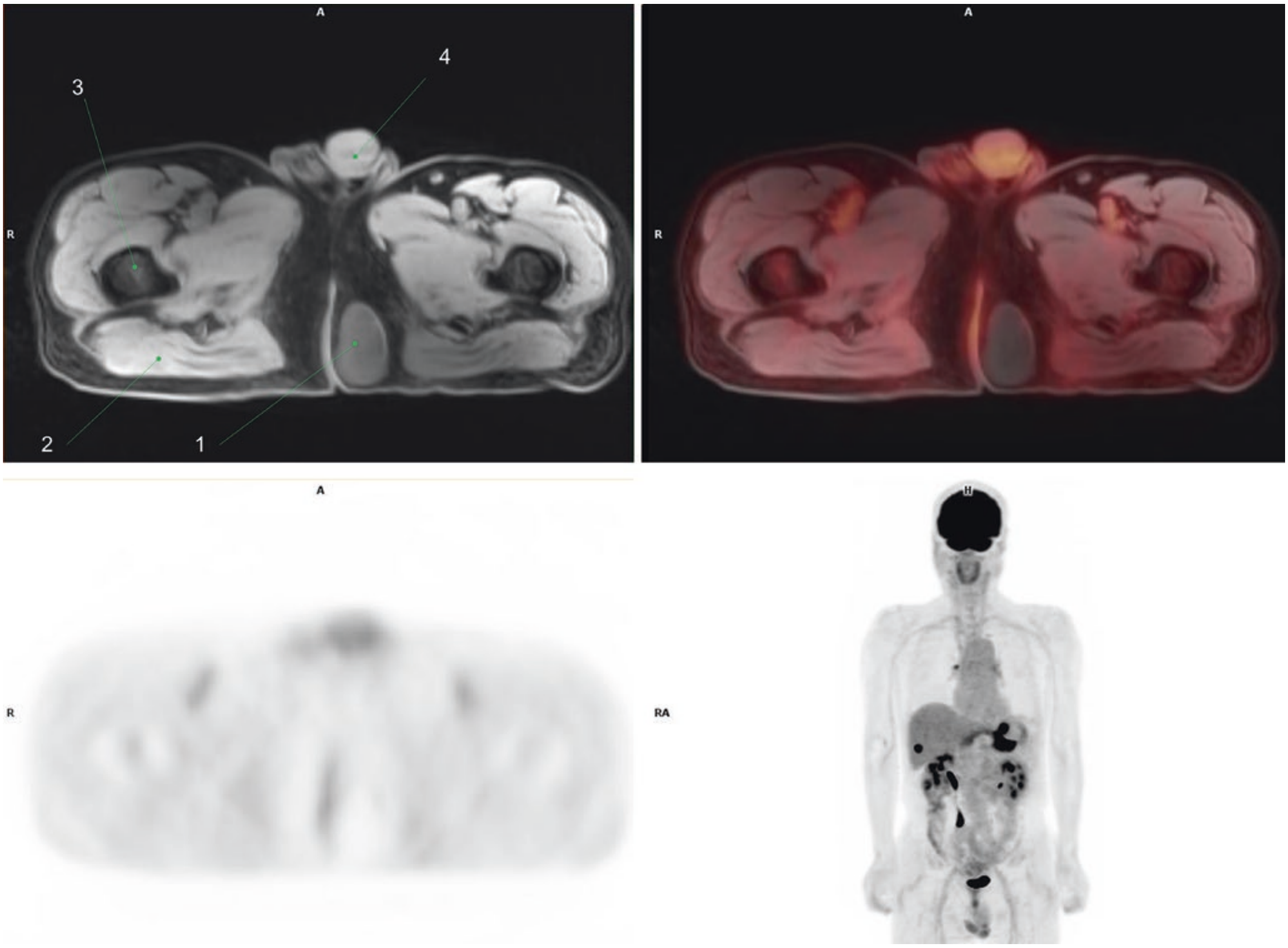

Fig. 25 1. Hypometabolic dermoid cyst in the left perineal area
2. Right gluteus maximus muscle
3. Right proximal femur
4. Penis

3.2 Case 2

A 69-year-old female patient with a history of right nephrectomy 10 years ago due to a renal liposarcoma, who presented with abdominal discomfort. Endoscopy was done and revealed a signet-ring cell gastric cancer, so ^{18}F-FDG PET/MR was done for initial staging. Focal increased activity was observed in the gastric antrum corresponding to the primary tumor, as well as in several enlarged lymph nodes (LNs) in the lesser curvature area, metastatic. Additionally, mild, diffuse, increased activity was found in fat-attenuating lesions at the retrocrural area and peritoneum, which were consistent with recurred liposarcoma (Figs. 26 and 27) [30, 31].

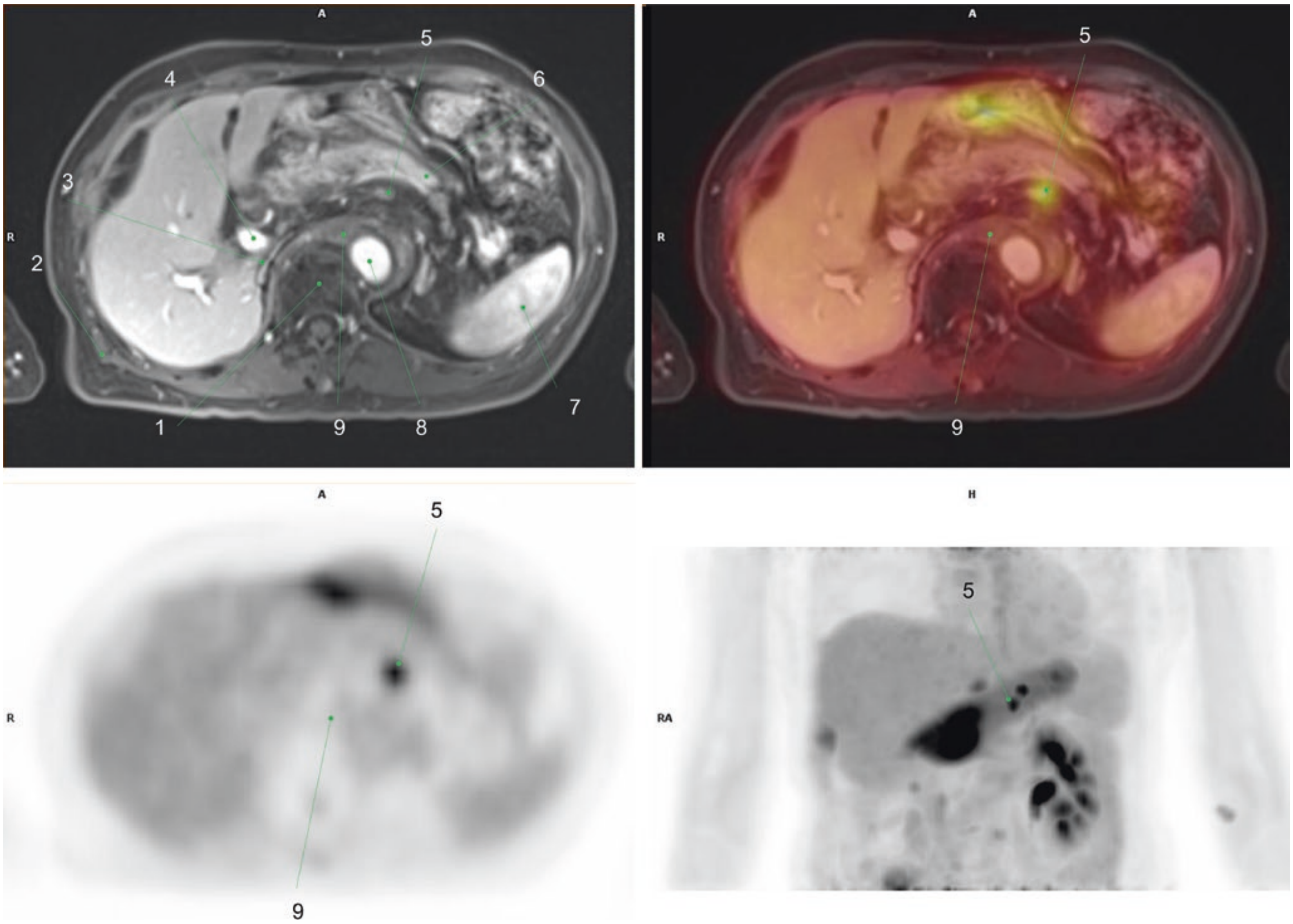

Fig. 26 1. Thoracic vertebral body
2. Right latissimus dorsi muscle
3. Collapsed inferior vena cava
4. Main portal vein
5. Hypermetabolic perigastric lymph node metastasis
6. Stomach, body
7. Spleen
8. Abdominal aorta
9. Mild, metabolically active recurred liposarcoma in retrocrural area

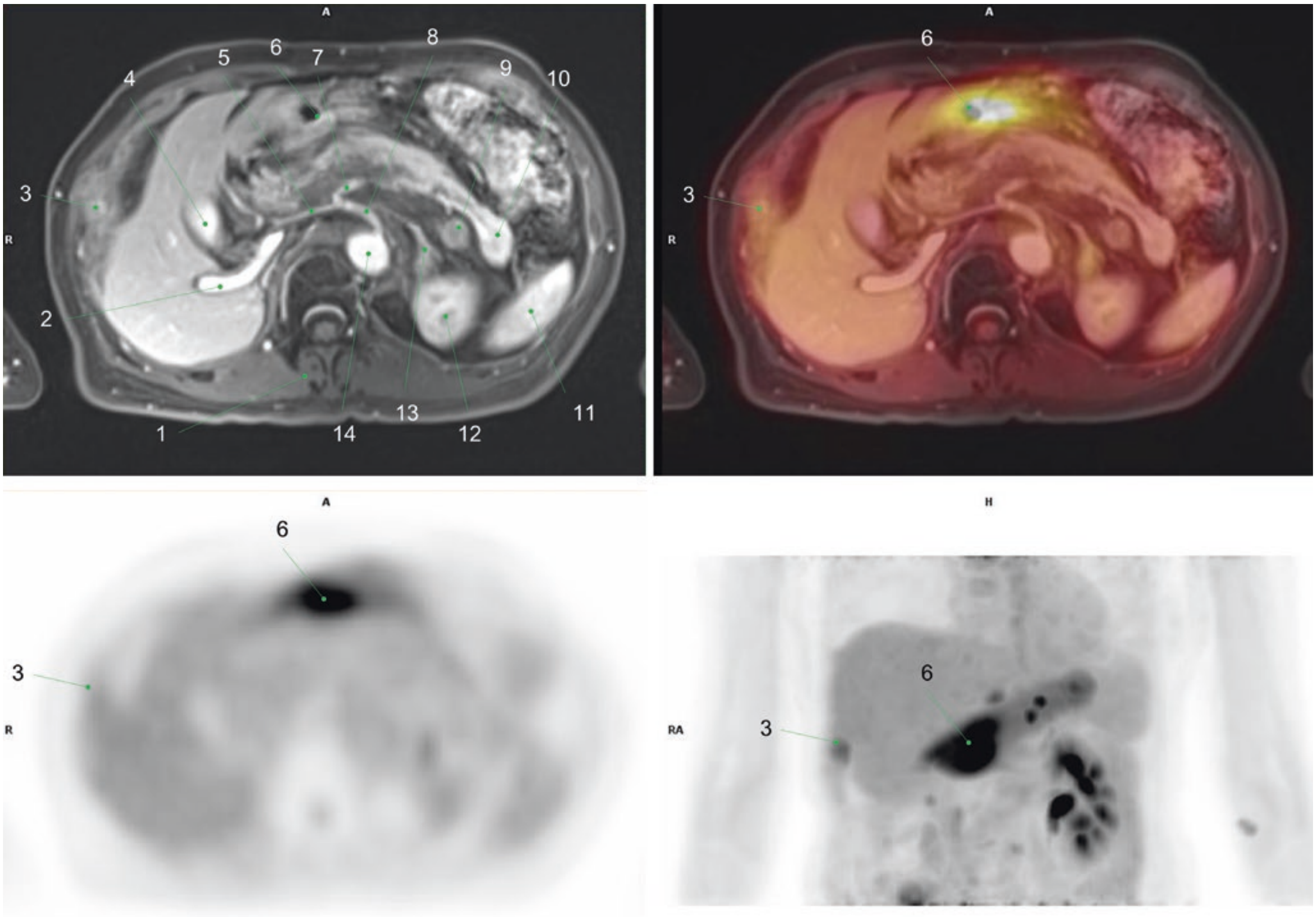

Fig. 27 1. Right paraspinal muscles
2. Right portal vein
3. Mild metabolically active peritoneal lesion, corresponding to recurred liposarcoma
4. Gallbladder
5. Common hepatic artery
6. Metabolically active stomach cancer, antrum
7. Splenic artery
8. Celiac trunk
9. Mild metabolically active peritoneal lesion, corresponding to recurred liposarcoma
10. Pancreatic tail
11. Spleen
12. Left kidney, inferior pole
13. Left adrenal gland
14. Abdominal aorta

3.3 Case 3

A 74-year-old male patient with persistent abdominal pain during the last 3 months. Ultrasound was performed finding a suspicious mass in the gallbladder, so he was referred for ^{18}F-FDG PET/MR evaluation. Images showed a marked hypermetabolic mass in the gallbladder fundus with intermediate, heterogeneous signal intensity in T2WI, consistent with a primary adenocarcinoma. Hypermetabolic liver invasion was excluded, as well as distant metastases (Fig. 28) [32].

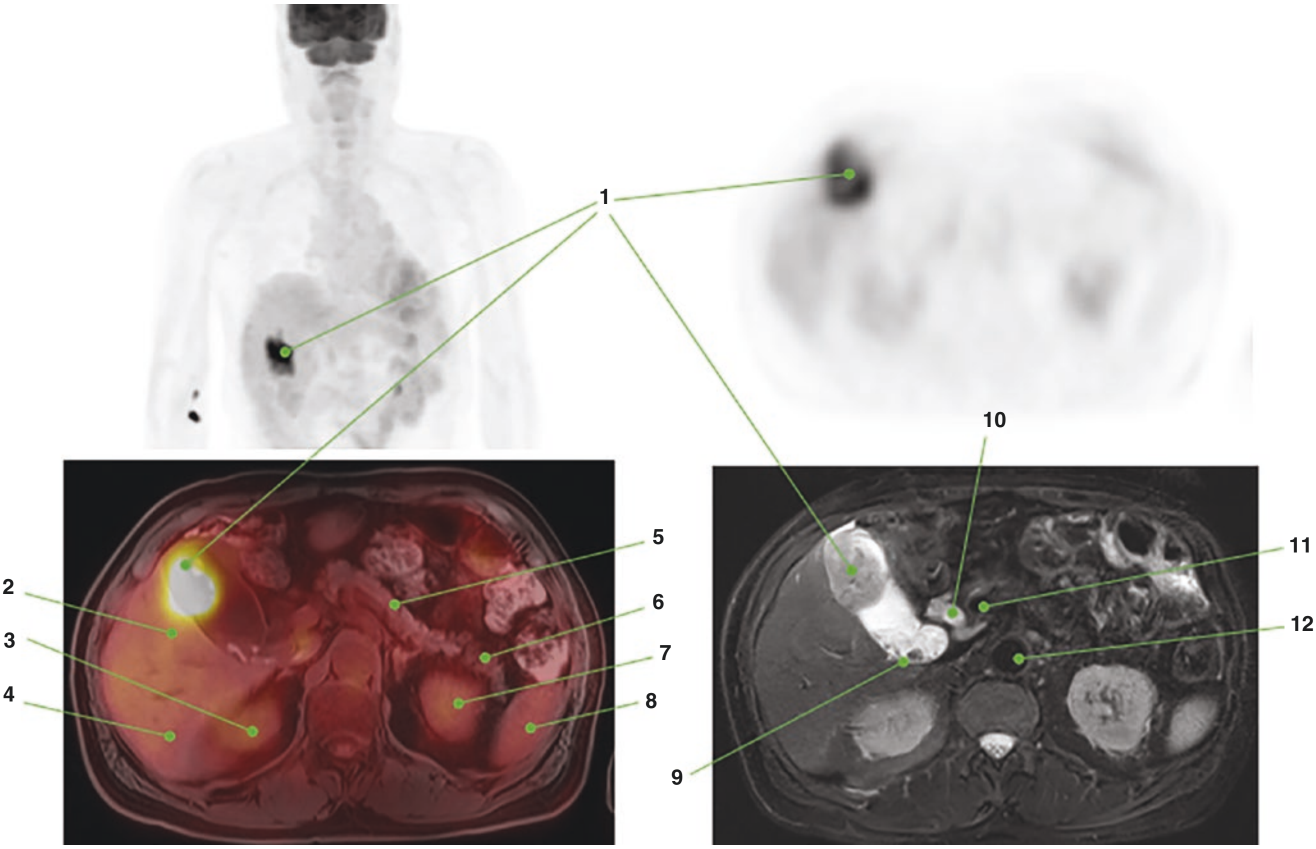

Fig. 28 1. Metabolically active gallbladder tumor
2. Liver segment 5
3. Right kidney, superior pole
4. Liver segment 6
5. Pancreatic body
6. Pancreatic tail
7. Left kidney, superior pole
8. Spleen, inferior pole
9. Gallbladder stones
10. Cystic duct
11. Portal vein
12. Abdominal aorta

3.4 Case 4

A 42-year-old patient, hepatitis B virus carrier, underwent abdominal ultrasonography for a routine health check. A liver mass was found, so ^{18}F-FDG PET/MR was indicated for further evaluation. Images showed moderate focal increased activity in the liver S7 at a lobulated mass with arterial enhancement and delayed washout, consistent with a hepatocarcinoma. The patient underwent right liver posterior sectionectomy and the final diagnosis was combined hepatocellular carcinoma (HCC) and cholangiocarcinoma (CCA), which explains the high FDG uptake of the lesion (Fig. 29) [33].

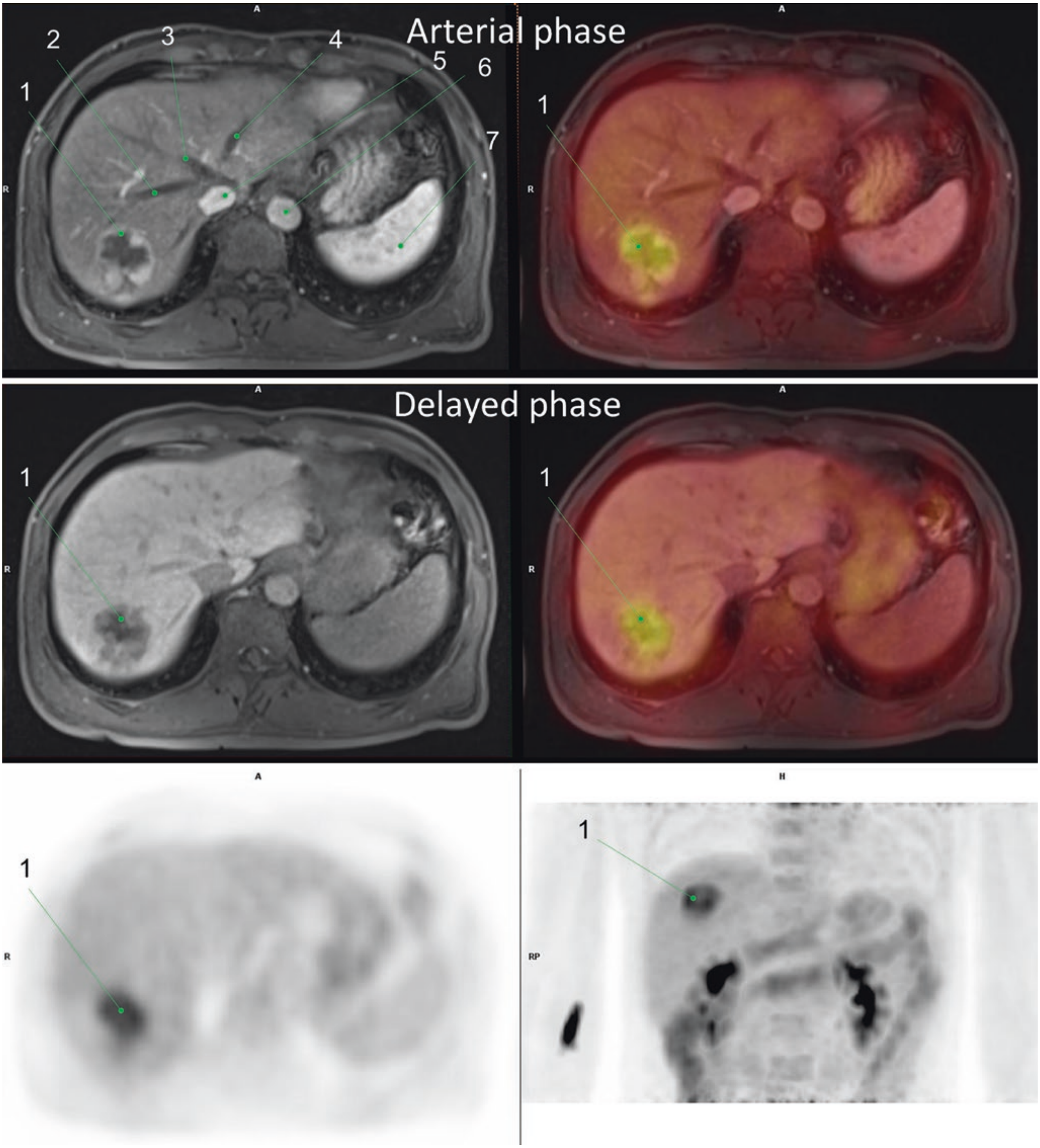

Fig. 29 1. Metabolically active liver tumor with heterogeneous arterial enhancement and delayed washout
2. Right hepatic vein
3. Middle hepatic vein
4. Left hepatic vein
5. Inferior vena cava
6. Abdominal aorta
7. Spleen

3.5 Case 5

A 58-year old patient with a history of a rare liver schwannoma, who presented with abdominal mass. ^{18}F-FDG PET/MR was done to search for malignant transformation. Images showed mild focal increased activity at the solid component of a complex irregular mass in the liver dome, which also showed heterogeneous signal intensity and delayed enhancement. Excisional biopsy was done, and a schwannoma with malignant transformation was confirmed (Figs. 30 and 31) [34].

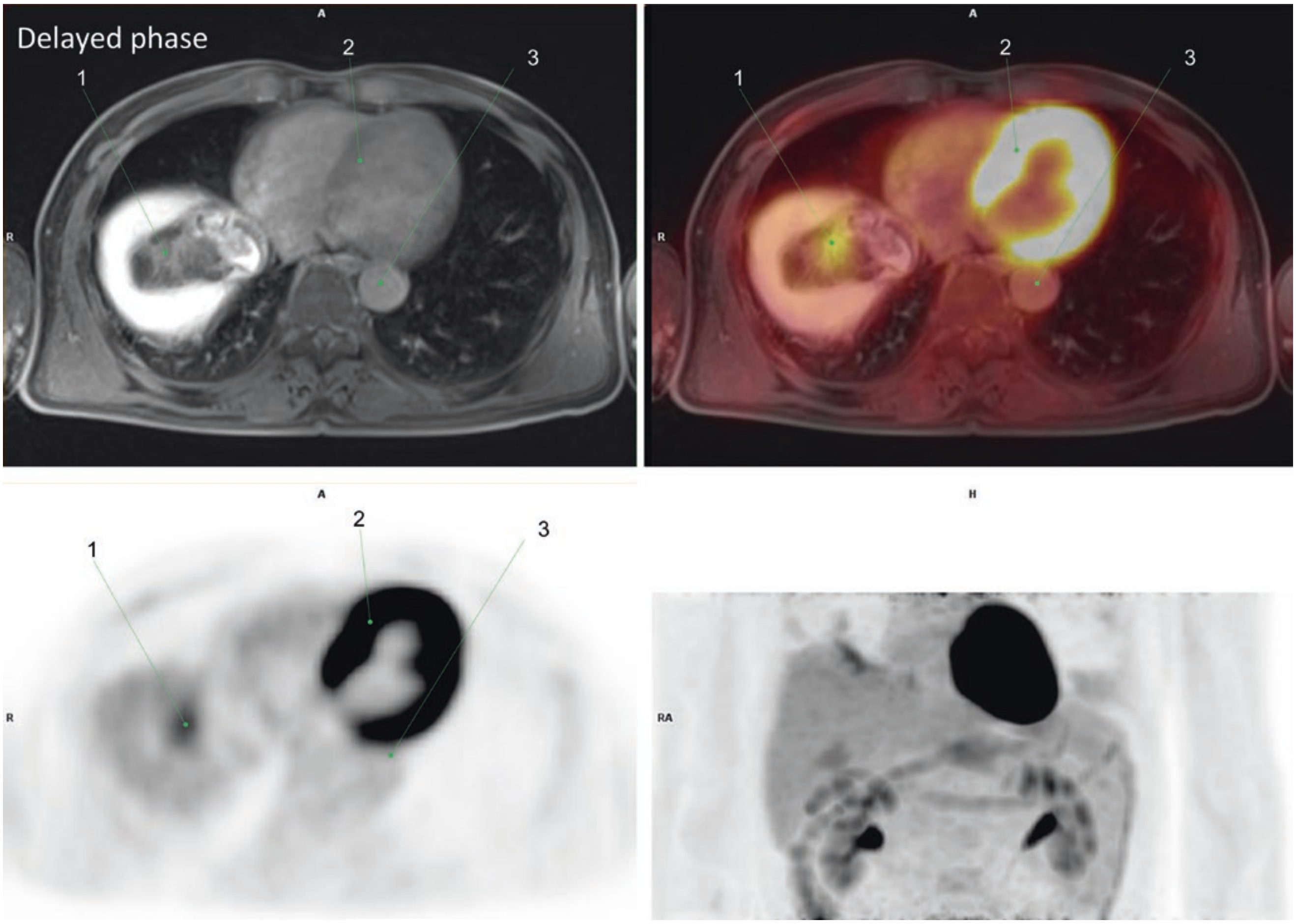

Fig. 30 1. Metabolically active liver schwannoma with delayed enhancement and central necrosis
2. Physiologic myocardial uptake, left ventricle
3. Descending aorta

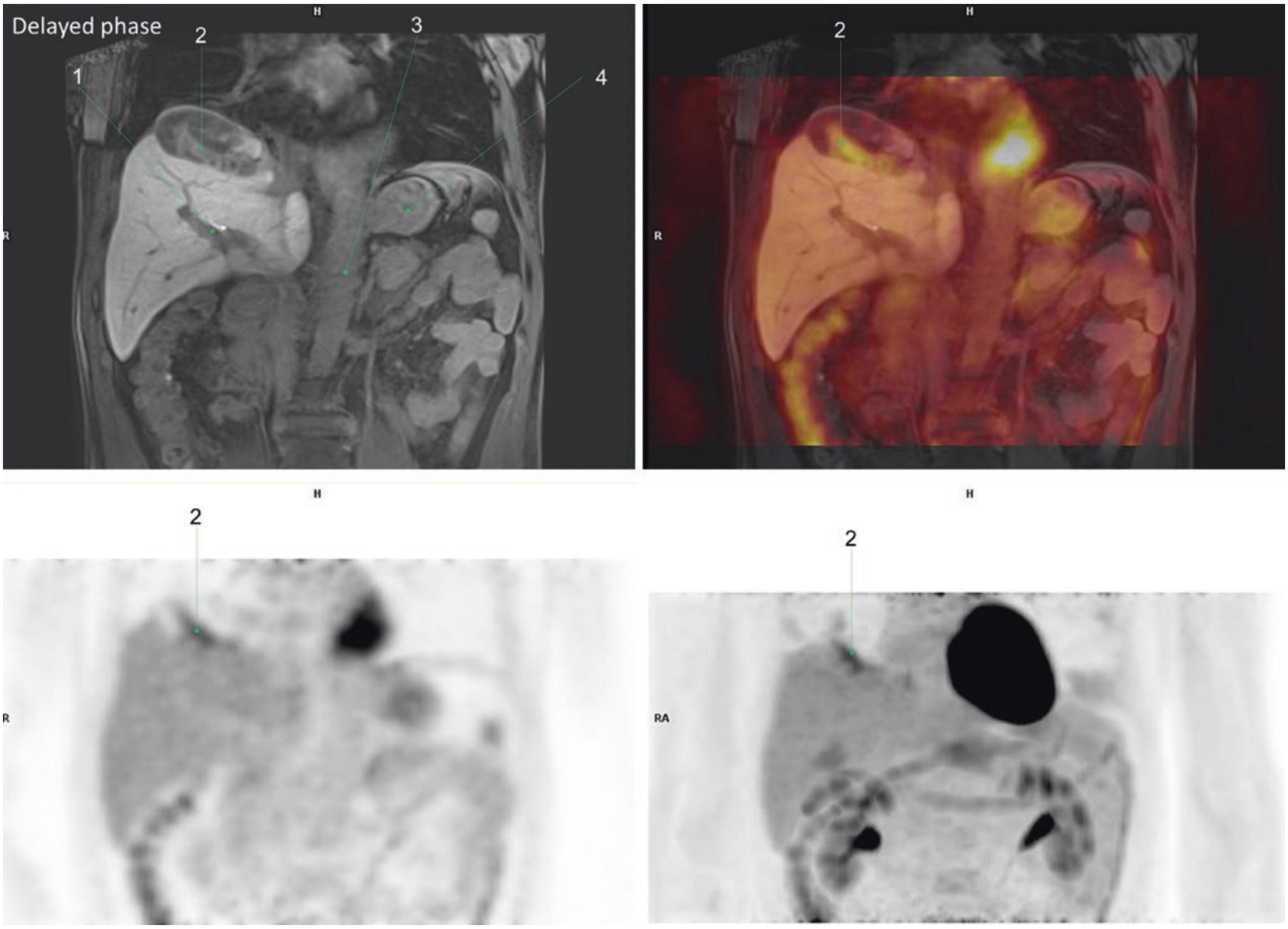

Fig. 31 1. Main portal vein
2. Metabolically active liver schwannoma with delayed enhancement and central necrosis
3. Abdominal aorta
4. Stomach

3.6 Case 6

A 72-year-old woman with recurrent abdominal pain, weight loss, and fever. Initial studies confirmed the diagnosis of a pancreatic tail adenocarcinoma and due to the suspicion of liver metastases, ^{18}F-FDG PET/MR was indicated. Images showed focal increased activity in a hypovascular pancreatic tail mass consistent with the primary tumor; due to the location of the lesion, no dilation of the main pancreatic duct was observed. Additionally, multiple focal hypermetabolic liver lesions were identified in the right hepatic lobe, corresponding to metastasis (Fig. 32) [32].

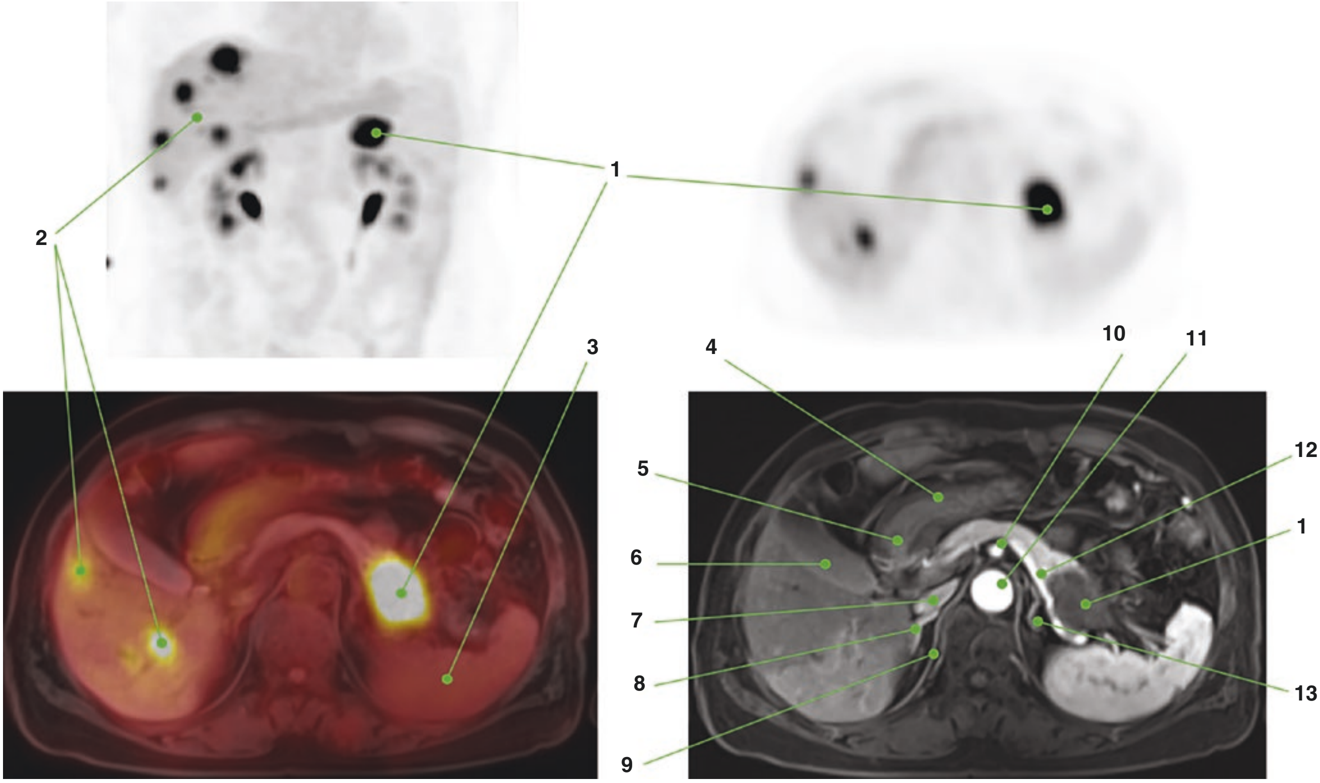

Fig. 32 1. Metabolically active pancreatic tail tumor
2. Multiple hypermetabolic liver metastasis in the right hepatic lobe
3. Spleen
4. Gastric antrum
5. Pylorus
6. Gallbladder
7. Inferior vena cava
8. Right adrenal gland
9. Right diaphragmatic crus
10. Superior mesenteric artery
11. Abdominal aorta
12. Splenic artery
13. Left adrenal gland

3.7 Case 7

A 69-year-old woman with persistent abdominal pain and distention. Abdominal ultrasound showed biliary dilatation and a suspicious pancreatic mass. ^{18}F-FDG PET/MR was done finding a hypermetabolic mass in the pancreatic head with dilatation of the main pancreatic duct and atrophy of the distal pancreatic parenchyma, typical findings of an adenocarcinoma at this location. No metabolically active metastases were detected (Fig. 33) [32].

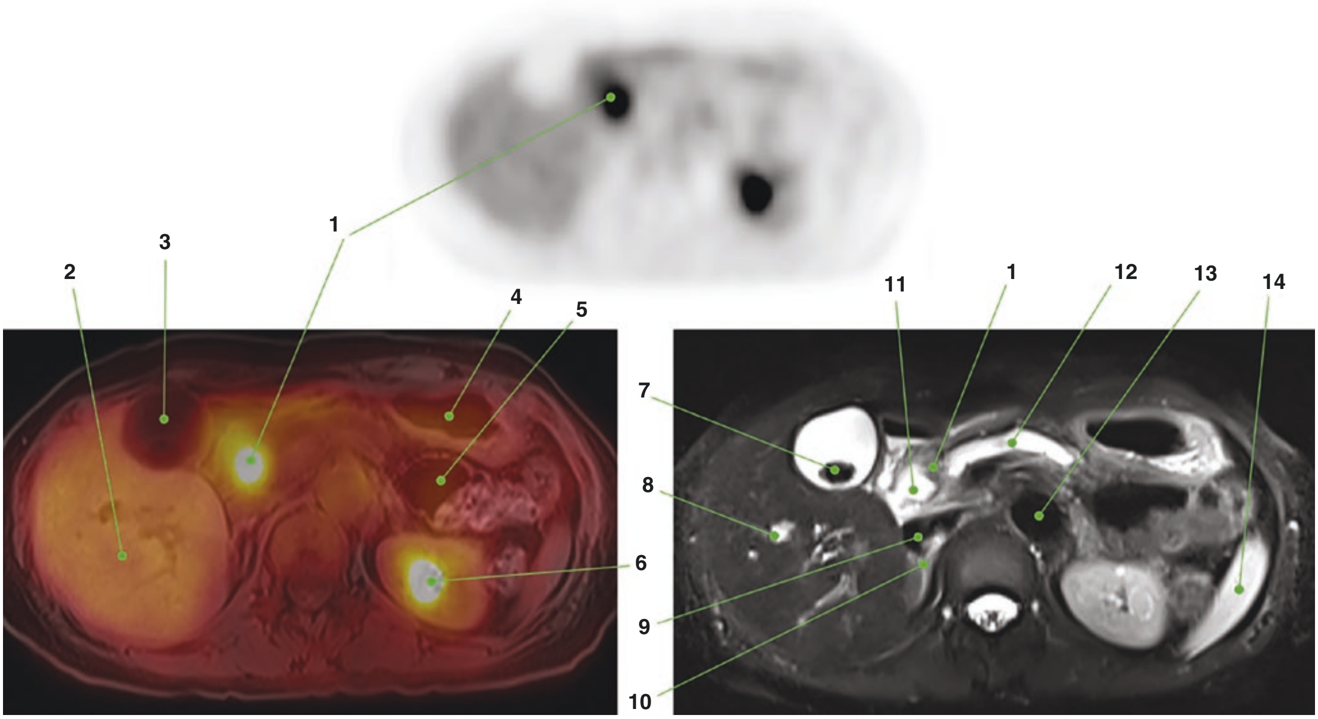

Fig. 33 1. Marked metabolically active pancreatic head adenocarcinoma
2. Right hepatic lobe
3. Gallbladder
4. Stomach
5. Transverse colon
6. Left kidney, upper pole
7. Gallbladder stone
8. Intrahepatic biliary duct dilation
9. Inferior vena cava
10. Right adrenal gland
11. Common bile duct, distal portion
12. Main pancreatic duct dilatation
13. Abdominal aorta
14. Spleen

3.8 Case 8

An 80-year-old woman with bloating, heaviness, and abdominal distention. Endoscopy was done finding a prominent mass in the stomach, so ^{18}F-FDG PET/MR was performed. Images showed slight and diffuse increased activity in a prominent rounded and very well-defined mass at the stomach, with heterogeneous contrast enhancement due to the presence of necrosis. Surgical resection of the lesion was done, and the final diagnosis was a low-grade gastrointestinal stromal tumor (GIST), as suspected (Fig. 34) [35].

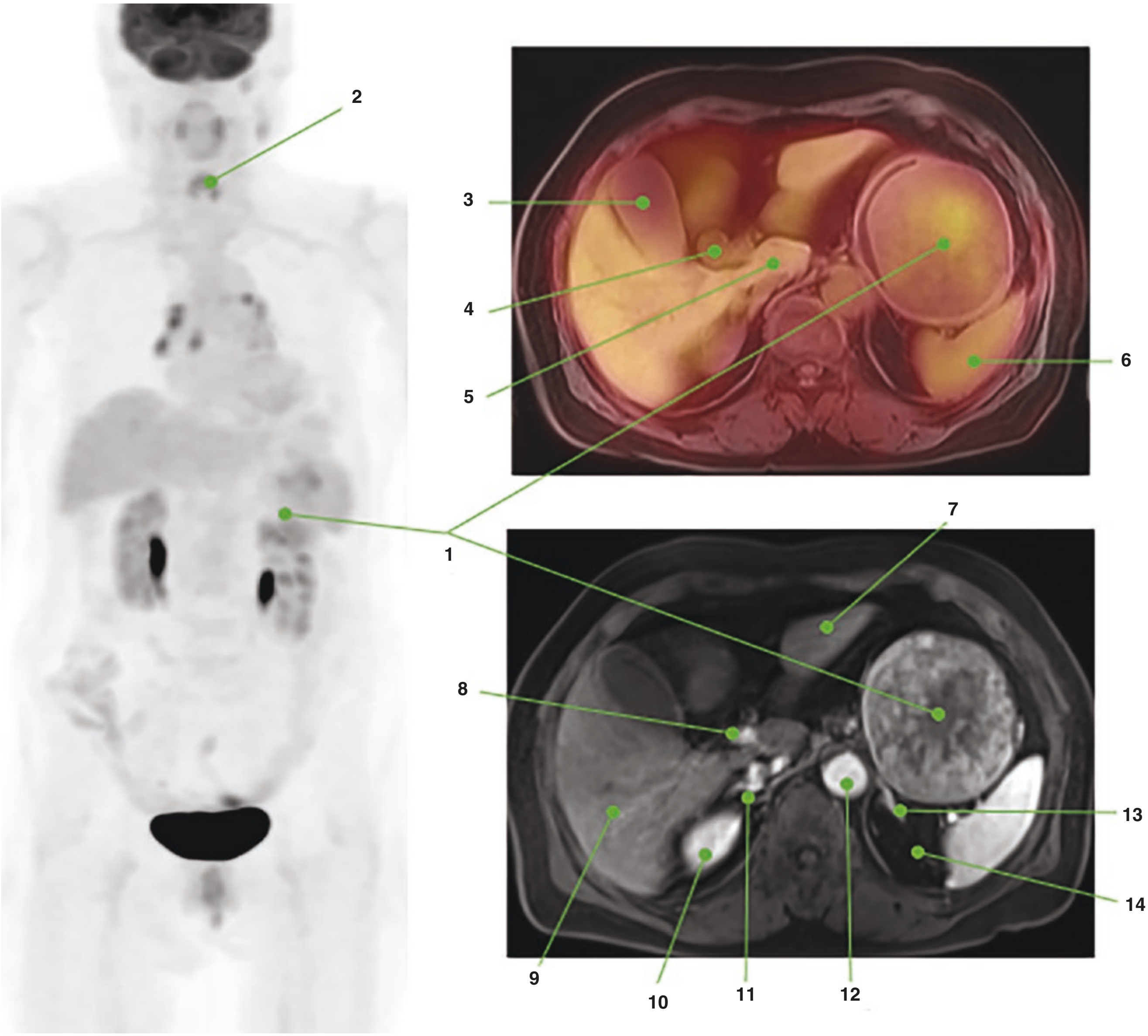

Fig. 34 1. Metabolically active gastric GIST
2. Physiologic activity in the vocal cords
3. Gallbladder
4. Common bile duct
5. Caudate lobe
6. Spleen
7. Left hepatic lobe, segment 3 (III)
8. Common hepatic artery
9. Right hepatic lobe, segment 6 (VI)
10. Right kidney, inferior pole
11. Right adrenal gland
12. Abdominal aorta
13. Left adrenal gland
14. Left perirenal space

3.9 Case 9

A 59-year-old man with a 3-month history of gradually increasing rectal bleeding. Colonoscopy was performed finding a circumferential mass in the sigmoid colon, consistent with an adenocarcinoma. During initial staging, liver metastases were suspected, so ^{18}F-FDG PET/MR was performed. Images show intense FDG uptake in the sigmoid colon at the primary tumor, without hypermetabolic pelvic or retroperitoneal lymph nodes. However, multiple metabolically active liver metastases were identified in both lobes (Fig. 35) [36].

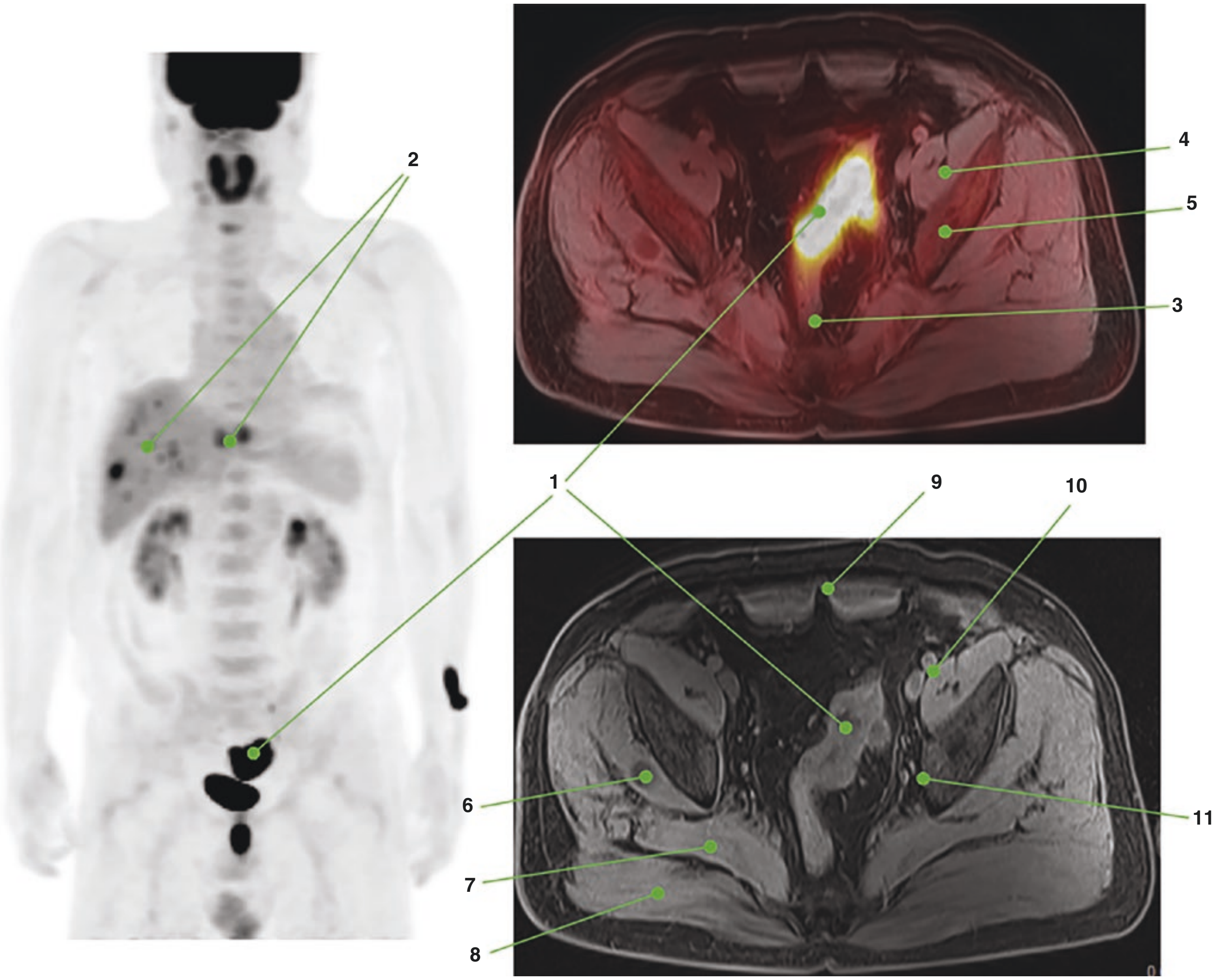

Fig. 35 1. Metabolically active sigmoid colon adenocarcinoma
2. Multiple hypermetabolic liver metastases in both lobes
3. Rectosigmoid junction
4. Left iliopsoas muscle
5. Left iliac bone
6. Right gluteus minimus muscle
7. Right gluteus medius muscle
8. Right gluteus maximus muscle
9. Rectus abdominis muscles
10. Left external iliac vessels
11. Left internal iliac vessels

3.10 Case 10

A 74-year-old man with prostate cancer, Gleason 8 (4 + 4), diagnosed with multiparametric MRI and transrectal biopsy. ^{18}F-Choline PET/CT was performed for staging and images showed focal increased activity in the primary tumor at the left peripheral zone of the prostate gland with exophytic extension to the recto-prostatic angle and probable involvement of the neurovascular bundle (see MRI correlation). Also, two different metastatic bone lesions were observed, one slightly hypermetabolic, ill-defined intramedullary lesion in the right ischial tuberosity, and other cortical sclerotic lesion in the left ischial tuberosity without FDG uptake (Fig. 36) [15].

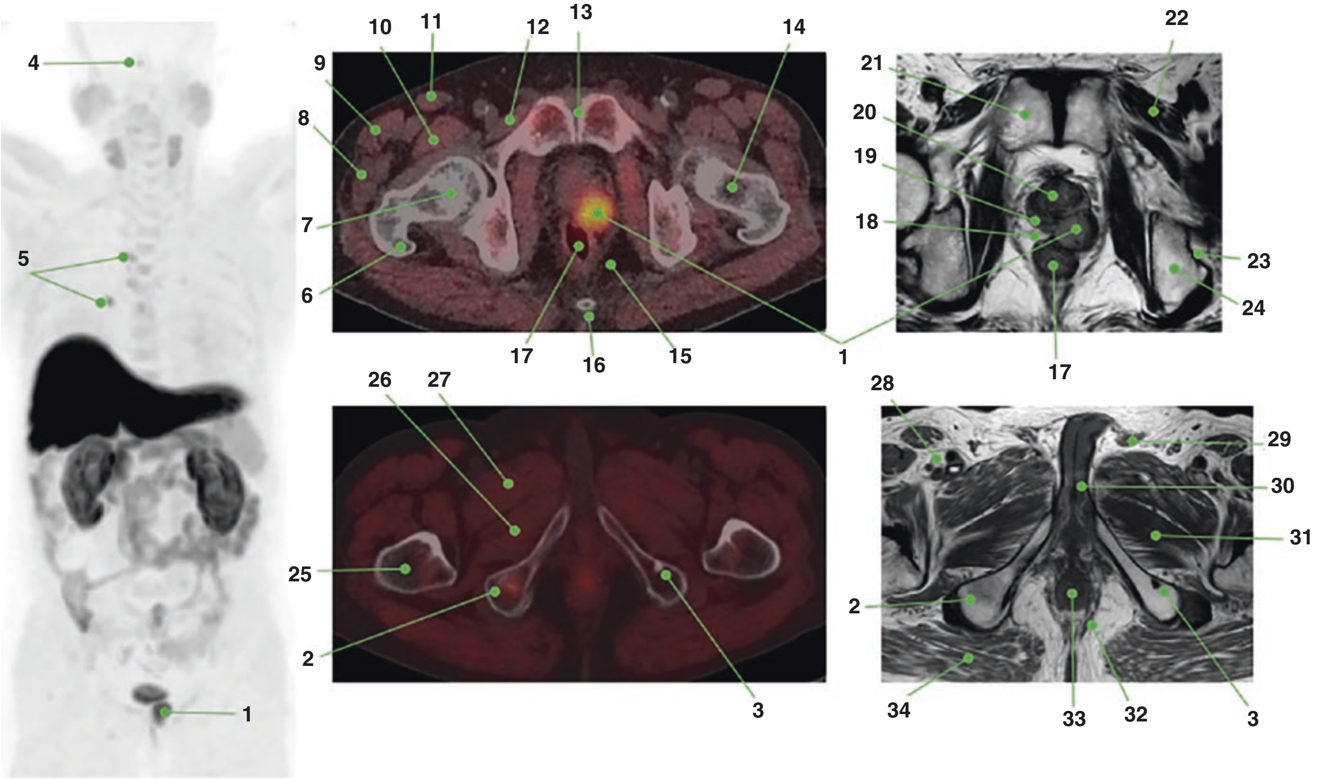

Fig. 36 1. Focal increased activity at primary prostate cancer in the left peripheral zone
2. Mild uptake in medullary bone metastasis
3. Sclerotic cortical bone metastasis without uptake
4. Pituitary gland
5. Mild metabolically active inflammatory lymph nodes
6. Right femur, greater trochanter
7. Right femoral head
8. Right vastus lateralis muscle
9. Right tensor fascia latae muscle
10. Right rectus femoris muscle
11. Right sartorius muscle
12. Right pectineus muscle
13. Pubic symphysis
14. Left femoral neck
15. Perirectal fat
16. Coccix
17. Rectum
18. Right recto-prostatic angle
19. Prostate gland, right peripheral zone
20. Prostate gland, transitional zone
21. Right pubic bone
22. Left pectineus muscle
23. Ischial tuberosity, cortical bone (T2WI hypointense)
24. Ischial tuberosity, medullary bone (T2WI hyperintense)
25. Right proximal femoral shaft
26. Right adductor magnus muscle
27. Right adductor brevis muscle
28. Right femoral vessels
29. Left spermatic cord
30. Base of penis
31. Left adductor magnus muscle
32. Left pubococcygeus muscle
33. Anal canal
34. Right gluteus maximus muscle

3.11 Case 11

A 41-year-old woman referred for ^{18}F-FDG PET/MR due to abnormal findings on her annual general checkup. At colonoscopy, a lobulated subepithelial mass was found on the anterior aspect of the rectum; there was no definite abnormal increased activity in the lesion, which was later confirmed as a leiomyoma. Also, a complex right adnexal cystic mass without abnormal increased FDG uptake was observed; the final diagnosis was a hemorrhagic cyst (Figs. 37 and 38) [36].

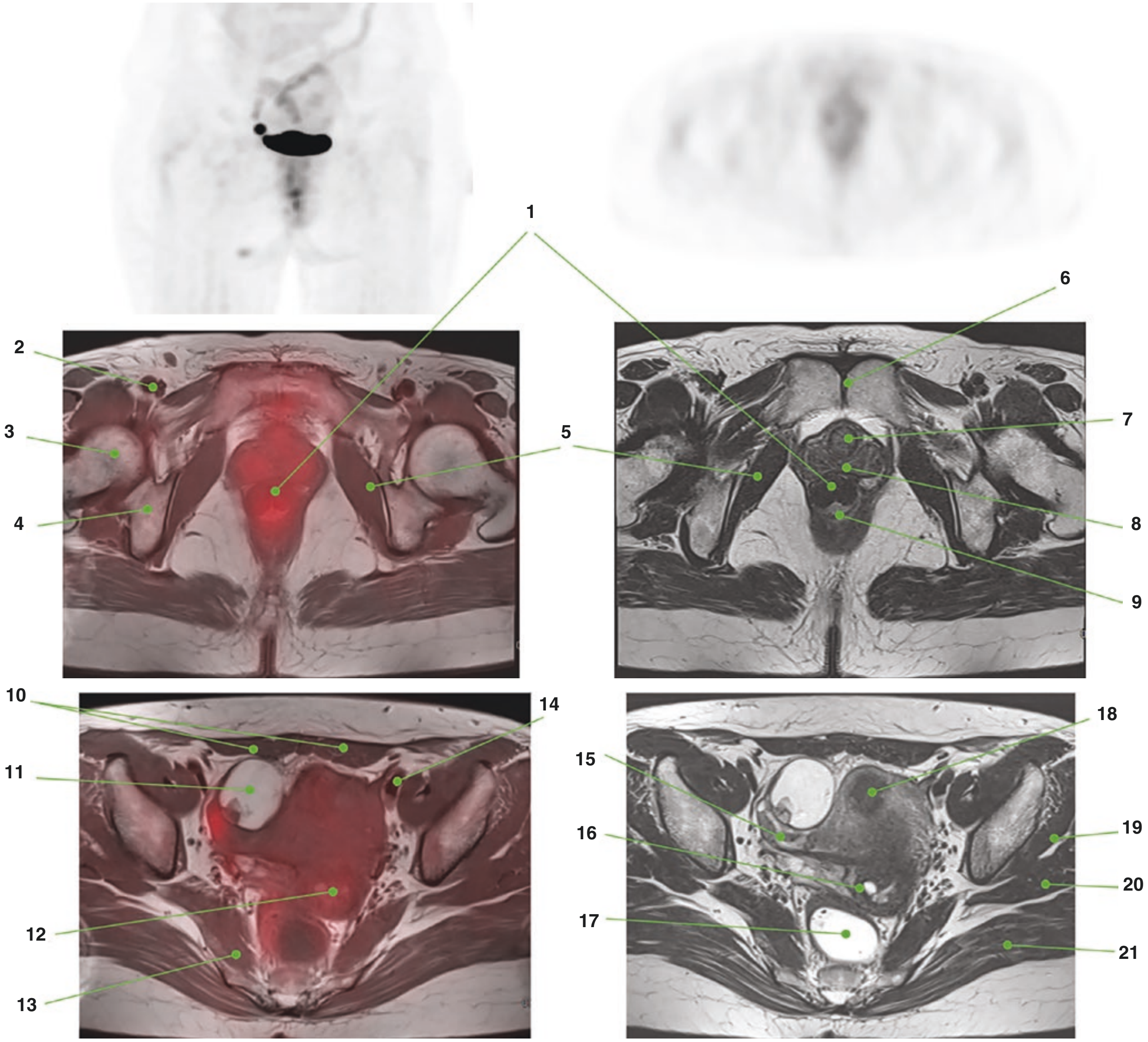

Figs. 37 and 38 1. Anterior rectal wall leiomyoma
2. Right femoral vessels
3. Right femoral head
4. Right acetabulum
5. Internal obturator muscles
6. Pubic symphysis
7. Urethra
8. Vagina
9. Rectal lumen
10. Rectus abdominis muscles
11. Complex right adnexal cyst with posterior papillary projection
12. Cervix
13. Right ischio-coccygeus muscle
14. Left external iliac vessels
15. Right fallopian tube
16. Nabothian cyst in the cervix
17. Proximal rectum
18. Uterine myoma
19. Gluteus minimus muscle
20. Gluteus medius muscle
21. Gluteus maximus muscle

3.12 Case 12

A 59-year-old female patient with an abnormal Pap smear test. Cervical punch biopsy revealed a squamous cell carcinoma, so ^{18}F-FDG PET/MR was done for initial staging. Images showed a hypermetabolic mass in the uterine cervix involving the posterior upper vaginal wall, but not the parametrium. No abnormal hypermetabolic lesions suggesting metastasis were found (Figs. 39 and 40) [37, 38].

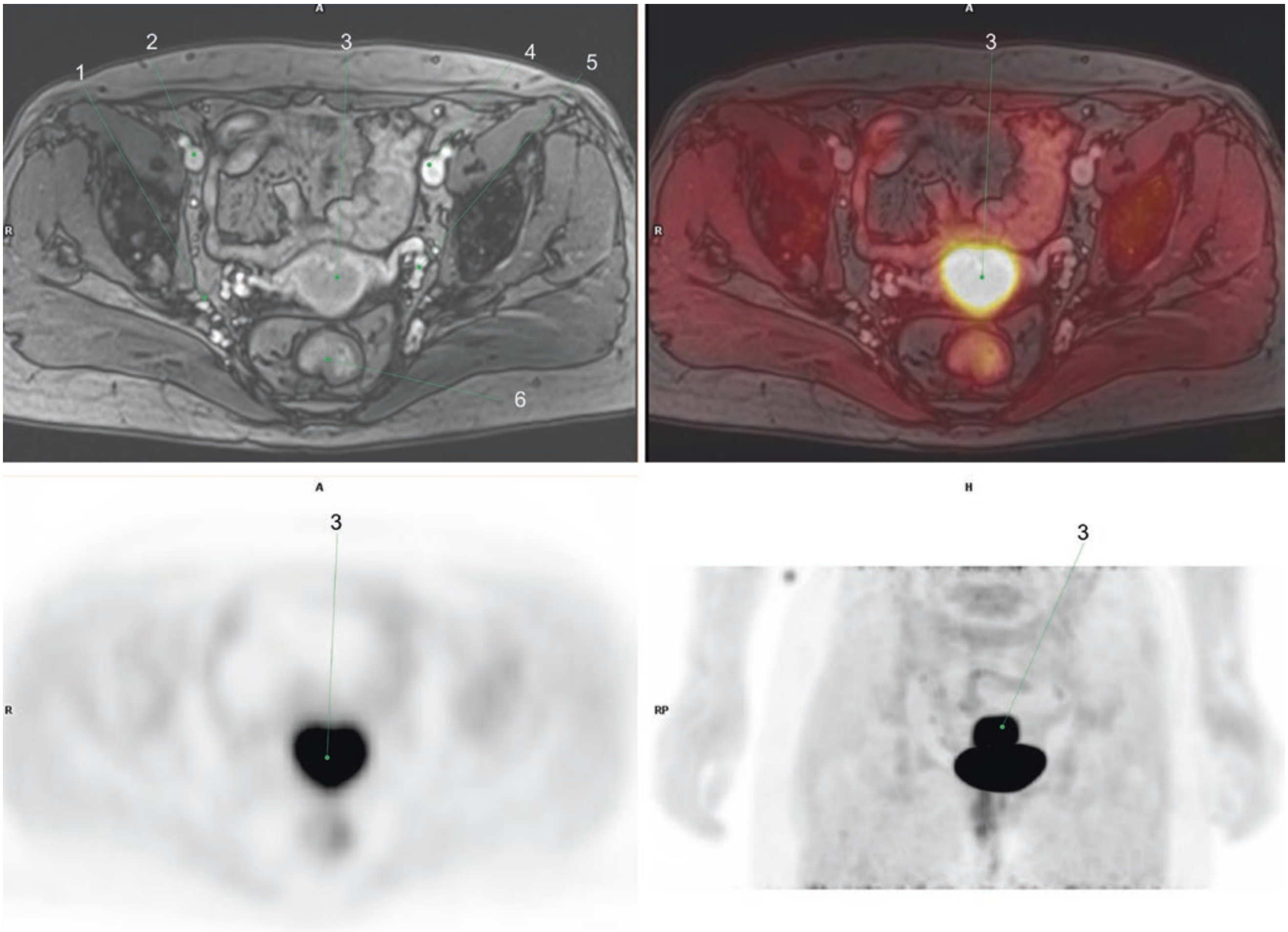

Fig. 39 1. Right internal iliac vessels
2. Right external iliac vessels
3. Metabolically active cervical cancer
4. Left external iliac vessels
5. Left internal iliac vessels
6. Rectum

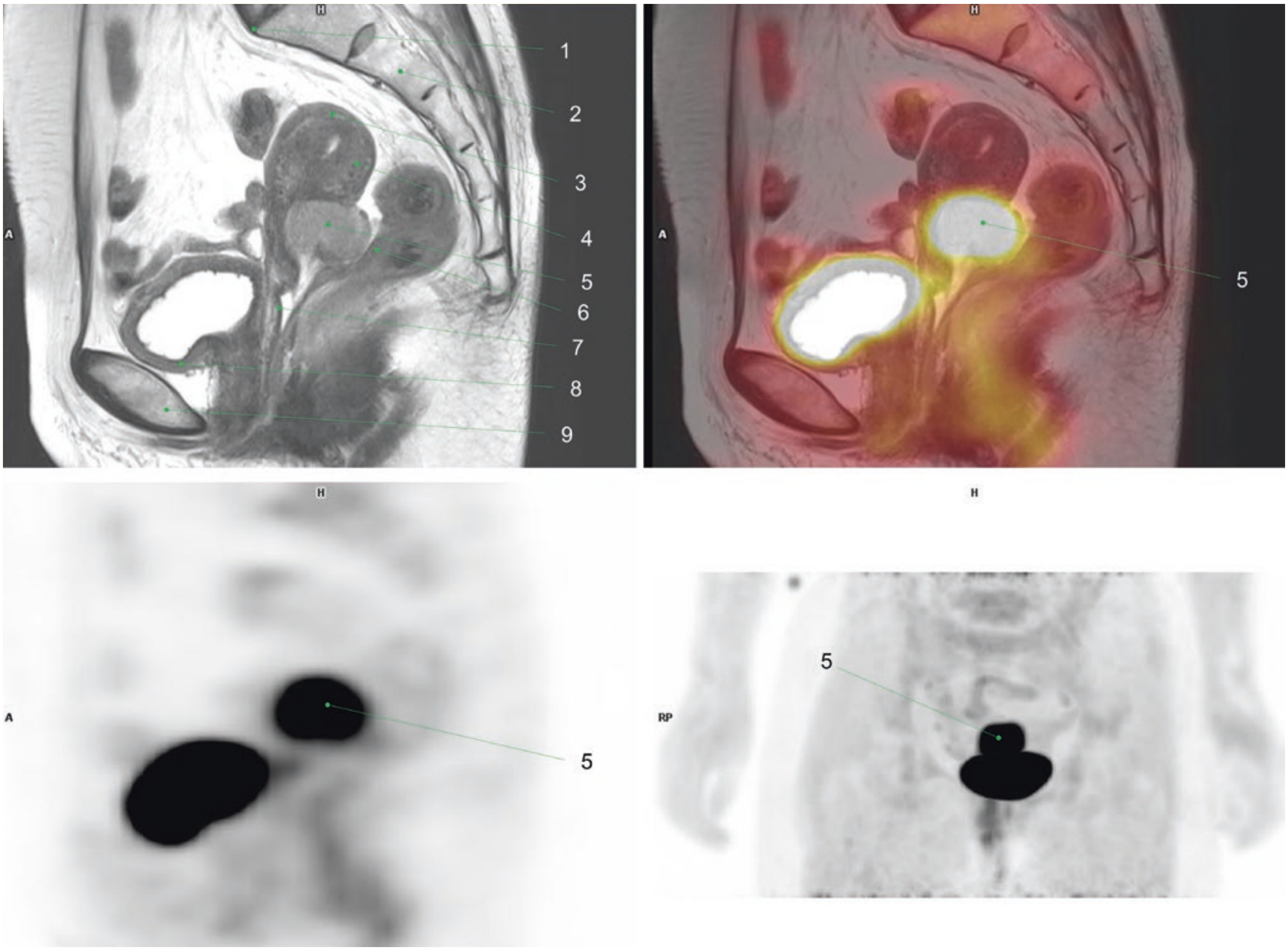

Fig. 40 1. Sacral promontory
2. Sacrum, S2
3. Uterine fundus
4. Uterine body (myometrium)
5. Metabolically active cervical cancer involving posterior vaginal fornix
6. Rectum
7. Vagina
8. Urinary bladder
9. Pubic bone

3.13 Case 13

A 41-year-old female patient with vaginal bleeding. Cervical biopsy revealed a squamous cell carcinoma, so ^{18}F-FDG PET/MR was done for staging. Images showed a hypermetabolic uterine cervical mass involving the parametrium and the lower third of the vagina. Hypermetabolic and enlarged metastatic LNs were also found in both the external iliac and left internal and perirectal areas (Figs. 41, 42, 43, and 44) [37, 38].

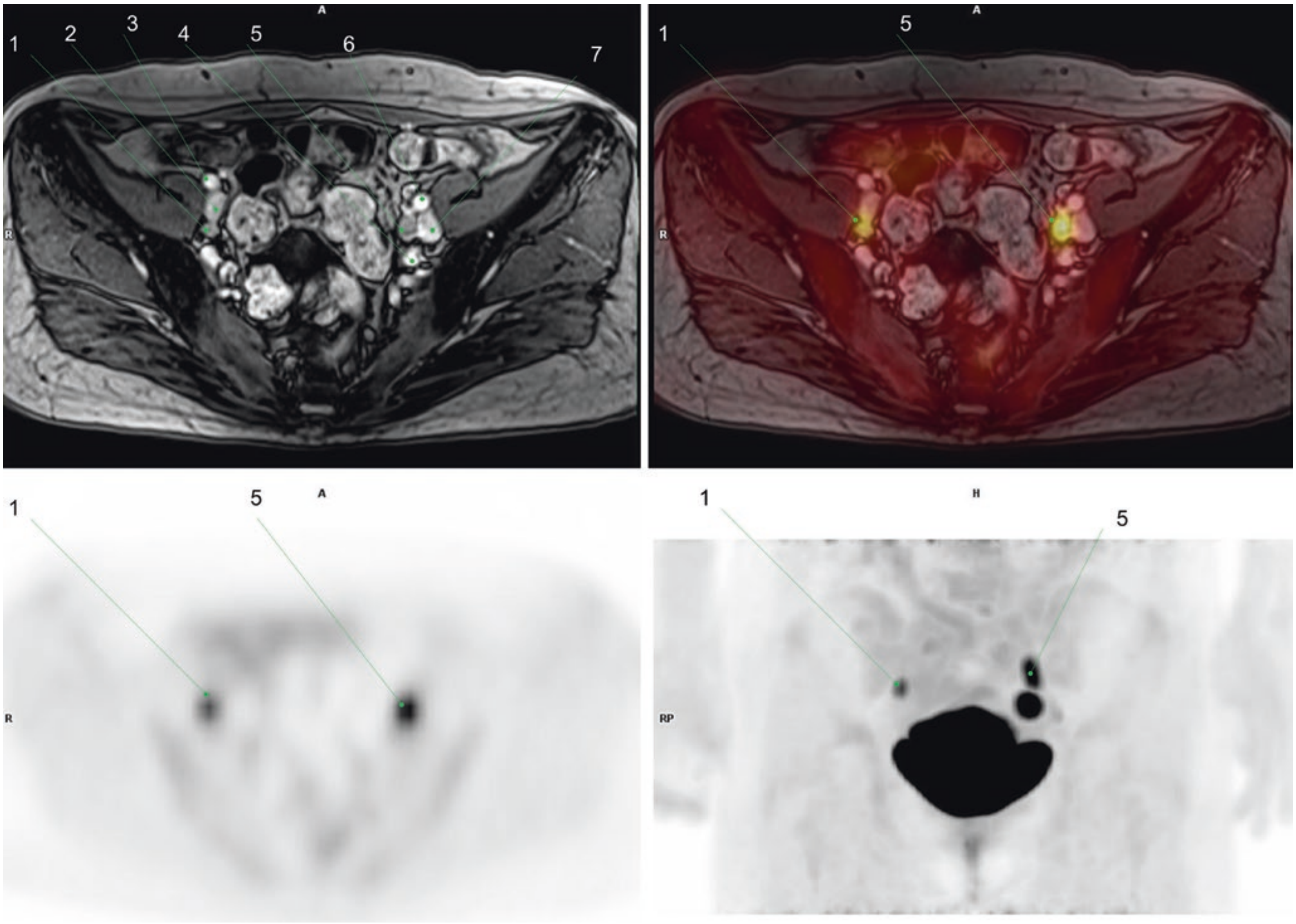

Fig. 41 1. Right external iliac LN metastasis
2. Right external iliac vein
3. Right external iliac artery
4. Left internal iliac artery
5. Left external iliac LN metastasis
6. Left external iliac artery
7. Left external iliac vein

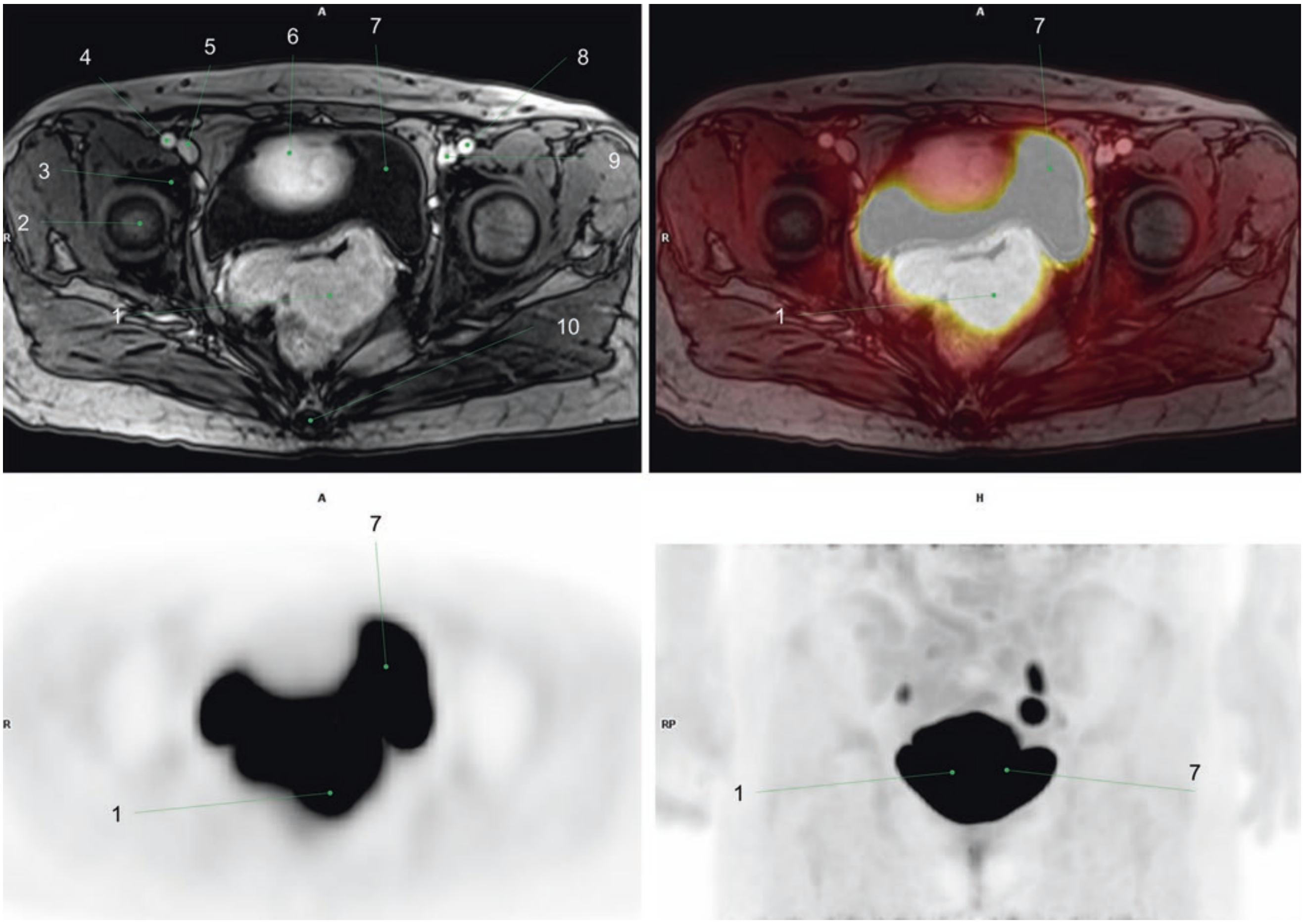

Fig. 42 1. Metabolically active cervical cancer
2. Right femoral head
3. Right acetabulum
4. Right femoral artery
5. Right femoral vein
6. Uterus, fundus
7. Urinary bladder
8. Left femoral artery
9. Left femoral vein
10. Coccyx

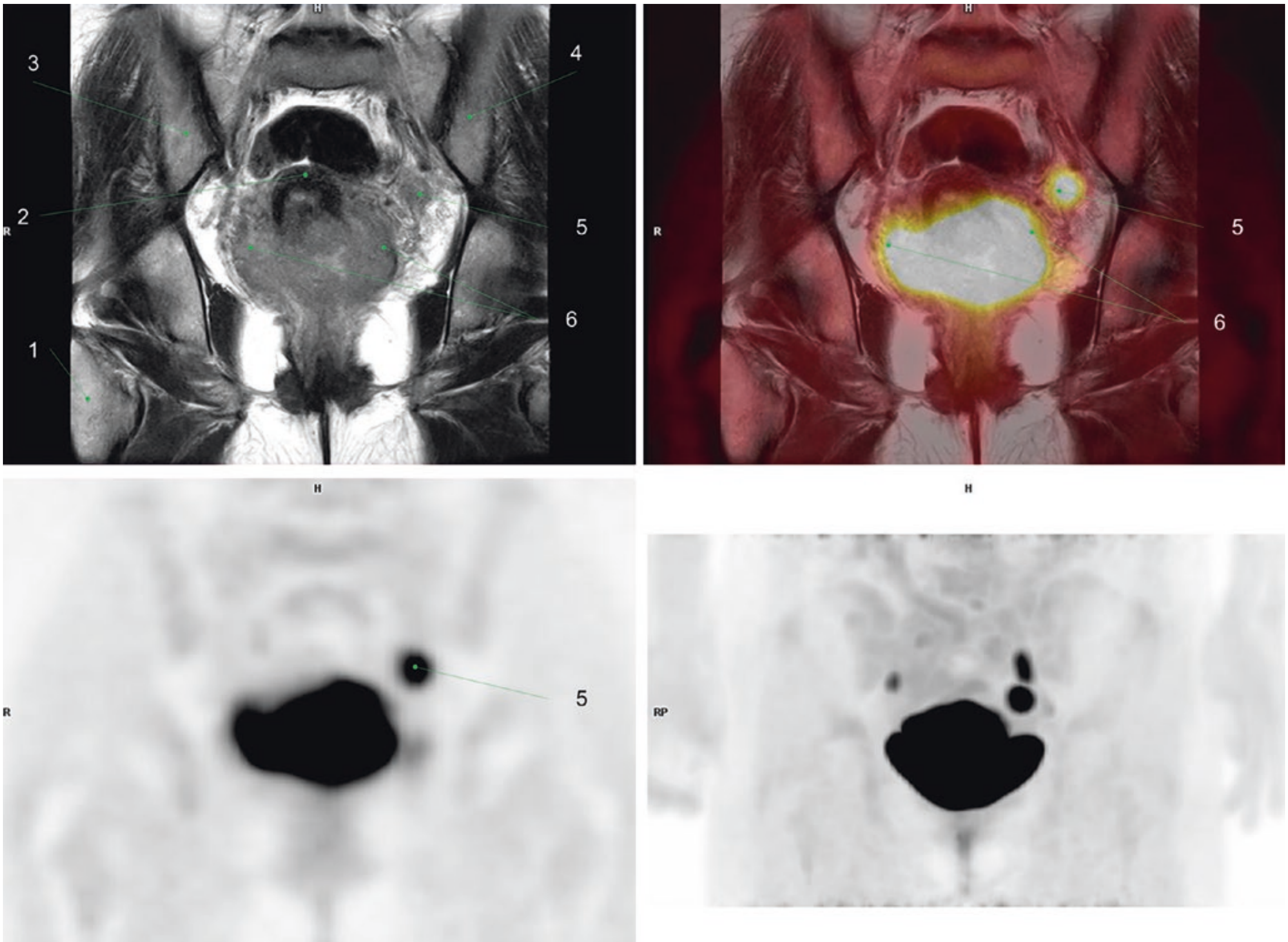

Fig. 43 1. Right proximal femur
2. Uterus
3. Right Ilium
4. Left ilium
5. Left pelvic LN metastasis
6. Bilateral parametrial invasion of cervical cancer

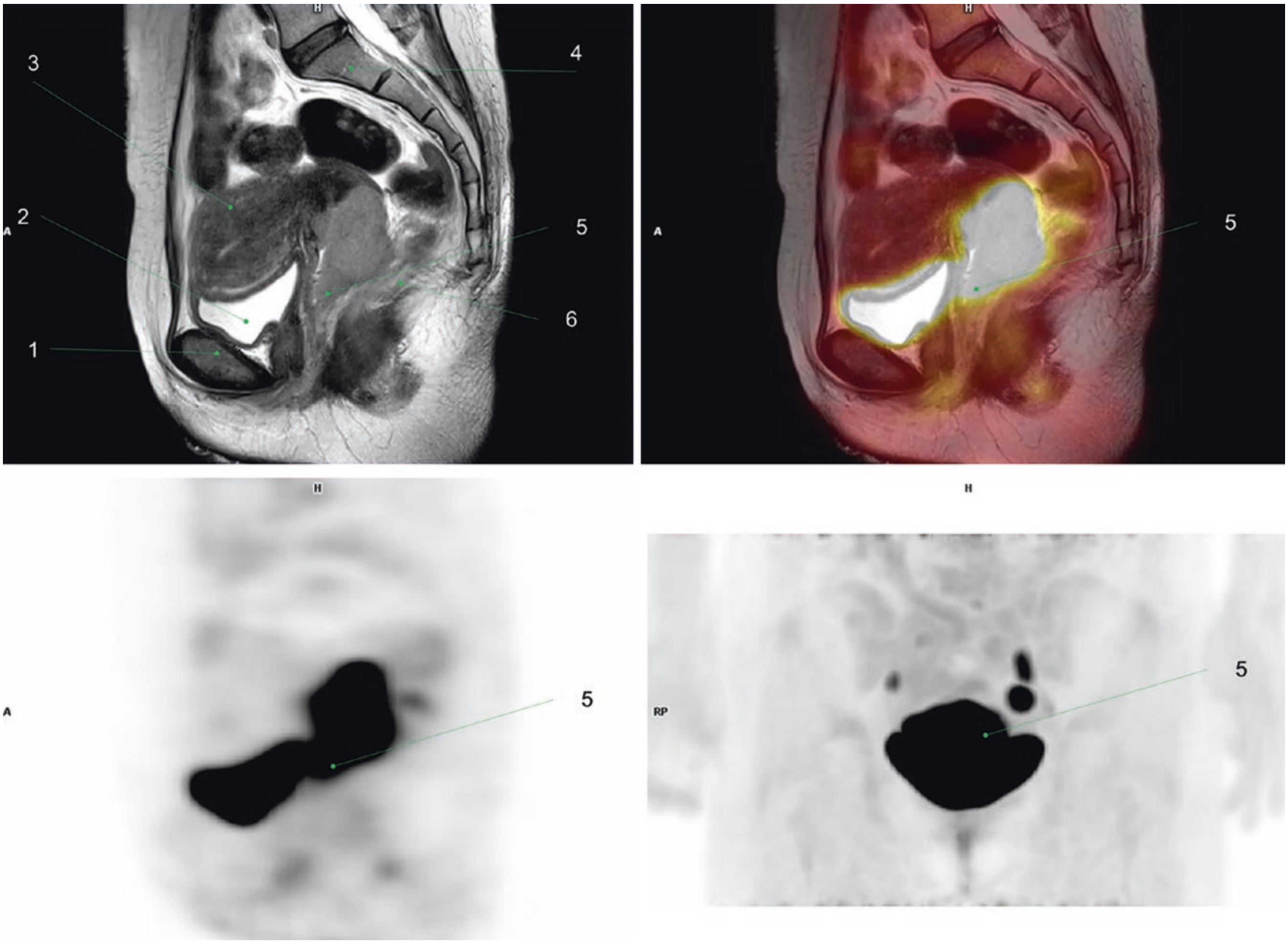

Fig. 44 1. Pubic bone
2. Urinary bladder
3. Uterus fundus
4. Sacrum S1
5. Metabolically active cervical cancer, lower vaginal extension
6. Rectum

4 Musculoskeletal System

4.1 Case 1

A 42-year-old female patient with a palpable mass in the right lower leg. ^{18}F-FDG PET/MR was performed for further evaluation, finding a multilobulated soft tissue mass with moderately increased activity at the posterior compartment of the right lower leg. Enlarged LNs with mildly increased metabolism were also observed in the right external iliac, inguinal, and popliteal regions. Posterior biopsy confirmed synovial sarcoma in the primary mass, and reactive inflammatory LNs in other locations, which is an expected finding since sarcomas very rarely metastasize to LNs (Figs. 45, 46, 47, 48, and 49) [39, 40].

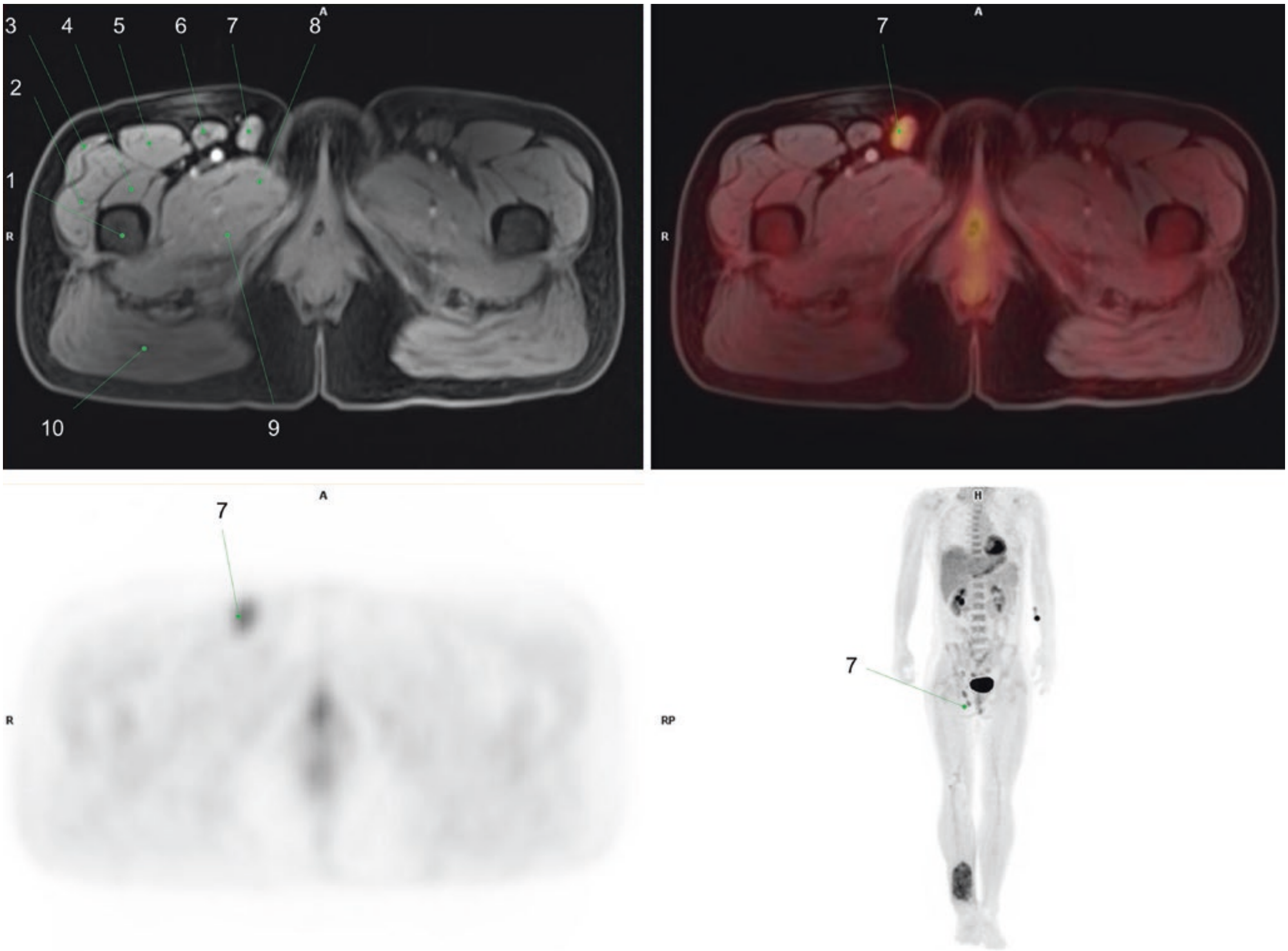

Fig. 45 1. Right femoral shaft
2. Right vastus lateralis muscle
3. Right tensor fasciae latae muscle
4. Right vastus intermedius muscle
5. Right rectus femoris muscle
6. Right sartorius muscle
7. Right inguinal LN with mild increased activity, reactive
8. Right adductor brevis muscle
9. Right adductor magnus muscle
10. Right gluteus maximus muscle

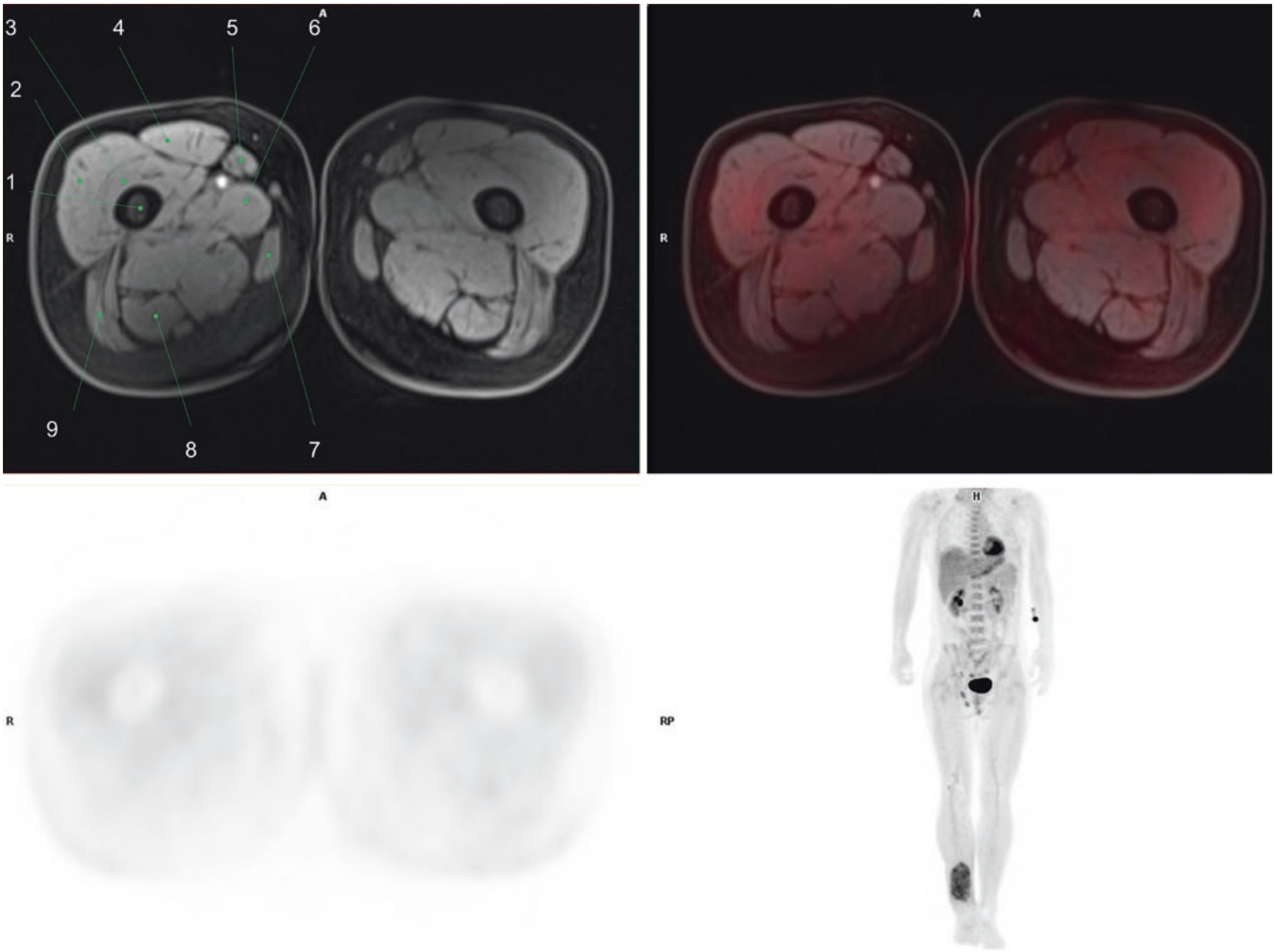

Fig. 46 1. Right femur
2. Right vastus lateralis muscle
3. Right vastus medialis and intermedius muscle
4. Right rectus femoris muscle
5. Right sartorius muscle
6. Right adductor longus muscle
7. Right gracilis muscle
8. Right semitendinosus muscle
9. Right gluteus maximus muscle

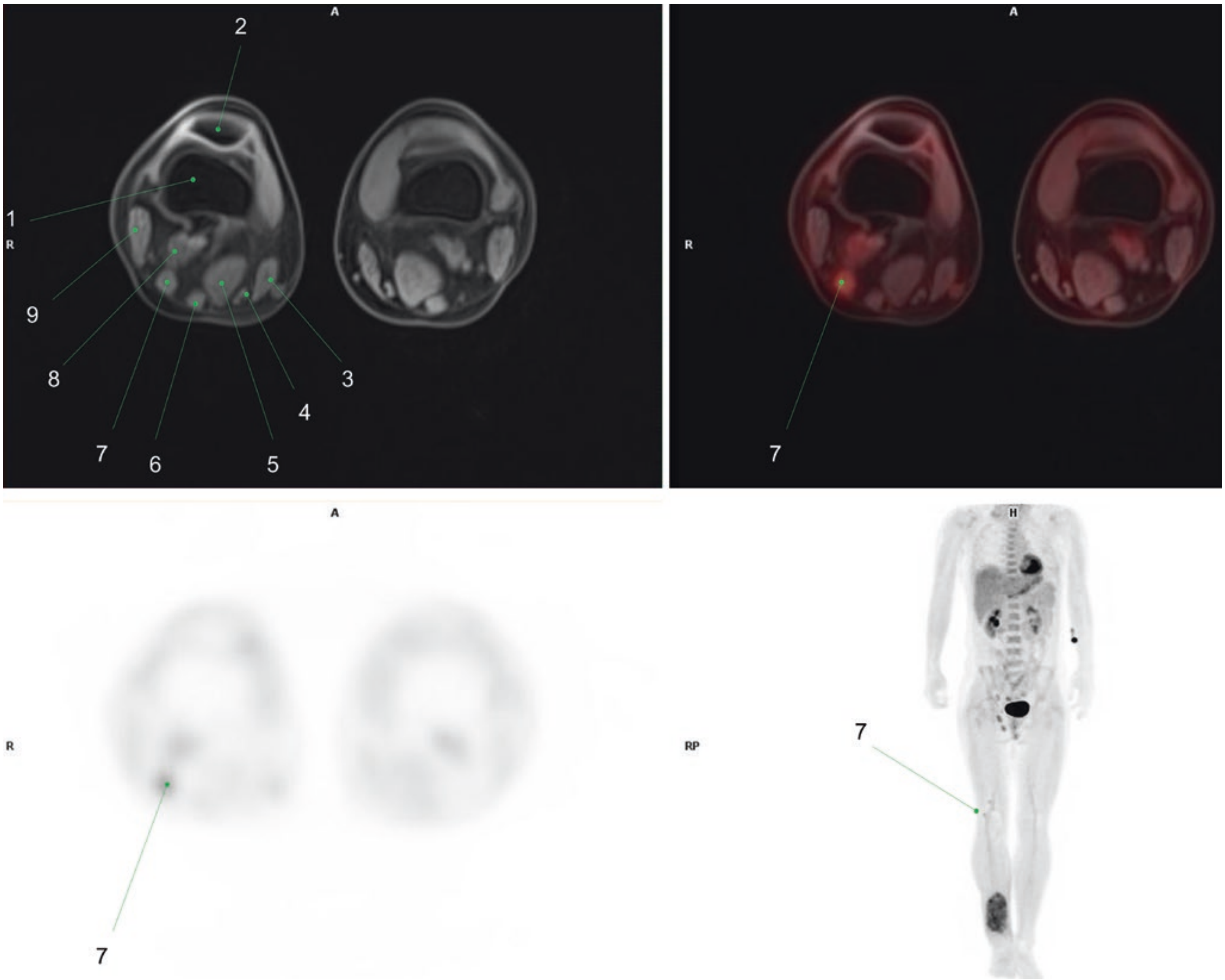

Fig. 47 1. Right femur
2. Right patella
3. Right sartorius muscle
4. Right gracilis muscle
5. Right semimembranosus
6. Right semitendinosus muscle
7. Right popliteal LN with mild increased activity, reactive
8. Right gastrocnemius muscle
9. Right biceps femoris muscle

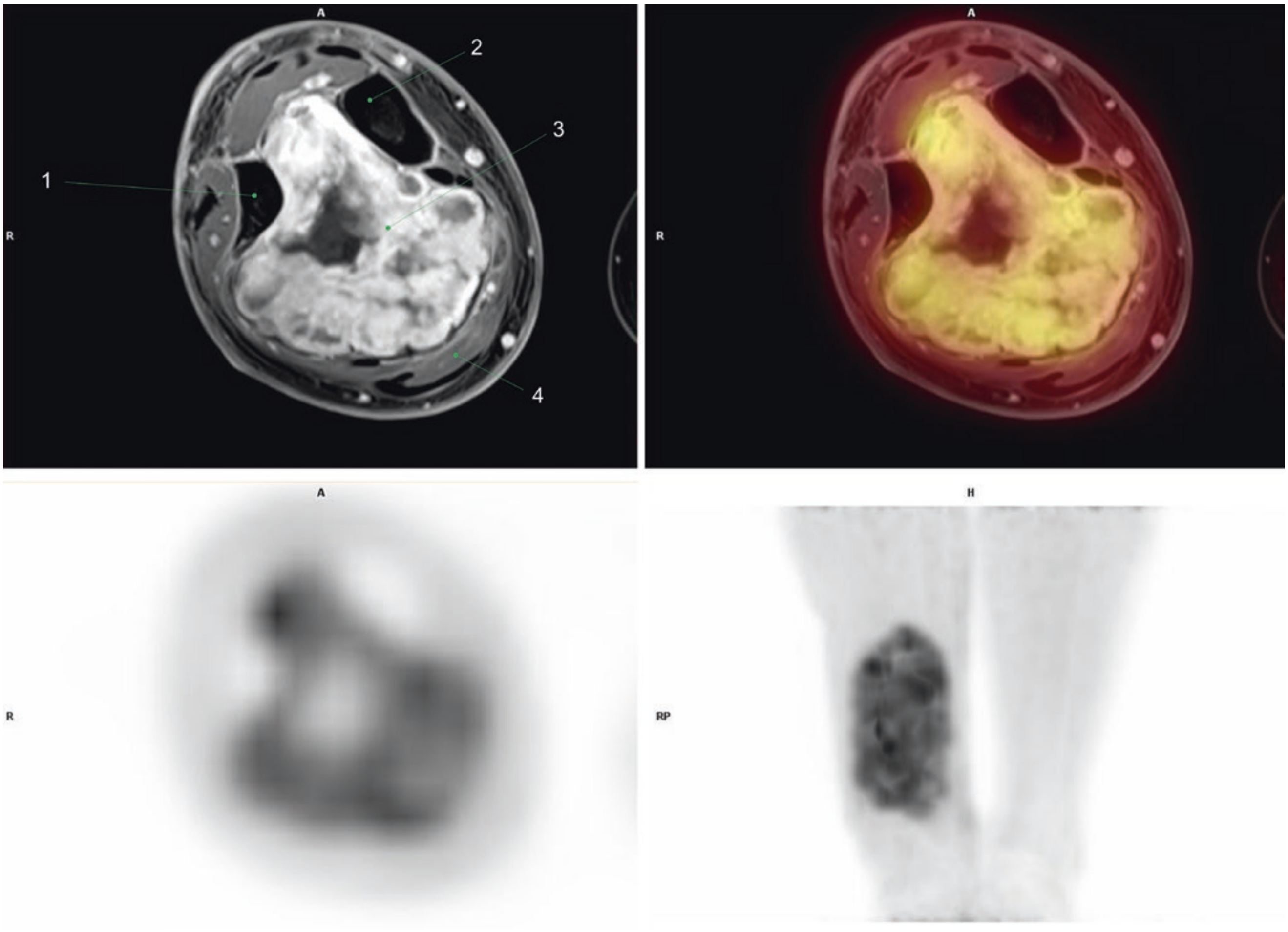

Fig. 48 1. Fibula shaft
2. Tibial shaft
3. Metabolically active synovial sarcoma
4. Gastrocnemius muscle

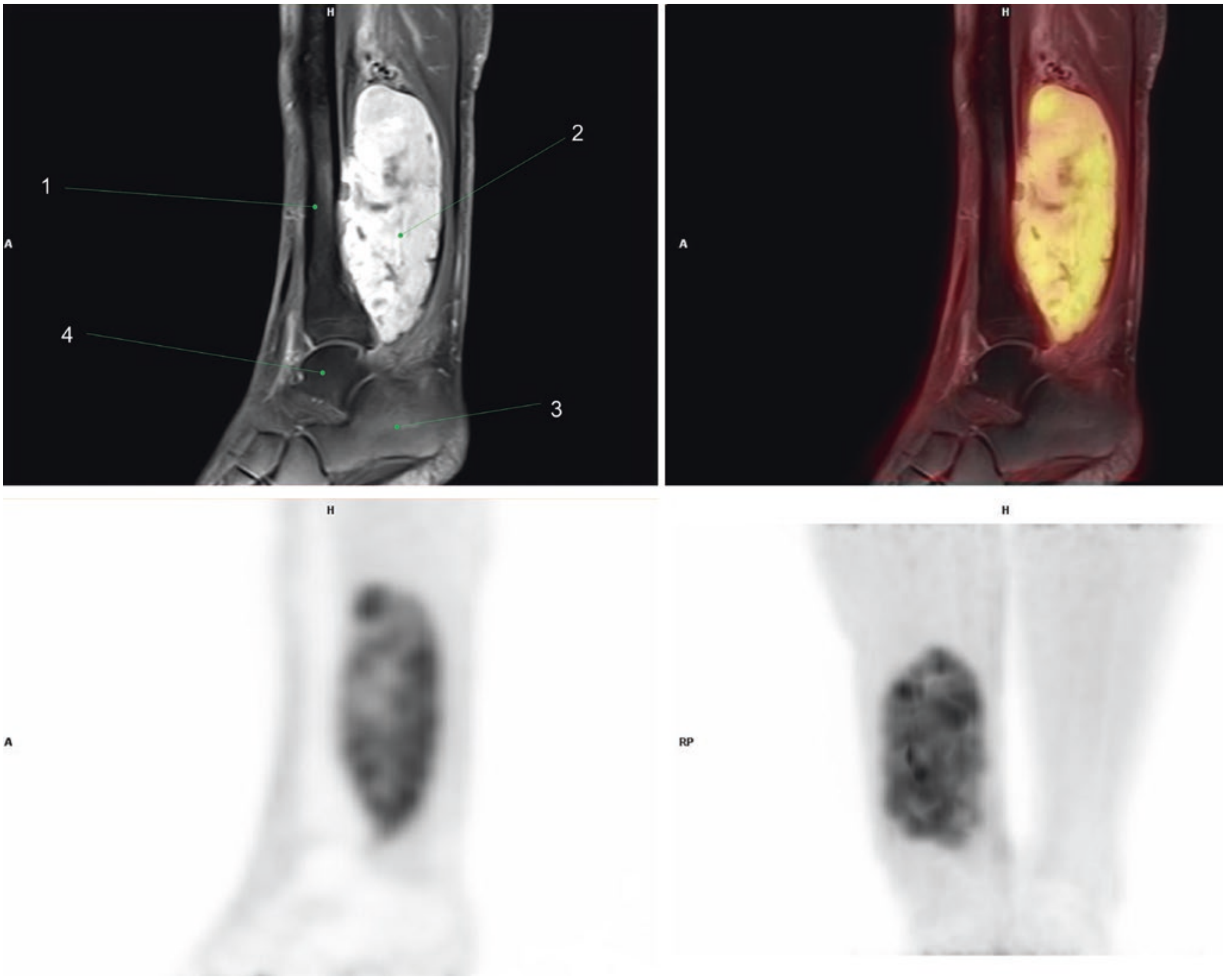

Fig. 49 1. Tibial shaft
2. Metabolically active synovial sarcoma
3. Calcaneus
4. Talus

4.2 Case 2

A 39-year-old male patient with a palpable mass in the right thigh. ^{18}F-FDG PET/MR was done for initial evaluation and staging. Images showed mild increased activity at a well-marginated enhancing mass in the right inner thigh. Myxoid liposarcoma was revealed by needle biopsy (Fig. 50) [39].

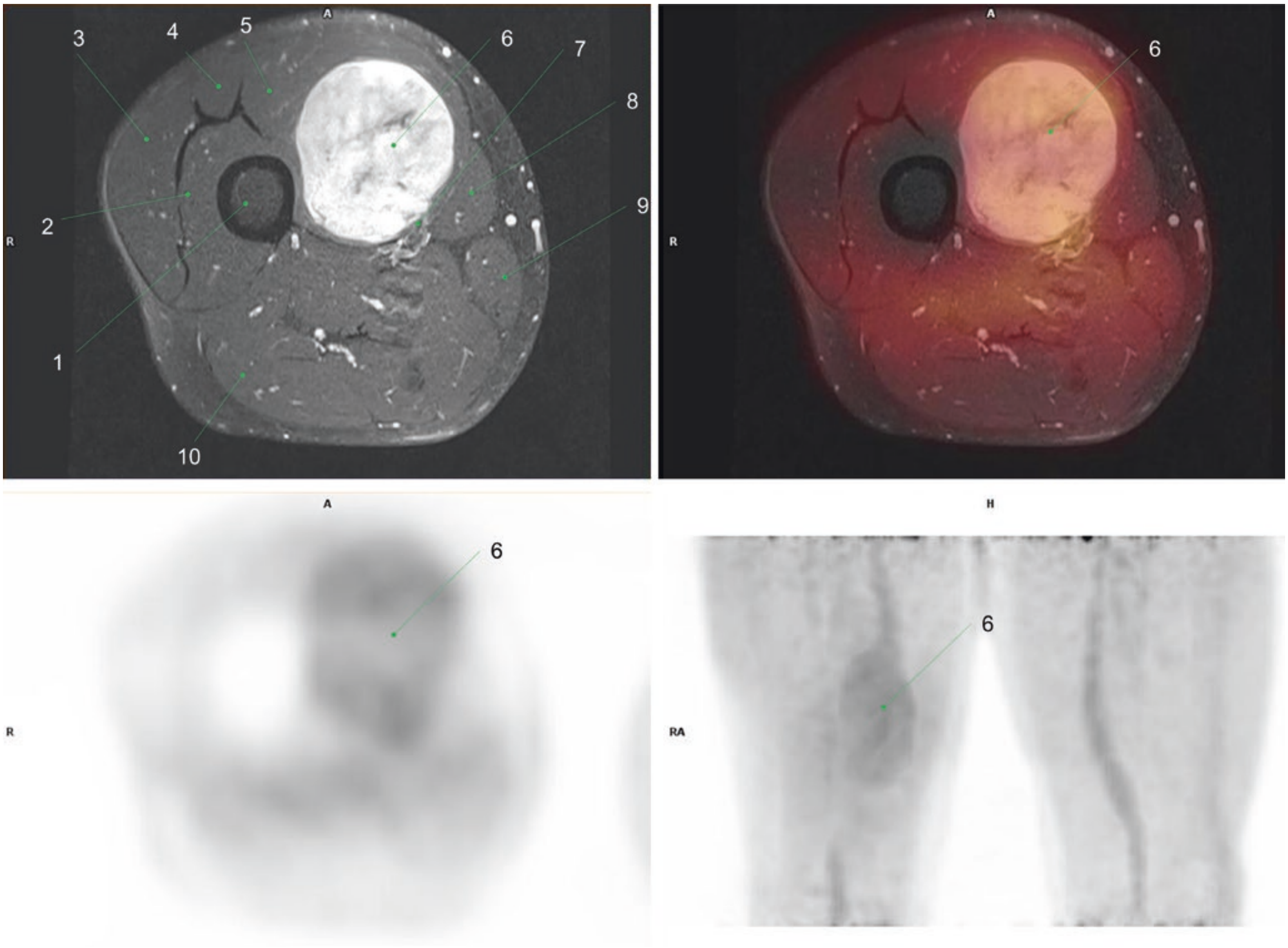

Fig. 50 1. Femoral shaft
2. Vastus intermedius muscle
3. Vastus lateralis muscle
4. Rectus femoris muscle
5. Vastus medialis muscle
6. Mild hypermetabolic liposarcoma
7. Femoral vessel
8. Sartorius muscle
9. Gracilis muscle
10. Biceps femoris muscle

4.3 Case 3

A 16-year-old female patient with chronic pelvic pain. X-ray and CT scan revealed an aggressive bone lesion in the left pelvic bone, and needle biopsy confirmed the diagnosis of osteosarcoma, so ^{18}F-FDG PET/MR was performed for staging. Images showed increased activity at a destructive bony lesion in the left pelvic bone involving the ilium, sacrum, and acetabulum, and encasing the left internal iliac vessels and sacral plexus. Inside the mass, an area with signal void on T2WI and marked contrast enhancement was identified, suggestive of intratumoral aneurysm. Multiple mild hypermetabolic metastatic lung nodules were also found (Figs. 51 and 52) [41, 42].

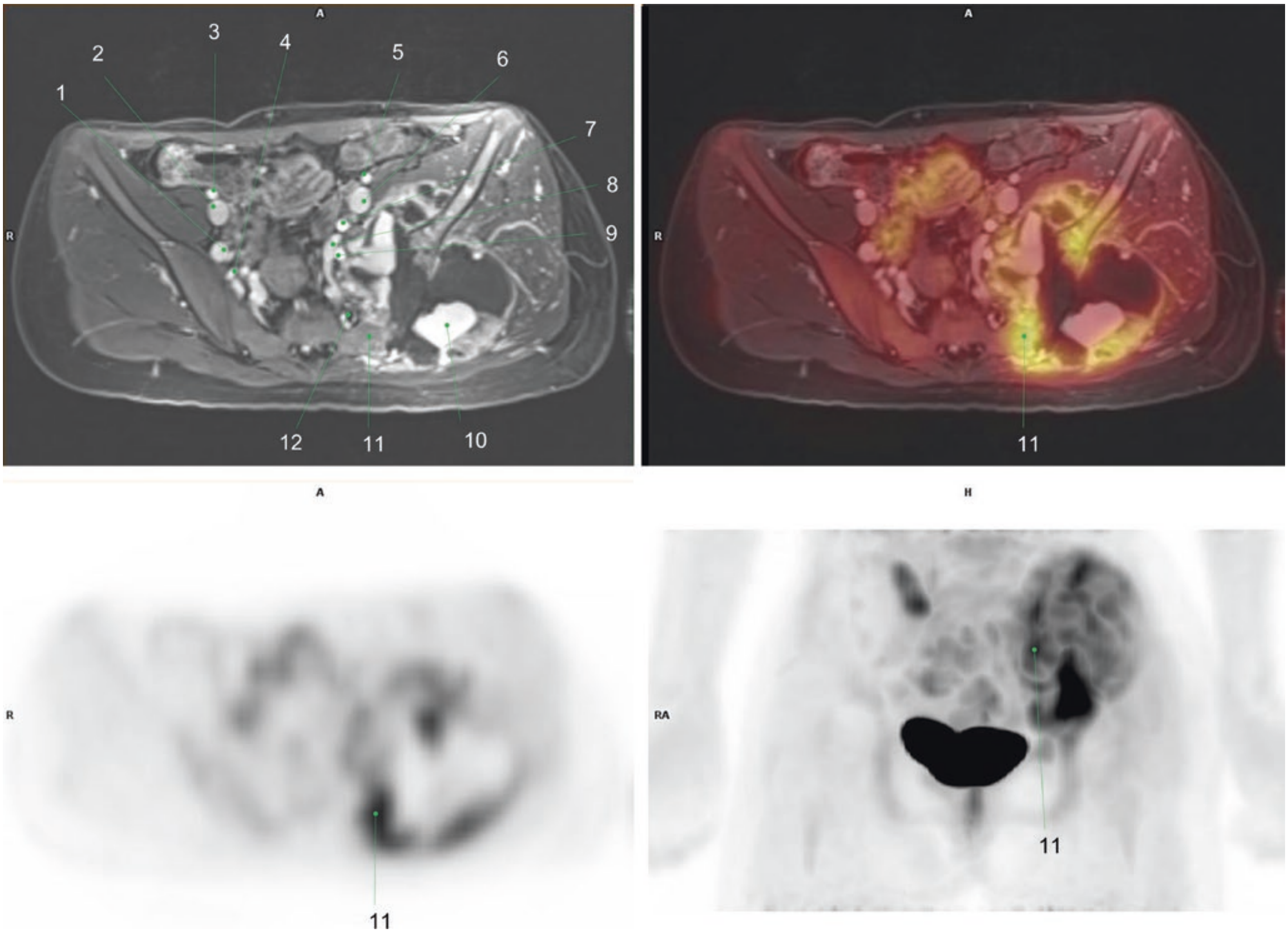

Fig. 51 1. Right internal iliac vein
2. Right external iliac vein
3. Right external iliac artery
4. Right internal iliac artery
5. Left external iliac artery
6. Left external iliac vein
7. Left internal iliac artery
8. Left internal iliac vein
9. Obturator artery
10. Intratumoral aneurysmal change of tumor vessel
11. Metabolically active osteosarcoma involving the left sacral ala
12. Sacral plexus

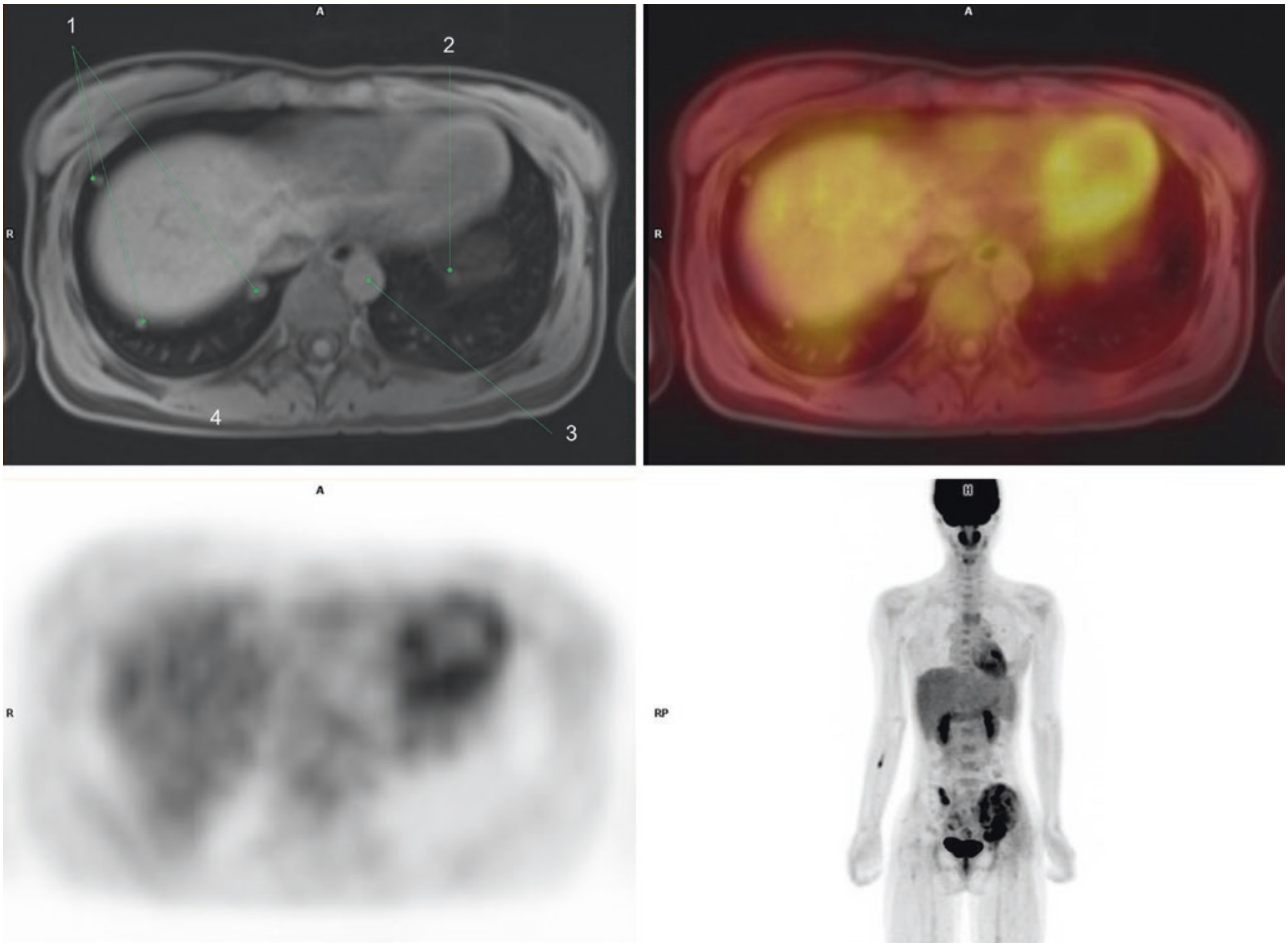

Fig. 52 1. Mild metabolically active lung metastases, right left lobe (RLL)
2. Mild metabolically active lung metastasis, Left lower lobe (LLL)
3. Descending aorta

Acknowledgments *The authors gratefully acknowledge Dr. Dong Soo Lee and Dr. Keon Wook Kang for their contributions to this chapter as it appeared in the previous edition.*

References

1. Levin CS, Maramraju SH, Khalighi MM, Deller TW, Delso G, Jansen F. Design features and mutual compatibility studies of the time-of-flight PET capable GE SIGNA PET/MR system. IEEE Trans Med Imaging. 2016;35:1907–14.
2. Chen Y, An H. Attenuation correction of PET/MR imaging. Magn Reson Imaging Clin N Am. 2017;25:245–55.
3. Fayad H, Lamare F, Merlin T, Visvikis D. Motion correction using anatomical information in PET/CT and PET/MR hybrid imaging. Q J Nucl Med Mol Imaging. 2016;60:12–24.
4. Bronski SM, Goenka AH, Kemp BJ, Johnson GB. clinical PET/MRI: 2018 update. AJR. 2018;211:295–313.
5. Kaufmann S, Kruck S, Gatidis S, et al. Simultaneous whole-body PET/MRI with integrated multiparametric MRI for primary staging of high-risk prostate cancer. World J Urol. 2020;38:2513–21.
6. Leithner D, Horvat JV, Bernard-Davila B, et al. A multiparametric [^{18}F]FDG PET/MRI diagnostic model including imaging biomarkers of the tumor and contralateral healthy breast tissue aids breast cancer diagnosis. Eur J Nucl Med Mol Imaging. 2019;46:1878–88.
7. Öztürk H. PET/MRI: the future of cancer restaging. Cancer Treatment Res Commun. 2020;25:100250.
8. Kirchner J, Sawicki LM, Deuschl C, et al. ^{18}F-FDG PET/MR imaging in patients with suspected liver lesions: value of liver-specific contrast agent gadobenate dimeglumine. PLoS One. 2017;12:e0180349.
9. Rutegård MK, Båtsman M, Axelsson J, et al. PET/MRI and PET/CT hybrid imaging of rectal cancer - description and initial observations from the RECTOPET (REctal Cancer trial on PET/MRI/CT) study. Cancer Imaging. 2019;19(1):52.
10. Huellner MW. PET/MR in head and neck cancer - an update. Semin Nucl Med. 2021;51(1):26–38.
11. Virarkar M, Devine C, Bassett R Jr, Javadi S, De Castro FS, Bhosale P. Update on diagnostic performance of PET/MRI in gynecological malignancies: a systematic review and meta-analysis. J Belgian Soc Radiol. 2020;104(1):4.
12. Cassarino G, Evangelista L, Giraudo C. et al. ^{18}F-FDG PET/MRI in adult sarcomas. Clin Transl Imaging. 2020;8:405–12.
13. Sgard B, Brillet PY, Bouvry D, Djelbani S, Nunes H, Meune C, Valeyre D, Soussan M. Evaluation of FDG PET combined with cardiac MRI for the diagnosis and therapeutic monitoring of cardiac sarcoidosis. Clin Radiol. 2019;74(1):81.

14. Nguyen NC, Moon C-H, Muthukrishnan A, Furlan A. 68Ga-DOTATATE PET/MRI for neuroendocrine tumors. Clin Nucl Med. 2020;45(9):e406–10.
15. Evangelista L, Zattoni F, Cassarino G, et al. PET/MRI in prostate cancer: a systematic review and meta-analysis. Eur J Nucl Med Mol Imaging. 2021;48:859–73.
16. Overcast WB, Davis KM, Ho CY, et al. Advanced imaging techniques for neuro-oncologic tumor diagnosis, with an emphasis on PET-MRI imaging of malignant brain tumors. Curr Oncol Rep. 2021;23:34.
17. Laudicella R, Iagaru A, Minutoli F, et al. PET/MR in neuro-oncology: is it ready for prime-time? Clin Transl Imaging. 2020;8:233–5.
18. Ortner M, Drost R, Heddderich D, et al. Amyloid PET, FDG-PET or MRI? - the power of different imaging biomarkers to detect progression of early Alzheimer's disease. BMC Neurol. 2019;19:264.
19. Kerstens VS, Varrone A. Dopamine transporter imaging in neurodegenerative movement disorders: PET vs. SPECT Clin Transl Imaging. 2020;8:349–56.
20. Mohile NA, Deangelis LM, Abrey LE. The utility of body FDG PET in staging primary central nervous system lymphoma. Neuro Oncol. 2008;10:223–8.
21. Thomas R, Braschi-Amirfarzan M, Laferriere SL, Jagannathan JP. Imaging of Waldenström Macroglobulinemia: a comprehensive review for the radiologist in the era of personalized medicine. AJR. 2019;213:248–56.
22. Natarajan A, Chandra P, Purandare N, Agrawal A, Shah S, Puranik A, et al. Role of fluorodeoxyglucose positron emission tomography/computed tomography in various orbital malignancies. IJNM. 2018;33(2):118–24.
23. Dadgar H, Norouzbeigi N, Ahmadzadehfar H, Assadi M. 68Ga-DOTATATE and 18F-FDG PET/CT for the management of esthesioneuroblastoma of the sphenoclival region. Clin Nucl Med. 2020;45(8):e363–4.
24. Platzek I, Beuthien-Baumann B, Schneider M, Gudziol V, Langner J, Schramm G, et al. PET/MRI in head and neck cancer: initial experience. Eur J Nucl Med Mol Imaging. 2013;40:6–11.
25. Larson CR, Wiggins RH. FDG-PET imaging of salivary gland tumors. Seminars in Ultrasound, CT and MRI. 2018;40(5):391–9.
26. Higashiyama A, Komori T, Inada Y, Nishizawa M, Nakajima H, Narumi Y. Diffuse ^{18}F-FDG uptake throughout the spinal cord in the acute phase of Neuromyelitis Optica Spectrum disorder. Eur J Nucl Med Mol Imaging. 2017;44(9):1609–10.
27. Heusch P, Buchbender C, Kohler J, Nensa F, Gauler T, Gomez B, et al. Thoracic staging in lung cancer: prospective comparison of 18F-FDG PET/MR imaging and 18F-FDG PET/CT. J Nucl Med. 2014;55:373–8.
28. Kohan AA, Kolthammer JA, Vercher-Conejero JL, Rubbert C, Partovi S, Jones R, et al. N staging of lung cancer patients with PET/MRI using a three-segment model attenuation correction algorithm: initial experience. Eur Radiol. 2013;23:3161–9.
29. Lee J, Cho YS, Kim J, Shim YM, Lee K-H, Choi JY. Prognostic significance of metabolic parameters by 18F-FDG PET/CT in thymic epithelial tumors. Cancer. 2021;13:712.
30. Wu CX, Zhu ZH. Diagnosis and evaluation of gastric cancer by positron emission tomography. World J Gastroenterol. 2014;20:4574–85.
31. Francis IR, Cohan RH, Varma DGK, Sondak VK. Retroperitoneal sarcomas. Cancer Imaging. 2005;5:89–94.
32. Moradi F, Ladaru A. The role of positron emission tomography in pancreatic cancer and gallbladder cancer. Semin Nucl Med. 2020;50(5):434–46.
33. Lu RC, She B, Gao WT, Ji YH, Xu DD, Wang QS, et al. Positron-emission tomography for hepatocellular carcinoma: current status and future prospects. World J Gastroenterol. 2019;25(32):4682–95.
34. Ota Y, Aso K, Watanabe K, Einama T, Imai K, Karasaki H, et al. Hepatic schwannoma: imaging findings on CT, MRI and contrast-enhanced ultrasonography. World J Gastroenterol. 2012;18:4967–72.
35. Wei K, Pan B, Yang H, Lu C, Ge L, Cao N. F-18 FDG PET, CT, and MRI for detecting the malignant potential in patients with gastrointestinal stromal tumors. Medicine. 2018;97(16):e0389.
36. Lee DH, Lee JM. Whole-body PET/MRI for colorectal cancer staging: is it the way forward? J Magn Reson Imaging. 2017;45(1):21–35.
37. Sala E, Wakely S, Senior E, Lomas D. MRI of malignant neoplasms of the uterine corpus and cervix. AJR Am J Roentgenol. 2007;188:1577–87.
38. Son H, Kositwattanarerk A, Hayes MP, Chuang L, Rahaman J, Heiba S, et al. PET/CT evaluation of cervical cancer: spectrum of disease. Radiographics. 2010;30:1251–68.
39. Schuler MK, Richter S, Beuthien-Baumann B, Platzek I, Kotzerke J, van den Hoff J, et al. PET/MRI imaging in high-risk sarcoma: first findings and solving clinical problems. Case Rep Oncol Med. 2013;2013:793927.
40. Partovi S, Kohan AA, Zipp L, Faulhaber P, Kosmas C, Ros PR, et al. Hybrid PET/MR imaging in two sarcoma patients — clinical benefits and implications for future trials. Int J Clin Exp Med. 2014;7:640–8.
41. Brenner W, Bohuslavizki KH, Eary JF. PET imaging of osteosarcoma. J Nucl Med. 2003;44:930–42.
42. Im HJ, Kim TS, Park SY, Min HS, Kim JH, Kang HG, et al. Prediction of tumour necrosis fractions using metabolic and volumetric 18F-FDG PET/CT indices, after one course and at the completion of neoadjuvant chemotherapy, in children and young adults with osteosarcoma. Eur J Nucl Med Mol Imaging. 2012;39:39–49.